"I told thee what would come of all
thy vapouring"

Samuel Butler
(Hudibras, 1663)

TRANSPORT PROPERTIES OF TYPE 2 SUPERCONDUCTORS.

A thesis submitted

by

Adrian Leonard Hinde

for the

Degree of Doctor of Philosophy

of the University of London

Physics Department

Imperial College of Science and Technology

London

1970

ABSTRACT

Critical current measurements were made on the Pb-Bi system for bismuth concentrations between 1 atomic % and 15 atomic %. Specimens were prepared by evaporation techniques and were of rectangular geometry with thicknesses of the order of 10,000 Å. Measurements were mainly confined to the surface sheath state with applied fields ranging from H_{c_2} to H_{c_3}. Critical currents in fields applied perpendicular and parallel to specimen surfaces yielded the variation of H_{c_2} ($4.2^{\circ}K$) and H_{c_3} ($4.2^{\circ}K$) with alloy composition. In parallel fields close to H_{c_3}, the critical current was proportional to specimen width for changes in width from 0.5 mm to 5.0 mm. Critical currents were also measured with the applied field inclined at an angle φ to the surface. The critical currents in this case could be related to φ through the equation:

$$\frac{1}{I_c} = \frac{1}{I_o} + A \sin\varphi \quad \text{where } I_o \text{ and } A \text{ are constants}$$

Rectification effects were investigated on specimens where surface superconductivity was reduced on one surface by the proximity effect of a 400 Å layer of copper. Diamagnetic critical currents, where the field due to the

transport current opposes the applied field within the specimen bulk, were greater than corresponding paramagnetic currents. The ratio of the diamagnetic current to the paramagnetic current at a given reduced field was insensitive to changes in temperature and alloy composition.

The magnitude and shape of parallel field critical current characteristics were compared with calculations based on solutions of Ginzburg-Landau equations, free energy considerations and for a surface-flux-pinning model. Results favoured explanations based on the surface-pinning model.

Voltage current characteristics were plotted with specimens in parallel fields between H_{c_2} and H_{c_3}. The current in the surface sheath was estimated and interpreted in terms of a flux flow model for power dissipations less than about 0.1 milliwatts/sq. cm.

ACKNOWLEDGEMENTS

I wish to express my thanks to my supervisor Dr J. G. Park for proposing the subject of this thesis and advice during its progress; to Dr D. Griffiths and Mr K. White for assistance in the construction of the proton resonance probe and thickness monitor; to Dr A. P. Murani for help in preparing a computer programme; to Mr F. A. Staff and Mr P. R. Monk of the Analytical Services Laboratory of Imperial College for specimen analysis; to Mr R. Sambles for photographing platinum-carbon replicas of specimen surfaces; to Dr I. Morton for part of the apparatus which he handed on for my use; and to the many other people who have provided friendly and stimulating encouragement.

I also owe thanks to the Science Research Council and the United Kingdom Atomic Energy Authority for providing me with maintenance grants.

Finally I would like to express my gratitude to Joy Dunning for her patience in typing the manuscript.

CONTENTS

INTRODUCTION

Since 1963 when surface superconductivity was understood in terms of solutions of Ginzburg-Landau equations (14) efforts have been made to understand the criterion for the onset of resistance when the surface sheath supports a transport current. Early theories were formulated based on the assumption that the local magnetic field is everywhere parallel to the specimen's surface. Calculations arising from these theories make predictions about the magnitude of the maximum resistance-less surface current and its dependence on sample geometry. Experiments pioneered by Hart and Swartz (44) failed to agree with the predictions, which led them to suggest an alternative approach to the problem. They developed a surface-flux-pinning model where a perpendicular field component can arise from the self field of the transport current. This field component penetrates the sheath in quantized vortices which are pinned by inhomogeneities in the surface structure. The transport current opposes pinning forces and at a critical current level the driving force exceeds the pinning force, the flux spot array moves and a voltage is detected.

Earlier critical current measurements seemed primarily concerned with rectification effects and the sensitivity of the critical currents to different surface treatments. Such investigations were mainly limited to foil specimens with isolated values of the G-L parameter, κ.

Experiments described in this thesis were conducted on evaporated films with similar surface finishes but over a range of compositions. These experiments enabled investigation of the relevance of the various theories concerning the magnitude of the critical surface current and its dependence on the G-L parameter, κ, magnetic field, and specimen geometry.

An important consequence of these investigations was the degree of reproducibility that could be achieved from measurements on thick alloy films prepared by standard evaporation techniques.

CHAPTER I

QUALITATIVE FEATURES OF TYPE-II SUPERCONDUCTORS

1.1 Magnetization Curves of Type-I and Type-II Superconductors

There are two basic types of superconductors, commonly known as type-I and type-II. Each can be characterized by the nature of its magnetization curve. Consider an infinite cylinder of type-I material with its axis parallel to an applied magnetic field. When the field is increased from zero the type-I superconductor exhibits perfect diamagnetism and no flux penetrates the bulk of the cylinder. The Meissner effect of complete flux expulsion exists in fields up to the bulk thermodynamic critical field, H_c, above which the cylinder is completely normal. A type-II superconductor of similar geometry shows the Meissner effect for magnetic fields up to H_{c_1}, which is less than H_c. At H_{c_1} it is energetically favourable for flux to begin to penetrate the cylinder to form a mixed state of normal filaments or vortices embedded within the superconducting phase. An increase in the field beyond H_{c_1} results in an increase in the volume of normal material occupied by flux, and at the upper

critical field, H_{c_2}, the bulk of the cylinder becomes normal. For fields above H_{c_2} a superconducting sheath remains on the surface and is not quenched until a critical field, H_{c_3}, is reached. The magnetization curves for ideal type-I and type-II superconducting infinite cylinders are shown in Fig. 1 and Fig. 2.

Fig.1 The Magnetization Curve of a Type-I Superconductor.

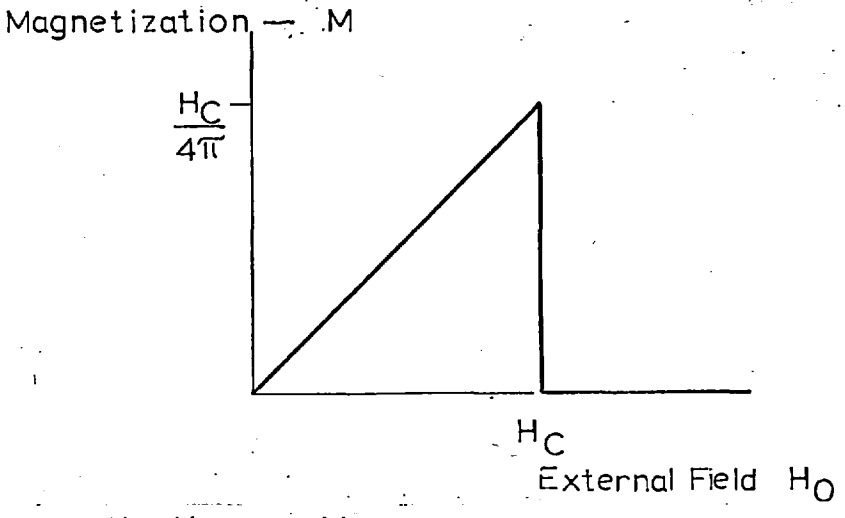

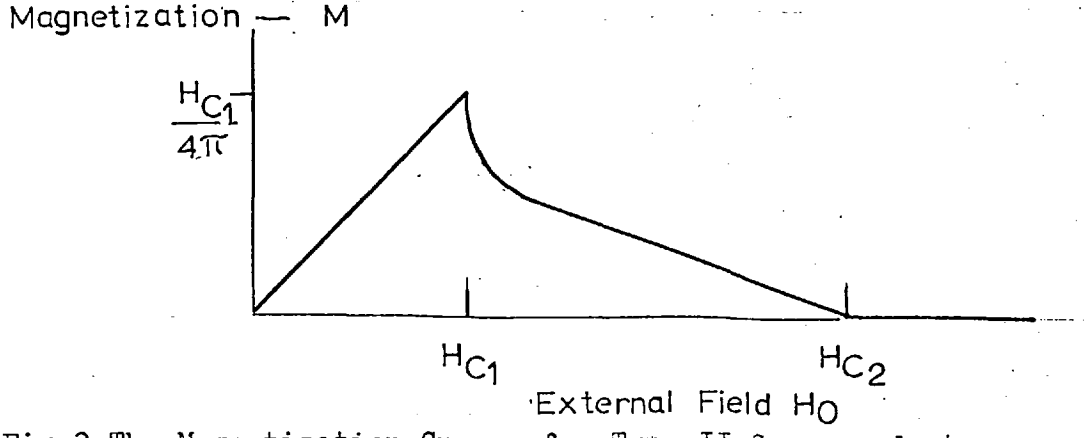

Fig.2 The Magnetization Curve of a Type-II Superconductor.

This magnetic behaviour of type-I and type-II superconductors can be explained in some detail, although for a limited regime of temperatures, from the phenomenological theory of superconductivity derived by Ginzburg and Landau (called the G-L theory henceforth). An important constant in this theory is the G-L parameter, κ, which for a type-I superconductor, near its transition temperature, has a magnitude less than $1/\sqrt{2}$. When κ is greater than $1/\sqrt{2}$ type-II behaviour is observed. In section (1.2) the G-L theory is outlined and in subsequent sections it is shown how solutions of G-L equations can explain the properties of type-II superconductors in the absence of transport currents.

1.2 The Ginzburg Landau Theory

The Gibbs free energy per unit volume of a pure superconductor or superconducting alloy in zero field may be expanded in powers of $|\Psi|^2$ (1) where Ψ is a complex order parameter:

$$G_s(0) = G_n(0) + \alpha|\Psi|^2 + \frac{\beta}{2}|\Psi|^4 \qquad 1.2.1.$$

This expansion is valid near the transition temperature, T_c, when $|\Psi|^2$ is small. α and β are constants to be determined. The equilibrium value of $|\Psi|^2$ is obtained by differentiating 1.2.1 with respect to $|\Psi|^2$ and equating the result to zero:

$$|\Psi_0|^2 = -\frac{\alpha}{\beta} \qquad 1.2.2$$

An additional requirement for stable equilibrium at temperatures below T_c is that

$$\frac{\partial^2}{\partial\{|\Psi|^2\}^2}\left\{G_s(0) - G_n(0)\right\} > 0,$$

i.e., $$\beta > 0 \quad \text{and hence} \quad \alpha < 0 \qquad 1.2.3$$

At the transition temperature,

$$|\Psi|^2 = 0 \qquad \text{and}$$
$$\alpha = 0.$$

The free energy difference per unit volume of the normal and superconducting phases is $H_c^2/8\pi$ which is equal to the area under the magnetization curves shown in Fig. 1 and Fig. 2.

Hence it follows from 1.2.1 and 1.2.2

$$\frac{H_c^2}{4\pi} = \frac{\alpha^2}{\beta} \qquad 1.2.4$$

The application of a magnetic field produces spatial gradients in Ψ which necessitate the inclusion of terms containing $\nabla\Psi$ into the free energy expression. Ginzburg and Landau (2) proposed that the free energy per unit volume of a superconductor in the presence of an applied field H_o should have the form:

$$G_s(H) = G_n(H) + \alpha|\Psi|^2 + \tfrac{1}{2}\beta|\Psi|^4 + \frac{1}{2m}\left|\left(-i\hbar\nabla - \frac{e^*A}{c}\right)\Psi\right|^2 + \frac{H^2}{8\pi} - \frac{H \cdot H_o}{4\pi} \qquad 1.2.5$$

where m and e* have the dimensions of mass and charge respectively. $\underline{H}$ is the local magnetic field and $\underline{A}$ the associated vector potential.

Two important differential equations are derived from 1.2.5 by minimizing the free energy difference with respect to the vector potential $\underline{A}$ and the order parameter Ψ^*.

Minimization of the free energy is a variational problem which may be solved by using Euler's equations (3). Minimization with respect to $|\Psi|^*$ yields one of the G-L equations:

$$\alpha|\Psi| + \beta|\Psi|^2\Psi + \frac{1}{2m}\left(-i\hbar\nabla - e^*\frac{\underline{A}}{c}\right)^2\Psi = 0 \qquad 1.2.6$$

Minimization with respect to $\underline{A}$ yields an expression for the current density:

$$\underline{J} = -\frac{c}{4\pi}\nabla^2\underline{A}$$

$$= -\frac{e^{*2}}{mc}|\Psi|^2\underline{A} - \frac{e^*\hbar}{2im}\left(\Psi^*\nabla\Psi - \Psi\nabla\Psi^*\right) \qquad 1.2.7$$

It is interesting to note that this equation has a similar form to the probability current that appears in quantum mechanics (4) where Ψ is interpreted as a wave function.

Ginzburg and Landau impose the boundary condition that the superelectron velocity is tangential to the surface:

$$\left(i\nabla + \frac{e^*\underline{A}}{\hbar c}\right)\Psi \cdot \underline{n} = 0 \qquad 1.2.8$$

where $\underline{n}$ is a unit vector normal to the surface.

The G-L equations 1.2.6 and 1.2.7 introduce two characteristic lengths, both functions of temperature T; the weak field penetration depth λ (T) and the coherence length ξ (T).

Consider a magnetic field sufficiently weak not to depress the order parameter below its equilibrium value Ψ_o. Equation 1.2.7 can now take the simplified form:

$$\nabla^2 \underline{A} = \frac{4\pi e^{*2}}{mc^2} \quad |\Psi_o|^2 A$$

and shows that a weak magnetic field will penetrate the surface of a superconductor to a depth:

$$\lambda(T) = \sqrt{\frac{mc^2}{4\pi \quad |\Psi_o|^2 \quad e^{*2}}} \qquad 1.2.9$$

Consider the case where by exterior constraints Ψ is made to have a slightly different value from Ψ_o at one point, $\underline{r}$, i.e.,

$$\Psi \longrightarrow \Psi_o(\underline{r}) \left[1 + \theta(\underline{r})\right] \qquad 1.2.10$$

where $\frac{\theta}{\Psi_o} \ll 1$

Substitution of 1.2.10 into 1.2.6 yields a differential equation which has a solution for the one dimensional case of the form:

$$\theta(x) = Ae^{-\sqrt{2}x/\xi} + Be^{\sqrt{2}x/\xi}$$

This equation shows that a small perturbation in Ψ spreads from the centre of the disturbance to a distance:

$$\xi(T) = \frac{\lambda(T)}{\kappa(T)}$$

κ is defined by:

$$\kappa = \frac{mc}{e^*\hbar}\sqrt{\frac{\beta}{2\pi}} \qquad 1.2.11$$

which after substitution of 1.2.2. and 1.2.4 into 1.2.11 becomes:

$$\kappa = \frac{\sqrt{2}\,e^*}{\hbar\, c} H_c \lambda^2 \qquad 1.2.12$$

By finding solutions of the G-L equation, 1.2.6, for which Ψ is very small it is possible to find the conditions necessary for spontaneous nucleation of the superconducting phase in the bulk of the material. By neglecting the term involving $|\psi|^3$, the G-L equation is formally identical to a Schrödinger equation for a particle in a uniform magnetic field. When this equation is solved it follows that the largest field for which $\Psi \neq 0$ is given by:

$$H_{c_2} = \sqrt{2}\kappa H_c \qquad 1.2.13$$

This equation specifies the distinction between type- I and type-II behaviour. If the nucleation field H_{c_2} is less than the thermodynamic critical field H_c type-I behaviour prevails and conversely if H_{c_2} is greater than H_c the material is a type-II superconductor.

The two G-L equations 1.2.6 and 1.2.7 have been derived from the Bardeen-Cooper-Schrieffer (5) (B-C-S) microscopic theory of superconductivity by Gor'kov (6,7) who shows that e^* should be replaced by $2e$, where e is the electron charge. Ψ has the physical significance of being the correlation

function of electron pairs and m is the free electron mass. A consequence of Gor'kov's derivation of the G-L equations is the conditions for which the G-L theory is valid. Firstly, $|\Psi|^2$ must be small if expansion 1.2.1 is to be justified. Secondly, the weak field penetration depth λ must be much greater than ξ_o for a pure metal and for a dirty metal λ must be much greater than $\sqrt{\xi_o l}$, where l is the normal state electron mean free path, ξ_o is the B-C-S coherence length which can be expressed in terms of the properties of the electron gas at the Fermi surface.

$$\xi_o = \frac{0.18 \hbar v_F}{kT_c}$$

where V_F is the Fermi velocity. ξ_o can be roughly interpreted as the size of electron-pairs which are the entities involved in a supercurrent flow. Except for temperatures very close to T_c the weak field penetration depth for pure type-I superconductors is smaller than ξ_o. Thus type-I superconducting behaviour can only be described by G-L theory in a very narrow temperature interval near T_c where λ (T) becomes very large. For a pure type-II superconductor where λ

is greater than ξ_o over the complete superconducting temperature interval then the G-L equations are valid over a larger temperature region. Type-II alloys, where λ is greater than $\sqrt{\xi_o \ell}$, will also have a comparatively large temperature region where the G-L theory is valid. For very dirty type-II alloys in magnetic fields close to a nucleation field, where ψ is small, the G-L theory is approximately applicable at all temperatures.

Gor'kov has derived equations involving ξ and λ, as functions of ℓ and reduced temperature t equal to $\frac{T}{T_c}$. Goodman has expressed these equations in a more convenient though simplified form:

$$\lambda(t) \simeq \lambda_L \left\{ \frac{1 + 0.752\,(\xi_o/\ell)}{2(1-t)} \right\}^{\frac{1}{2}}, \qquad 1.2.14$$

$$\xi(t) \simeq \frac{0.522\,\xi_o}{\left[(1-t)\left\{1+0.752\,(\xi_o/\ell)\right\}\right]^{\frac{1}{2}}} \qquad 1.2.15$$

where $\lambda_L = \left(\frac{m^* c^2}{4\pi N e^2}\right)^{\frac{1}{2}}$

is called the London penetration depth (8). N is the number of

free electrons per unit volume, each of mass m^*.

From these equations Goodman (9) has derived a useful relationship:-

$$\kappa = \kappa_0 + 7.5 \cdot 10^3 \frac{\gamma^{\frac{1}{2}}}{\sigma} \qquad 1.2.16$$

which enables a calculation to be made for the κ value of an alloy of known conductivity σ in the normal state ($ohm^{-1}\ cm^{-1}$). γ is the temperature coefficient of the electronic specific heat in ergs $cm^{-3}\ deg^{-2}$. κ_0 refers to pure material and is equal to $0.96\ \frac{\lambda_L}{\xi_0}$.

1.3 Abrikosov Vortices in Type-II Superconductors

Abrikosov (10) has solved the G-L equations for type-II superconductors where $\kappa > 1/\sqrt{2}$. At the bulk nucleation field H_{c_2} a type II superconductor undergoes a change to the mixed state by means of a second-order phase transition. In perpendicular fields just below H_{c_2} the order parameter is periodic and has the geometry of a lattice which Abrikosov, without rigorous proof, took to be square. The local

magnetic field for such a mixed state varies linearly with $-|\Psi|^2$ between a maximum of H_o (the applied field) at the lattice points and a minimum of

$$H_{min} = H_o - \frac{\sqrt{2}\,(H_{c_2} - H_o)}{2\kappa^2 - 1}$$

at places midway between lattice points.

The total flux associated with each lattice point is one fluxon $\varphi_o = \frac{hc}{2e} \simeq 2 \times 10^{-7}$ gauss-cm^2.

In applied fields well below H_{c_2}, the mixed state is not satisfactorily explained by G-L theory unless the temperature is close to the transition temperature. Fortunately magnetic properties of the mixed state can be interpreted using a simple model where an isolated vortex in a type-II superconductor can be approximated by a normal cylindrical core of radius $\xi(T)$ surrounded by circulating electrons which persist to a distance $\lambda(T)$ from the axis of the core. The magnetic flux associated with the vortex is one flux quantum and the local decrease in magnetic energy is approximately equal to $\pi\lambda^2 \frac{H_o^2}{8\pi}$ per unit length of the vortex line.

The local increase in free energy due to the appearance of a normal core is approximately equal to $\pi \xi^2 \frac{H_c^2}{8\pi}$ per unit length.

This model of fluxons can also be used to calculate the interaction energy of two vortices provided the normal cores do not overlap. Two parallel vortices can lower their mutual free energy by increasing their separation. This repulsive interaction between vortices plays an important role in deciding the structure of the vortex lattice of the mixed state. Careful calculations (11,12) and experiments (13) show that throughout the whole mixed state the most energetically advantageous vortex lattice structure is triangular. The direct observation of vortex lines by Essmann and Träuble (13) reveal that the fluxon lattice is not perfect in practice but is susceptible to various kinds of imperfections. Grain boundaries and stacking faults are observed as a consequence of flux line dislocations. The fluxon lattice contains interstitial and vacancy defects, even large holes where tens of flux lines can be seen missing. In addition to these plastic imperfections there is considerable elastic distortion of the vortex lattice.

1.4 Surface Superconductivity

St James and de Gennes (14) have solved the G-L equationsin the presence of a surface where the boundary condition given by equation 1.2.8 is applicable. Their solution assumes that the bulk dimensions of the specimen are large compared with the coherence length $\xi(T)$ and the temperature T is close to T_c. An additional assumption they make is that the surface polish is sufficiently good that local variations in the radii of curvature of the boundary are large compared with $\xi(T)$.

St James and de Gennes show that the nucleation of superconducting regions in a type-II superconductor should occur near the specimen surface at a field greater than the bulk nucleation field H_{c_2}. For the case they consider, of a magnetic field applied parallel to the specimen surface, a superconducting sheath persists to a field:

$$H_{c_3} = 1.695\, H_{c_2} \qquad 1.4.1$$

above which superconductivity is destroyed.

Experiments described in this thesis are concerned with type-II lead-bismuth alloys. It is perhaps of interest to note that pure lead, although a straightforward type-I material at $4.2^{\circ}K$, exhibits surface superconductivity at lower temperatures as a consequence of the different temperature dependencies of H_{c_3}, H_{c_2} and H_c. Superconductors where $H_{c_3} > H_c > H_{c_2}$ are sometimes called type I-II superconductors. Magnetization curves for pure lead have been plotted by Jones (15) and McEvoy (16) where the presence of the surface sheath above H_c is clearly seen as a tail in their plots of magnetization against H_o.

Exact solutions of G-L equations for fields corresponding to the existence of the surface sheath have been derived by Fink and Kessinger (17) using numerical methods. One property of the surface sheath they calculate is its thickness as a function of the applied parallel field and the G-L parameter κ. (See Fig. 3). They define the sheath thickness, Δ, by the equation:

$$\Delta = \int_0^{\infty} \left[\frac{\Psi(x)}{\Psi(o)} \right]^2 dx .$$

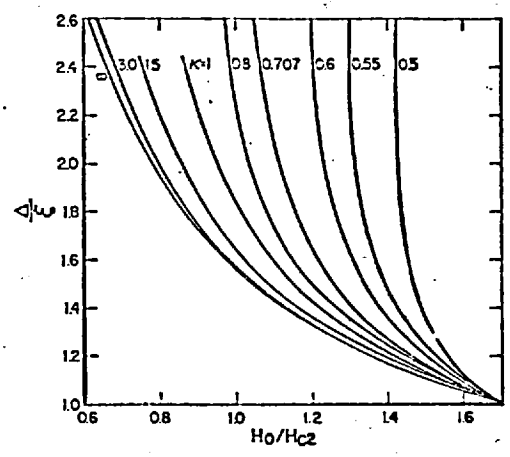

Fig. 3 The thickness of the Superconducting Surface Sheath Δ in units of the Coherence Length ξ as a function of H_o/H_{c_2} and the G-L Parameter κ

$\Psi(x)$ is the order parameter a distance x from the surface of the superconductor. The thickness of the sheath has been measured by Fischer and Maki (18) for the case of the alloy $Pb_{0.91}Bi_{0.09}$ in fields close to H_{c_2}. Their measurements show good agreement with the calculations of Fink and Kessinger.

1.5 Generalization of Ginzburg-Landau Parameters to Describe Superconducting Behaviour at Lower Temperatures

The G-L parameter κ is defined for temperatures close to T_c. In order to cater for temperatures below T_c, Maki introduced temperature dependent parameters $\kappa_1(T)$, and $\kappa_2(T)$ (19) which may be deduced from measurements of the upper critical field $H_{c_2}(T)$, the thermodynamic critical field H_c, and the slope of the magnetization curve near

$H_{c_2}(T)$. The defining relationships for $\kappa_1(T)$ and $\kappa_2(T)$ are:-

$$\kappa_1(T) = H_{c_2}(T)/\sqrt{2}\ H_c(T) \qquad 1.5.1$$

$$\left(\frac{dM}{dH_o}\right)_{H_{c_2}} = \frac{1}{4\pi\beta(2\kappa_2(T)^2 - 1)} \qquad 1.5.2$$

where $\beta = 1.16$ for a triangular vortex lattice . Maki has calculated κ_1 and κ_2 numerically by solving Gor'kov's generalized G-L equations for the case of small normal state mean free paths. The temperature dependence of H_{c_2} as defined by equation 1.5.1 has been calculated explicitly by Helfand and Werthamer (20) for arbitrary electron mean free paths, ℓ. Fig. 4 shows their plot of $h^* = \frac{H_{c_2}}{-(dH_{c_2}/dt)t=1}$ versus reduced temperature t where $\lambda' = 0.882\,\xi_o/\ell$

An experimentally useful calculation they make is the dependence of mean free path on the slope of H_{c_2} (t) curves near t=1.

Tewordt (21) has developed a generalized G-L theory of superconducting alloys which is applicable for an extended

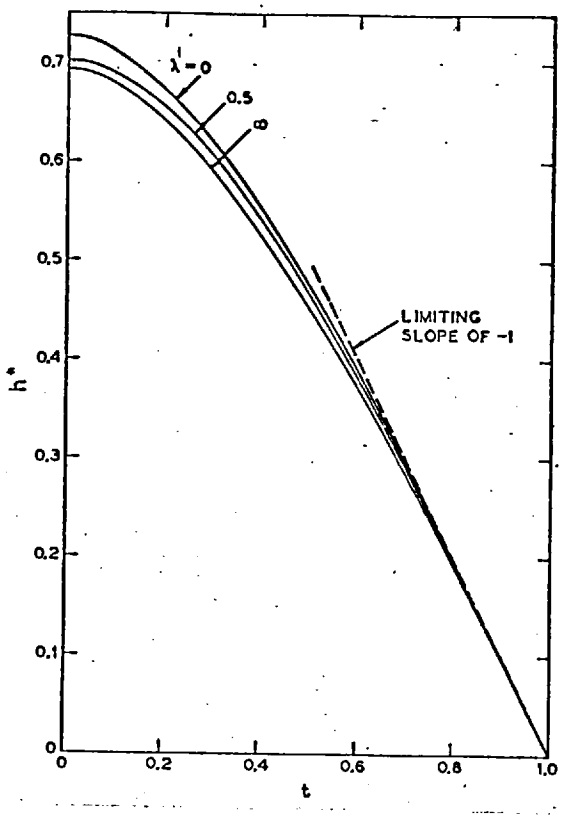

Fig. 4 The Critical Field Reduced so as to have a slope of -1 at t=1, as a function of reduced temperature and purity

range of both the reduced temperature and order parameter. Tewordt (21) includes fourth order terms in the expression for the Gibbs free energy difference of the superconducting and normal phases. From this theory Ebneth and Tewordt (22) have calculated the ratio H_{c_3}/H_{c_2}:

$$\frac{H_{c_3}(T)}{H_{c_2}(T)} = 1.695 + \delta\left(1 - \frac{T}{T_c}\right) \qquad 1.5.3$$

where δ is a function of the normal state electron mean free path l. In the dirty limit $l \to 0$ and $\delta \to 0$. Implicit in Tewordt's generalized G-L theory is that the electron pair scattering at the surface is specular. For the general case of surface reflection which is a combination of specular and diffuse scattering Usadel and Schmidt (23) have calculated the ration $H_{c_3}(T)/H_{c_2}(T)$ for arbitrary l at T=0 and for an extended range of temperatures below T_c. For $t=\frac{T}{T_c}$ not too far from unity,

$$\frac{H_{c_3}(t)}{H_{c_2}(t)} = 1.695\left[1 + pa_1(1-t)^{\frac{1}{2}} + a_2(1-t)\right] \qquad 1.5.4$$

with $a_1 = 0.205\left(\frac{l}{0.875\,\xi_o}\right)^{\frac{1}{2}}$

and $a_2 = (0.548 - 0.409p + 0.083p^2)\frac{l}{0.875\,\xi_o}$

For t=0,

$$\frac{H_{c_3}(0)}{H_{c_2}(0)} = 1.695\left[1 + 0.171p\left(\frac{l}{0.875\,\xi_o}\right)^{\frac{1}{2}} + (0.379 - 0.283p + 0.058p^2)\left(\frac{l}{0.875\,\xi_o}\right)\right] \qquad 1.5.5$$

The parameter p is the degree of diffuseness of surface scattering and is restricted by

$$0 \leqslant p \leqslant 1$$

The ration $H_{c_3}(t)/H_{c_2}(t)$ has been measured by Maki and Fischer (18) on $Pb_{0.91}Bi_{0.09}$ in a temperature interval $0.4 \leqslant t \leqslant 1$. There is close agreement with theory when p=0.

CHAPTER II

PROPERTIES OF TYPE - II SUPERCONDUCTORS IN THE PRESENCE OF TRANSPORT CURRENTS

2.1 Introduction

When transport currents above a critical level are introduced into type-II superconductors in the mixed state, resistance appears and a voltage is developed along the direction of current flow. The source of this resistance has been studied using microscopic theory by Caroli and Maki (27). They considered only fields near H_{c_2} in the dirty and clean limits of the electron mean free path. The microscopic theory takes no account of flux pinning.

It is proposed in section 2.2 of this chapter to consider irreversible behaviour with a flux pinning model where resistance appears as a result of the dissipative motion of vortices. In subsequent sectionsthe concept of a critical current is reviewed in the special case where fields are applied parallel to specimen surfaces.

2.2 Application of Transport Currents to Type-II Superconductors in the Mixed State

If a magnetic field is applied perpendicular to the surface of a type-II superconducting film it will enter the mixed state at a field $H^*_{c_1} < H_{c_1}$ and will persist to a field H_{c_2}. The initial penetration field is less than H_{c_1} because of demagnetization effects. When a transport current is applied to such a film a force acts on the vortices; but for small applied currents the fluxons cannot move because, it is believed, they are pinned by inhomogeneities in the metallurgical structure of the superconductor (24). These inhomogeneities, distributed throughout the material, modify the free energy of the vortex array such that there are free energy minima for certain relative positions of the vortex lattice and the pinning centres (25).

The driving force per unit length of a pinned flux line has been derived by a thermodynamic argument by Friedel et al (26). Its magnitude has the form of the Lorentz force equation:

$$\text{i.e.,}\quad \underline{F_L} = \underline{J} \wedge \frac{\phi_o}{c} \qquad 2.2.1$$

where $\underline{\varphi_o}$ is the flux quantum and $\underline{J}$ is the mean current density near the flux line. When the transport current is sufficiently large to overcome pinning forces the vortices undergo a viscous flow in a direction which makes an angle α with the transport current as shown in Fig. 5

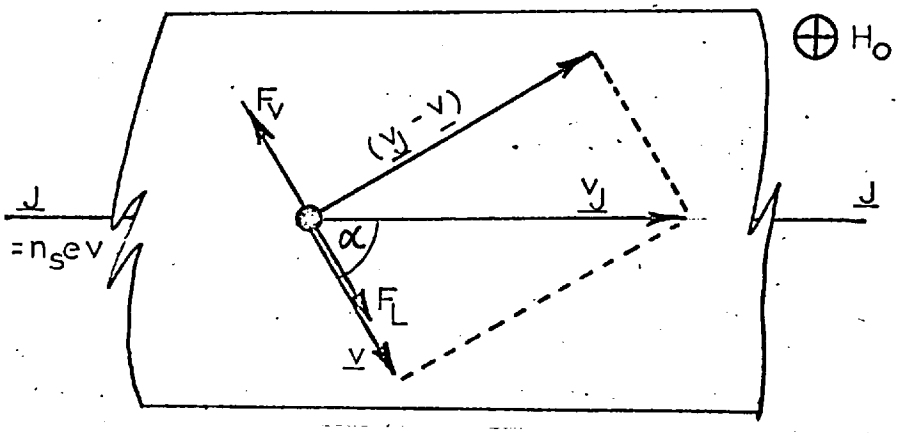

Fig. 5 Velocity and Force Diagram for Vortex Motion through Mixed State. The applied Field H_o is directed into the Plane of the Page

In order to maintain a steady state the viscous drag experienced by a moving flux line, $F_{\underline{v}} = \eta \underline{v}$, must be equal and opposite to the "Lorentz force" acting on the moving flux line, i.e.,

$$| v_{\underline{J}} - \underline{v} | n_s e \varphi_o = \eta v \quad (28, 29, 30)$$

where $\underline{v_J}$ is the velocity of the electrons carrying the transport current, η is a "viscosity constant" and v is the velocity of a vortex through the material.

It follows from Fig. 5 that:

$$\alpha = \tan^{-1} \frac{\eta}{n_s e \phi_o}$$

Experiments by Niessen and Staas (31) on superconducting alloys indicate that for dirty material η is large and flux flow is nearly perpendicular to the applied current. Since the vortices have to overcome viscous resistance during their motion a power input is required to maintain a steady state and the specimen will develop a voltage, V, along its length:

$$V = \underline{E} \cdot \underline{b}$$

where

$$\underline{E} = (\underline{v} \wedge \underline{B})/c \qquad (32, 33)$$

$\underline{E}$ is the effective field in the superconductor and B is the average flux density. $\underline{b}$ is the vector distance between

the two potential leads. Kim et al (34) have shown that current-voltage characteristics in the flux flow regime are linear and they have fitted the relationship:

$$\underline{E} = \rho_f (\underline{J} - \underline{J}_o) \qquad 2.2.4$$

to their experimental results where ρ_f is the flux flow resistivity defined by:

$$\rho_f = \frac{dE}{dJ} \qquad 2.2.5$$

The flux flow resistivity shows good agreement with the empirical relationship:

$$\frac{\rho_f}{\rho_n} = \frac{H_o}{H_{c_2}} \qquad 2.2.6$$

where H_o is the applied field and ρ_n is the normal state resistivity. Kim et al (34) suggest that this result follows if the electrical resistance is contributed by the normal cores and the current does not avoid them. They reach this conclusion by considering a high κ model (35) where the

penetration depth λ is much greater than ξ and the normal core can be approximated by a cylinder of radius ξ. For such a model H/H_{c_2} represents the fraction of the total volume occupied by normal material.

It is important to point out that according to the flux creep theory of Anderson (36) flux pinning is not absolutely rigid at finite temperatures since thermal activation can cause flux lines to leave their potential wells. Vortices are able to move past pinning centres even in very small currents. In this flux creep regime the induced electric field E varies approximately exponentially with the transport current J. At a sufficiently high current level flux flow predominates and the voltage-current characteristics are linear.

2.3 Critical Currents for Type-II Superconductors in Parallel Fields

Consider a type-II superconductor which has a rectangular geometry with a transport current flowing along its longest dimension and a magnetic field applied parallel to the surface of the material, perpendicular to the applied current. In fields just below H_{c_2}, the superconductor will be in the mixed

state and a model based on flux flow and pinning will be appropriate. Above H_{c_2}, the bulk of the material is normal and only a superconducting surface sheath exists. The criterion for the appearance of resistance at a critical current for such a configuration is not well understood. Critical current may be defined as the current corresponding to the appearance of a given measurable voltage.

2.4 The Maximum Current Density for which Solutions of the G-L Equations can be found

Abrikosov (37) assumes that the measured critical current corresponds to the maximum current density for which solutions of the G-L equations can be found. He takes a modified Gaussian error curve to be a good approximation to the solution of the G-L equations. For temperatures close to the transition temperature, T_c, and for penetration depths large compared with the surface sheath thickness the critical current density is related to the applied fields H_o through the equation:

$$J_c = \frac{5H_c}{3\sqrt{3\pi K}} \left(1 - \frac{H_o}{H_{c_3}}\right)^{3/2} \qquad 2.4.1$$

provided H_o is not too far from H_{c_3}.

Park (38) has repeated Abrikosov's calculations with the added refinement that he does not make an approximation to ψ. In this case exact solutions of the G-L equations are found by numerical methods which are valid close to T_c in the range from just below H_{c_2} to H_{c_3}. Park considers paramagnetic and diamagnetic transport currents in a rectangular strip where surface superconductivity is destroyed on one of the surfaces. A transport current is defined as being diamagnetic and positive when it flows in the same direction as the outmost shielding current and conversely it is paramagnetic and negative when flowing in the opposite sense. These shielding currents, which have been calculated by Fink (39), are shown in Fig. 6. Park's solutions shown in Fig. 7 reveal that the diamagnetic critical current is less than the paramagnetic one. The latter shows reasonable agreement with the results of Abrikosov.

In the above theory it is assumed that the weak field penetration depth is much greater than the thickness of the surface layer so that the internal field H can be taken to be uniform throughout the sheath and equal to the external

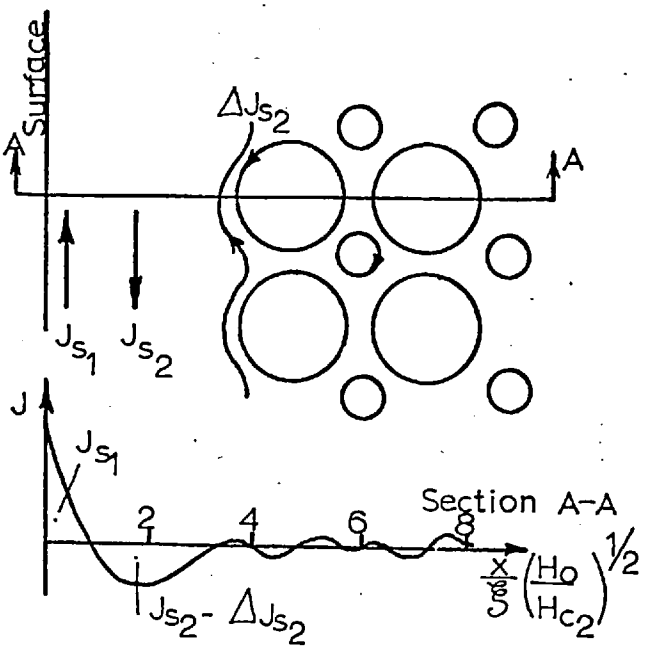

Fig. 6 The Schematic distribution of the Internal Currents for a Type-II Superconducto where $H_o < H_{c_2}$ and $(H_{c_2} - H_o)/H_{c_2} \ll 1$

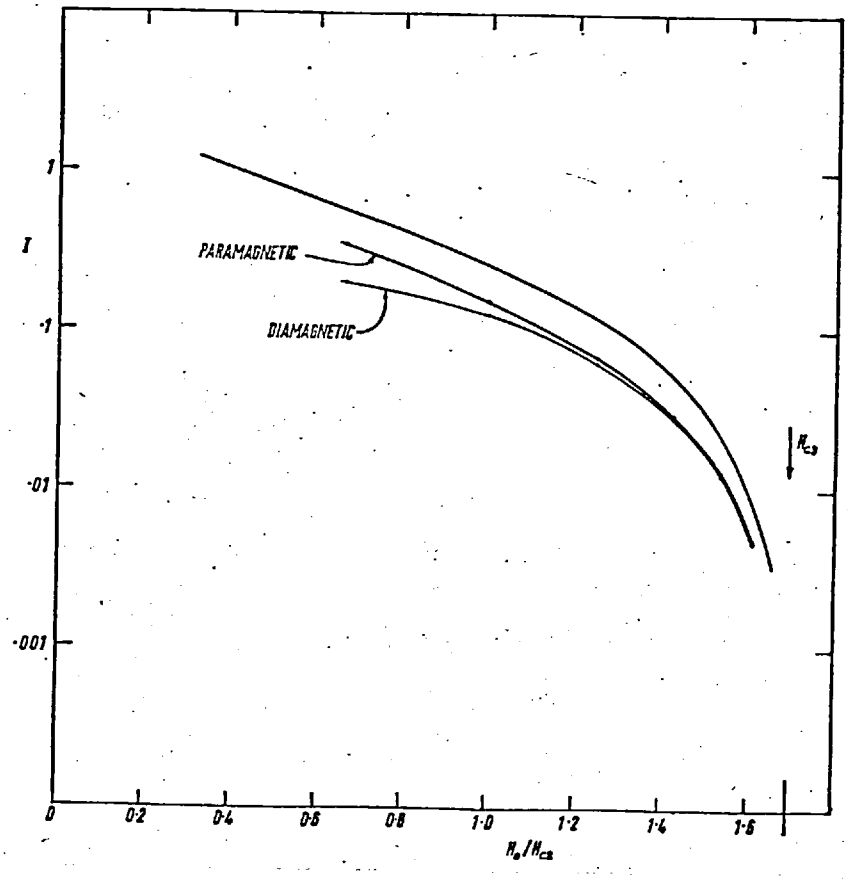

Fig. 7 Variation of Critical Surface with Reduced Field H_o/H_{c_2} as given by Abrikosov's calculation (upper curve) and by Park. $\kappa \gg 1$, $J_c = IH_c/\kappa$ A/cm

if there is no transport current.
field H_o/ This implies $\kappa \gg 1$. However Fink (39) points out that when the G-L parameter κ is greater than 3 the maximum deviation of the internal magnetic field from its external value is smaller than 2%.

The critical surface-sheath currents calculated by Abrikosov (37) and Park (38) are considerably greater, by at least one order of magnitude, than experimental results (40).

2.5 Infinite Cylinder Model

Fink and Barnes (41), and Park (42) have attempted to calculate the maximum current induced in the surface sheath of an infinite cylinder. These calculations are based on the hypothesis that the current can be treated as uniform and when the current is critical the free energy of the superconducting state (G_s) has the same value as the normal phase free energy (G_n) in the same applied field. From these same assumptions Fink has calculated the critical transport current density in a rectangular strip of width ω:

$$J_c = \frac{c}{2\sqrt{\pi}} \left(\frac{\beta}{\ln 4\kappa - 1}\right)^{5/4} \left(\frac{2}{\omega}\right)^{1/2} \left(\frac{\hbar}{2\sqrt{2}e}\right)^{1/4} \left(\frac{H_c}{\kappa}\right)^{3/4} \left(\frac{\Delta}{\xi}\right) F^2(0) \qquad 2.5.2$$

where $\beta \approx 1$. F(0) is the value of the normalised order parameter at the surface of the sheath. $\frac{\Delta}{\delta}$ and F(0) have been calculated by Fink and Kessinger (17) as functions of κ. These calculations are illustrated in Fig. 3 and Fig. 8 below:

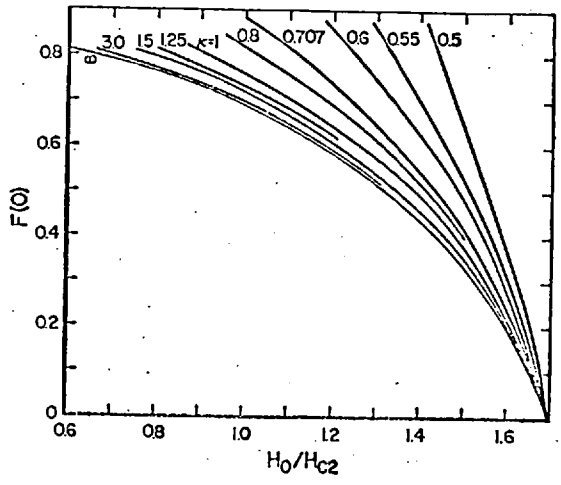

Fig. 8 The Absolute Value of the Normalised Order Parameter at the Boundary Surface

The magnitude of the total critical current $I_c = J_c \omega$ calculated from equation 2.5.2 shows reasonable agreement with an experiment of Hart and Swartz (43). However, the effect of variations in the width were not examined and so the assumptions pertaining to this equation were not rigorously tested.

2.6 The Hart and Swartz Surface-Flux-Pinning Model

In sections 2.2 - 2.5 it is assumed that the resultant magnetic field influencing the specimen is everwhere parallel to its surface. Misalignment of the applied field with the specimen surface can result in a perpendicular component of the magnetic field. Also the transport current through the sheath can contribute a perpendicular component. Hart and Swartz (44) postulate that magnetic flux can penetrate the sheath in the form of a quantized array of flux spots. Imperfections in the surface structure of the superconductor act as pinning centres and to set the flux spot array in motion requires the presence of a driving force. At some current level the "Lorentz force" exceeds the pinning force and a voltage is induced as a result of flux flow. If the critical surface transport current is determined by flux pinning a local surface region is said to be in the critical state when it carries its maximum current density. A sample critical surface current is reached only when the entire flux spot array can move as an entity, i.e., when every surface region is in the critical state.

The local current distribution across the width of a

type-II superconducting strip must be self-consistent with the local perpendicular component of the magnetic field. If the local field is everywhere parallel to the film surface the current distribution is peaked at the edges as calculated by Bowers (45). In this surface-flux-pinning model the perpendicular component of the local field is only zero along a centre line of the two surfaces of the film provided the applied field has no perpendicular component. At this position the current density has its maximum value J_o. The critical current density elsewhere $J_c(H_p)$ decreases with increasing perpendicular field component, being a minimum near the film edges. When the surface critical state is reached the local perpendicular field is determined from the equation:

$$H_p(x) = P\int_{-\frac{\omega}{2}}^{\omega/2} \frac{2J_c\left[H_p(x^1)\right]}{c(x-x^1)}\, dx^1 \qquad 2.6.1$$

where x is the distance from the centre of the strip (width ω) measured normal to the current, so that the edges are at $x = \pm \frac{\omega}{2}$. P indicates that the principal part of the integral is taken. Hart and Swartz solve equation 2.6.1 for

one special case, taking for $J_c(H_p)$ the function:

$$J_c(H_p) = J_o/(1 + H_p/H_a) \qquad 2.6.2$$

where H_a is a constant determined by the strength of pinning. The total measured critical current is given by:

$$I_c = \int_{x=-\frac{\omega}{2}}^{\omega/2} J_c(x)\, dx \qquad 2.6.3$$

The model predicts a total surface critical current which is linear with the strip width and independent of its thickness. Experiments by Hart and Swartz have been consistent with their model. They have made I_c measurements for a single surface, surface superconductivity on the other surface being destroyed by the proximity effect of copper (46). For a single surface the diamagnetic critical current as defined in section 2.4 is greater than the paramagnetic critical current. The ratio of the two currents for a parallel field is of the order of 1.4 and becomes a maximum of about 1.7 when the specimen is rotated through an azimuthal angle φ of about 0.2 degrees. Fig.9 on page 46 shows the geometry of the specimens together with field and current directions.

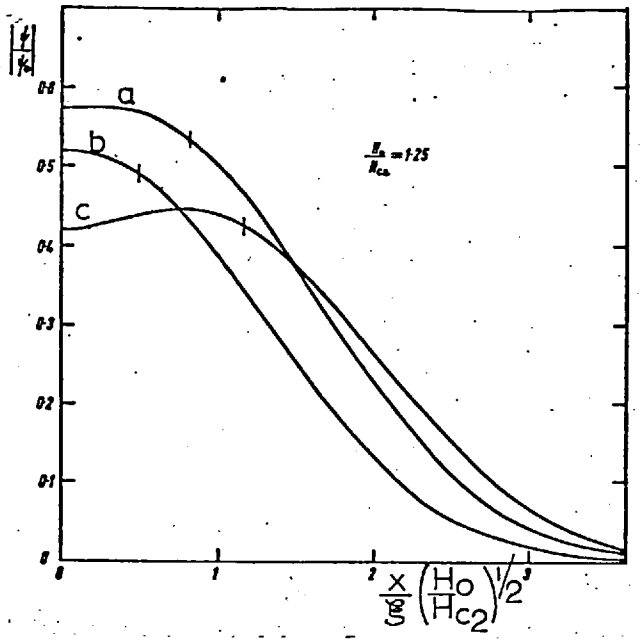

Fig. 10 Variation of the Order Parameter with depth below the surface given by x. (a) zero transport current
(b) paramagnetic critical current
(c) diamagnetic critical current

The explanation for rectification, based on a flux pinning model, is that the depth below the surface to which an intercepting flux thread persists and thus the length of the flux line which is pinned is greater for a diamagnetic current than for a paramagnetic current as shown in Fig. 10 above.

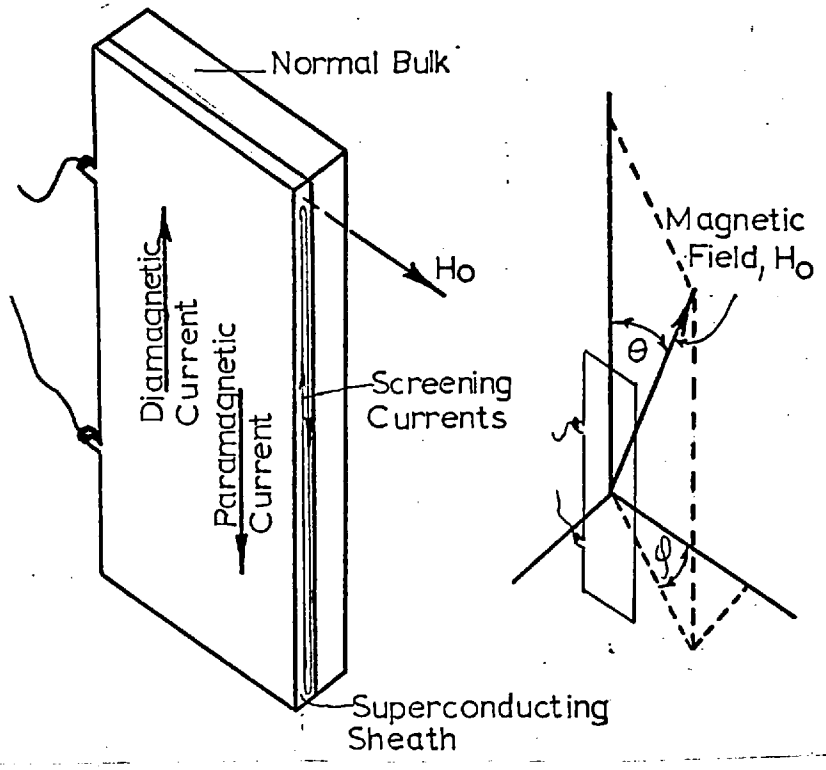

Fig. 9 The Definition of Polar Angle θ and Azimuthal angle φ. The Case of $\theta = 90^{\circ}$, $\varphi = 0^{\circ}$ is also shown

Hart and Swartz find for their evaporated films that the critical surface currents decreased by a factor of two when the applied magnetic field is turned out of the plane of the surface by only a few tenths of a degree. For small variations in the azimuthal angle Φ the sample critical current varies roughly as

$$\frac{1}{I_c} = \frac{1}{I_o} + b \sin \Phi \qquad 2.6.4$$

Qualitative measurements have been made on the effect of

surface roughness. It would appear in general that slight roughness given to a surface by imperfect polishing or surface contaminants increases the critical current density relative to the low critical currents obtained for well polished surfaces. It is probable that surface roughness can influence the critical current in two ways. Firstly, increased surface roughness is expected to increase the local value of the G-L parameter which should result in a decrease of the critical current if the dependence of J_c on κ is approximated by the theories of Barnes and Fink (41) and Park (42). Secondly, according to Hart and Swartz, surface irregularities are a source of the free energy wells which pin flux lines. Thus if a polished specimen is roughened the critical current should increase. Experiments suggest that the effects due to the latter explanation dominate.

CHAPTER III

PREPARATION AND STRUCTURE OF SPECIMENS

3.1 Specimen Composition

Experiments described in this thesis were concerned with alloys of the Pb-Bi system covering a composition range from 1 to 15 atomic per cent of bismuth. In this range the alloy forms the solid phase, α, which is a continuous solid solution of the random substitutional type (47). The face centred cubic crystal structure of the alloy was observed at room temperature from an electron diffraction pattern with a thin film containing 5 atomic % of bismuth. Experiments by Malseed and Rachinger (48) imply that the α phase persists to 17.4 atomic % bismuth at liquid helium temperatures. The boundaries between equilibrium phases from their data is shown in Fig. 11.

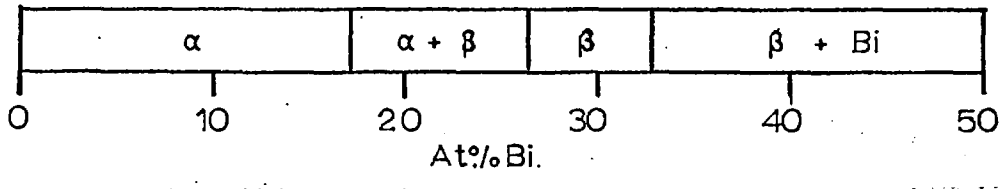

Fig. 11 Equilibrium Phases for Pb-Bi System

3.2 Homogeneity of Evaporated Pb-Bi Films

The evaporation temperatures, T_p, corresponding to a vapour pressure of 10 microns of mercury are similar for lead and bismuth (49)

$$T_p \text{ (Pb)} = 718^{\circ}C$$
$$T_p \text{ (Bi)} = 698^{\circ}C$$

This suggests that these metals can be evaporated from a single source with reasonable certainty that composition gradients will be small in the resultant film. Kopf (50) compares the transition temperatures, T_c, of foils and evaporated Pb-Bi films of similar average compositions. His films, 2000 Å thick, were evaporated at an initial pressure of 5×10^{-7} Torr on to glass substrates at room temperatures. For compositions up to 20 atomic % Bi, T_c for a film was slightly lower than that for the corresponding foil sample; the largest deviations between transition temperatures were about 1%. Kopf concluded that useful homogeneous alloy films can be prepared from a mixture of lead and bismuth evaporated from a single source.

3.3 Substrate and Mask Cleaning Procedure

Evaporated films of the Pb-Bi system were deposited on freshly cleaned soda glass microscope slides. Films deposited on substrates which had not been subjected to a cleaning procedure tended to show streaks and blemishes or in some cases had a uniform appearance but poor optical reflectance. Since contamination of the films might well result in variations of their superconducting properties a standardised cleaning procedure was adopted:-

(i) Detergent wash

(ii) Immersion in concentrated nitric acid

(iii) Immersion in hydrogen peroxide

Each operation was followed by a distilled water rinse. The slides were dried in a hot air stream given a gentle pass through an oxidizing gas flame, cooled and then rinsed in distilled water. If there was no water "break" the slides were considered fit for use and dried again; otherwise the whole procedure was repeated.

3.4 Film Geometry

The geometry of the specimens was defined by evaporation through a stainless steel mask in contact with the glass substrate

The structure of the mask is shown in Fig. 12 together with the specimen shape it produced.

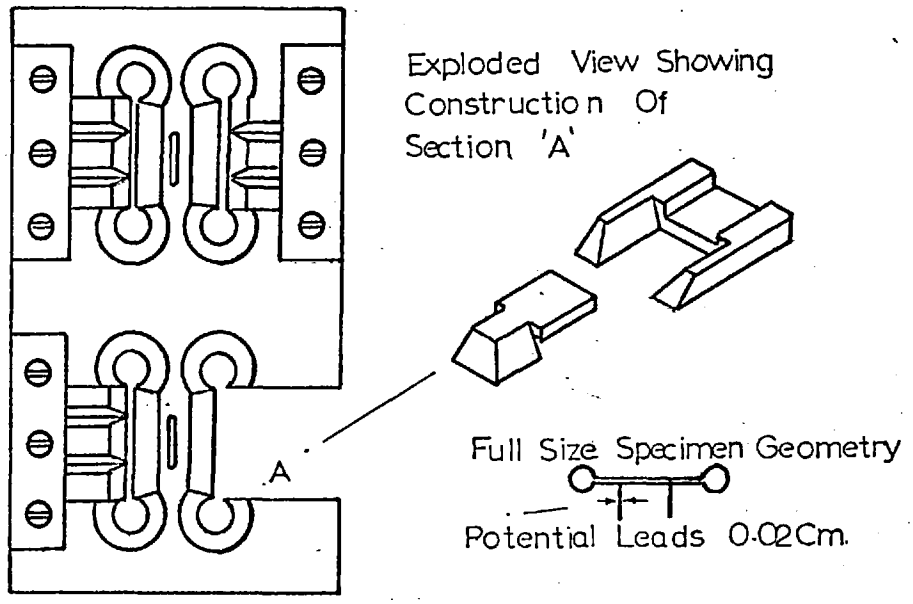

Fig. 12 Structure of Evaporation Mask

The underside of the mask had been machined and lapped to a high degree of flatness to ensure close contact with the substrate to minimize penumbra effects.

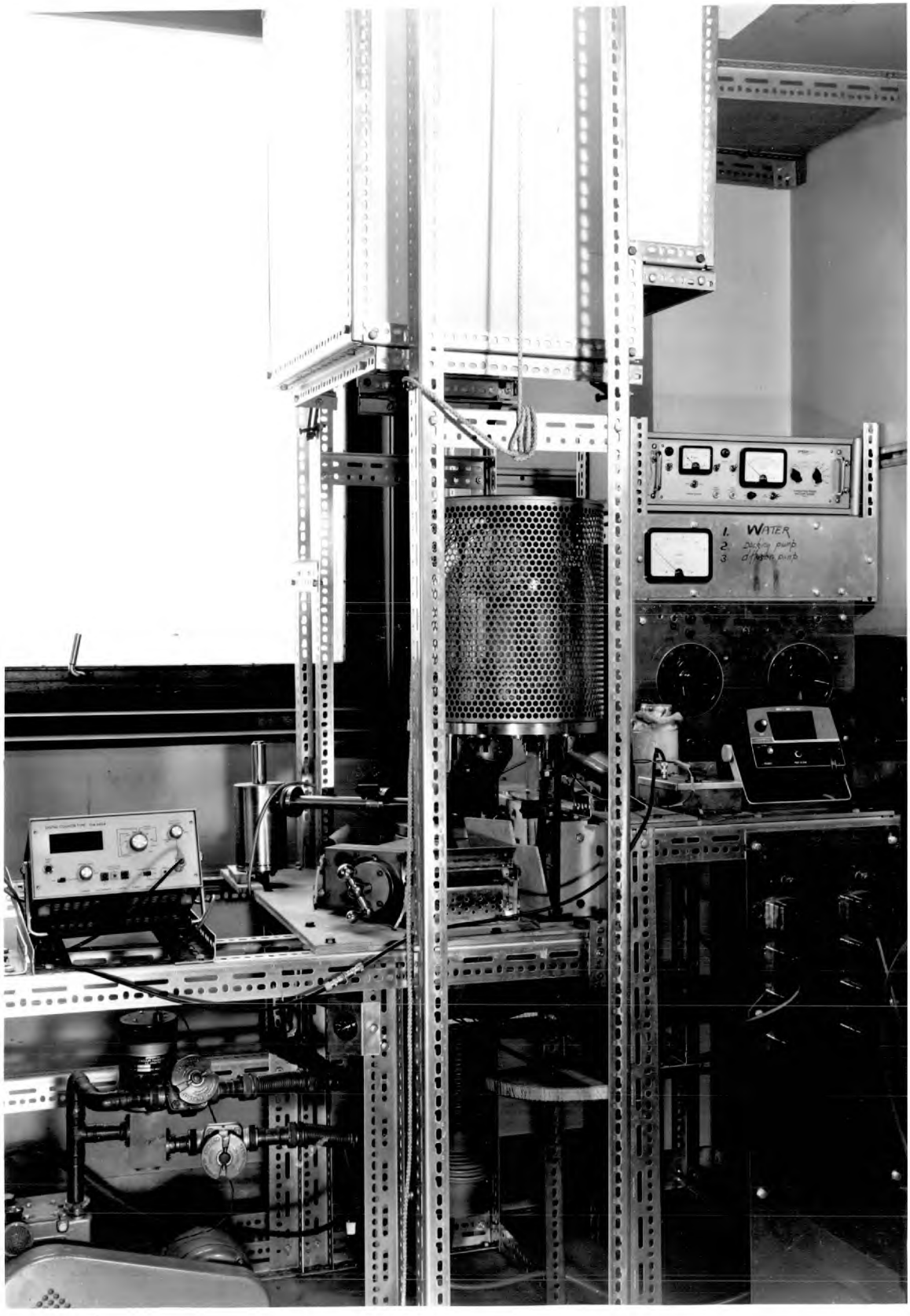

Plate 1. Evaporator

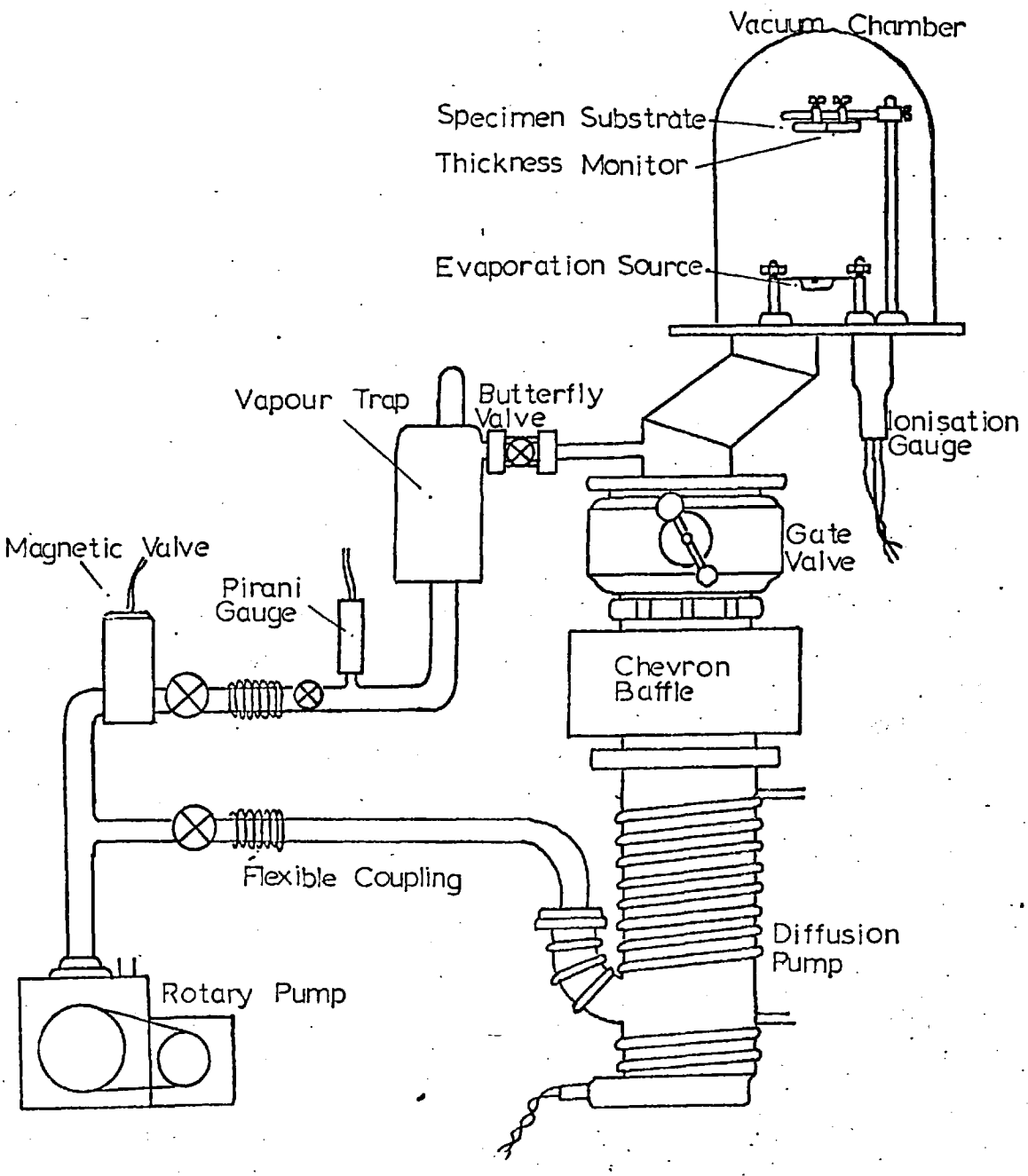

Fig. 13. General Layout of Evaporator

3.5 Description of the Evaporator

Plate 1 shows the detail of the evaporator assembled for the work described in this thesis. A schematic diagram, Fig. 13, gives the general layout of the evaporator components. The base plate of the evaporating chamber and other high vacuum regions were constructed mainly from stainless steel because of its good high vacuum properties (51). To facilitate heating of evaporation sources and the monitoring of evaporation parameters several insulated electrical inputs were inserted into the base-plate of the vacuum chamber. Four electrodes were used for supplying current to two independent evaporation sources and two mechanical inputs were introduced to allow movement of screens between sources and substrate. Viton "O" rings capable of withstanding temperatures of 120°C without detriment ensured high vacuum seals for these inputs. Temperatures of this order were used to "bake" out the chamber and its contents prior to evaporation. After a day of outgassing at 120°C it was possible to achieve ultimate pressures approaching 10^{-7} Torr. "Baking" was effected by lowering an asbestos oven over the evaporation chamber.

Evacuation was by means of a 4 inch diffusion pump (C.V.C.

type PMC-4B) of quoted pumping speed 690 litres/sec. Because of the impedance of the interconnecting gate valve (C.V.C. type VCS-41B) and chevron baffle (C.V.C. type BCN-41A) the pumping speed at the chamber orifice was reduced to 150 litres/sec. To prevent overheating of the pump oil (Convalex 10) a thermostat was fitted to the cooling system of the diffusion pump. Pressures in the backing line and vacuum chamber were recorded with a "Speedivac" Ionisation-Pirani Gauge, Model 1. The Pirani guage head (type 6A) was used for pressures down to 10^{-3} Torr. The ionisation guage head (type IG3K) recorded pressures in the chamber for a range extending from 10^{-3} to 10^{-8} Torr.

3.6 Evaporation Procedure

Specimens were prepared from small pellets of lead and bismuth nominally 99.999% pure mixed in known proportions to a total mass of 1.2 gms. The tantalum evaporation boat is illustrated in Fig. 14.

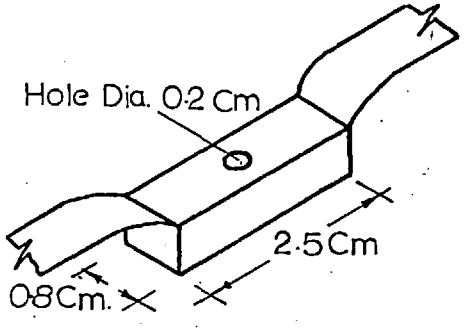

Fig. 14 Evaporation Boat

Vapour emission through the aperture in the boat can be treated as an approximation to emission from a Knudsen surface source (49). The thickness of the evaporated deposit from such a source is given by

$$t = \frac{m}{\pi \rho} \quad \frac{1}{h^2}$$

where m is the mass of the contents of the boat evaporated to completion. ρ is the density of the film and h is the distance separating source and substrate - in this case 15.0 cms. This method of thickness estimation was only a rough guide which agreed to within 40% the thickness measured by more precise optical interference methods. ρ was taken to be that of pure lead for low concentrations of bismuth. ρ can be estimated more accurately by using the relation:

$$\rho = \frac{\text{weight of atoms in unit cell of crystal}}{\text{volume of unit cell}}$$

The volume of the unit cell requires knowledge of changes in lattice parameter with composition which according to Vegard's law may be estimated by linear interpolation (47).

The processing chamber and its contents were usually outgassed for 2 or 3 hours at 120°C by lowering the oven before commencement of evaporation. Evaporation was initiated at a pressure of 5×10^{-6} Torr by passing a current of slowly increasing magnitude through the boat until a thickness monitor (described in section 3.8) registered the commencement of deposition. The current was then increased further until an evaporation rate of 100 Å/sec was recorded. The lead and bismuth were evaporated together at this rate with a current of some 70 Amps flowing through the boat. When the contents of the boat neared exhaustion the evaporation rate dropped significantly at which stage the current was switched off to prevent possible contamination due to overheating.

3.7 Specimen Annealing

Films were approximately 10,000 Å thick. Since a small composition gradient across the thickness was probable, the specimens were annealed for 1 hour at 150°C in a vacuum better than 5×10^{-5} Torr. Fig. 15 shows the variation of diffusion coefficient as a function of temperature for the diffusion of bismuth in lead extracted from the data of Seith and Laird (52)

who made direct measurements of concentration gradients by spectographic techniques for the alloy $Pb_{0.98}Bi_{0.02}$.

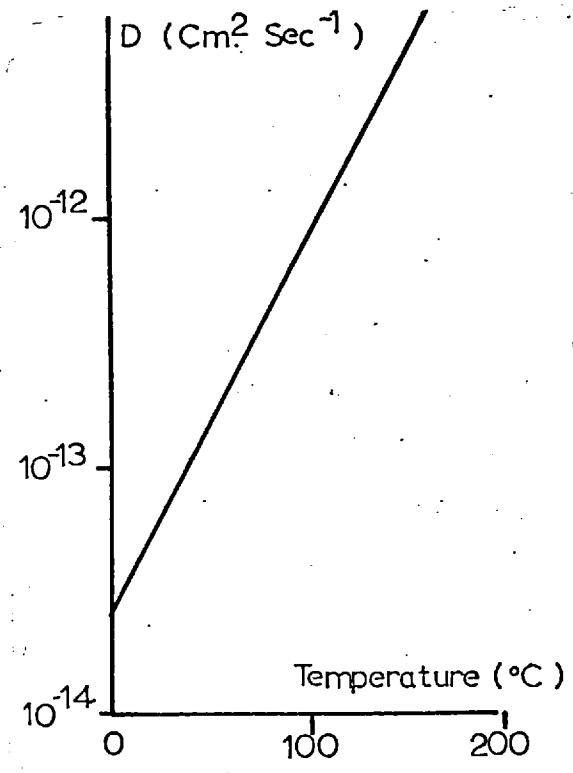

Fig. 15 Variation of Diffusion Coefficient, D, as a Function of Temperature for Bismuth in Lead

The quantity $\sqrt{Dt}$ is an important quantity in diffusion since it gives roughly the distance over which the concentration can change substantially during a diffusion anneal of t seconds. It would take the order of 100 hours for a room temperature anneal to be successful for a 10,000 Å thick film. However, a diffusion anneal of one hour at 150°C should be sufficient to ensure homogeneity of composition across the thickness of a 10,000 Å film.. In this case $\sqrt{Dt}$ = 12,500 Å.

Annealing was achieved by transferring the specimens, after deposition, to a furnace (within the chamber) fabricated from 0.0025 inch tantalum sheet bent into a box slightly larger than the substrate. A current of about 20 Amps through the box was sufficient to raise the temperature of its interior to 150°C.

3.8 Monitoring of Evaporation Rates

The circuit for the electronics of the thickness monitor is shown in Fig. 16

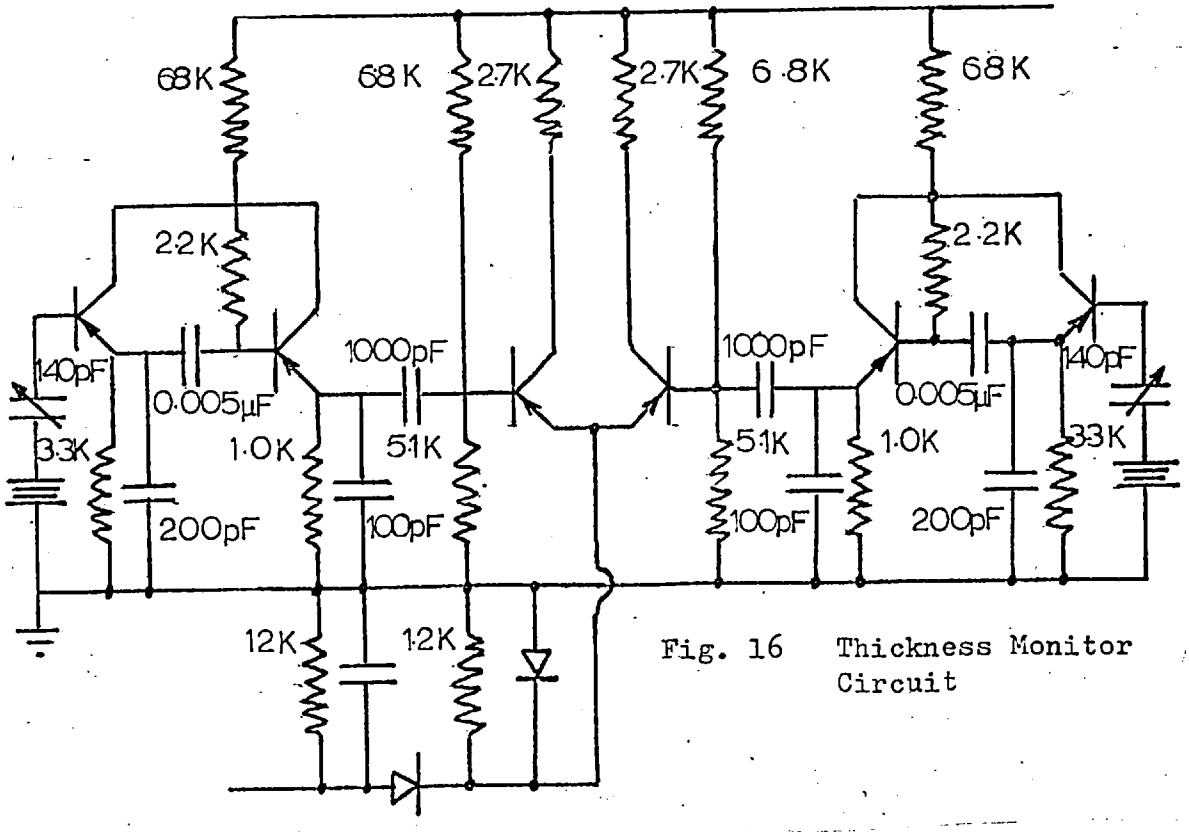

Fig. 16 Thickness Monitor Circuit

The two AT cut quartz crystals , nominally 1 MHz, were mounted side by side next to the film substrate as shown in Fig. 13. One of the crystals was masked from the vapour stream and the other was exposed to allow deposition of the evaporant and a change in the crystal's natural vibration frequency. The signals from the two oscillators were mixed by the differential amplifier and subsequently fed via rectifying and low pass filter networks to a digital frequency meter (Venner type T.S.A. 6634). The change in frequency was proportional, to within 20%, to the thickness of material deposited. 5 Å of lead was equivalent to a frequency change of 1 Hz. Although this device was useful for estimating evaporation rates it was not considered sufficiently accurate for absolute determination of film thickness.

3.9 Measurement of the Thickness of Films

The thicknesses of the specimen films were determined using an optical interference method. A 100 Å layer of silver was evaporated over the microscope slide supporting the films. According to Tolansky (53) this layer follows the contours of the surface to within 10 Å. A plain microscope slide was prepared in a similar fashion so that an air wedge could be formed from the two slides as indicated in Fig. 17.

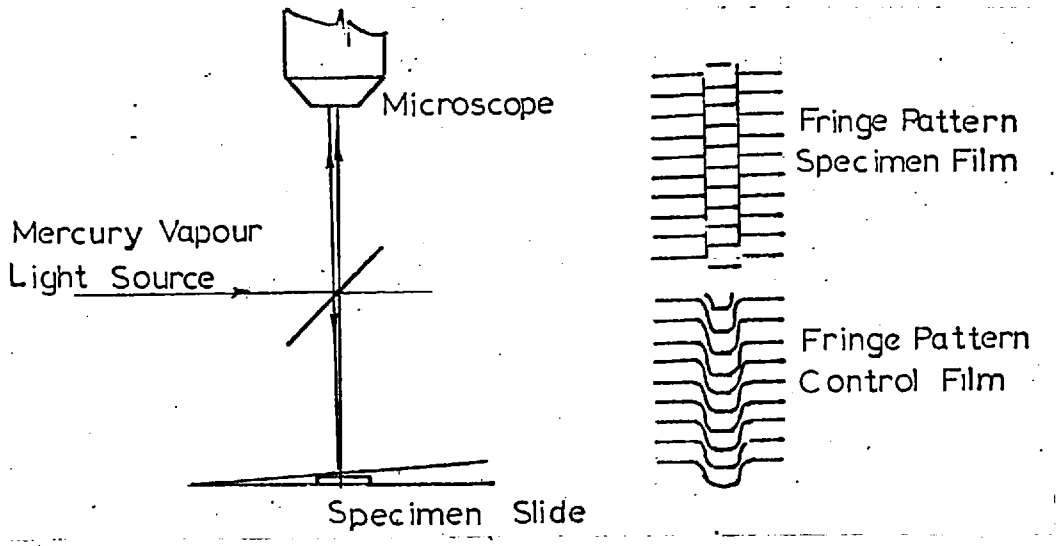

Fig. 17 Observation of Localized Fringes of Equal Thickness

The wedge was illuminated with a collimated beam of light from a mercury vapour lamp. A 45 degree glass reflector plate was placed between the slides and objective of a low power microscope through which the reflection interference fringes could be observed. The fringe displacement, n, of the mercury green line (wavelength λ = 5460 $\mathring{A}$) corresponding to the discontinuity at the specimen edges was measured and the film thickness, t, calculated from: $t = \frac{n\lambda}{2}$. t was deduced by taking the mean of repeated measurements of the fringe displacement. The standard error of the mean was never more than 1%. To determine the order of the fringe displacement additional measurement were made on a control film where there was a gradual

gradient in the thickness of the film near its edges enabling the fringe system to be followed as it passed from the specimen film to the bare substrate. This control film was formed by evaporating through the slits cut in the evaporation mask. The underside of these slits were bevelled so that the mask was effectively out of contact with the substrate.

3.10 Film Trimming

The edges of the specimens were trimmed, since untrimmed films exhibited unusually large parallel transition fields. This was attributed to a gradient in the film thickness near the edges so that when the thickness approached the superconducting penetration depth, a parallel field greater than H_{c_3} was necessary to quench the superconducting state. The reason for the sloping nature of the specimen edges could not be explained in terms of penumbra phenomena, especially since precautions were taken to avoid such effects. More probably, the sloping edges were caused by metal atoms penetrating beneath the mask due to their high surface mobility as suggested by Caswell (51) who has studied the influence of evaporation conditions on superconducting properties. His experiments indicate that it is unlikely that the presence of gas molecules should influence

the bulk superconducting properties of a film for evaporation at a pressure of 5×10^{-6} Torr. However, the pressure of oxygen molecules may affect the surface mobility of metal atoms and consequently influence the edges of a specimen.

Fig. 18 shows how the films were trimmed

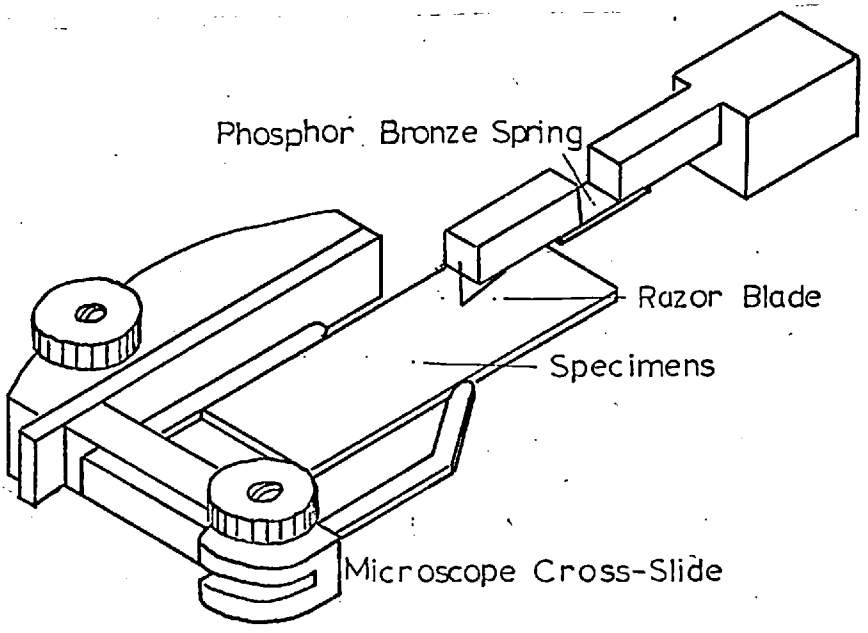

Fig. 18 Device for Trimming Specimens

The razor blade was rigidly mounted and allowed to press down on the specimens with appropriate pressure applied through a phosphor-bronze spring. The trimming geometry was controlled by manipulation of cross slides from an optical microscope.

3.11 Specimen Mounting

Fig. 19 indicates how the specimens were mounted before insertion into the cryostat. Potential leads were 42 gauge copper wire and current leads 28 gauge. Leads were attached to the specimens with indium solder applied with a conventional small bit soldering iron but operated at reduced voltage to prevent film damage.

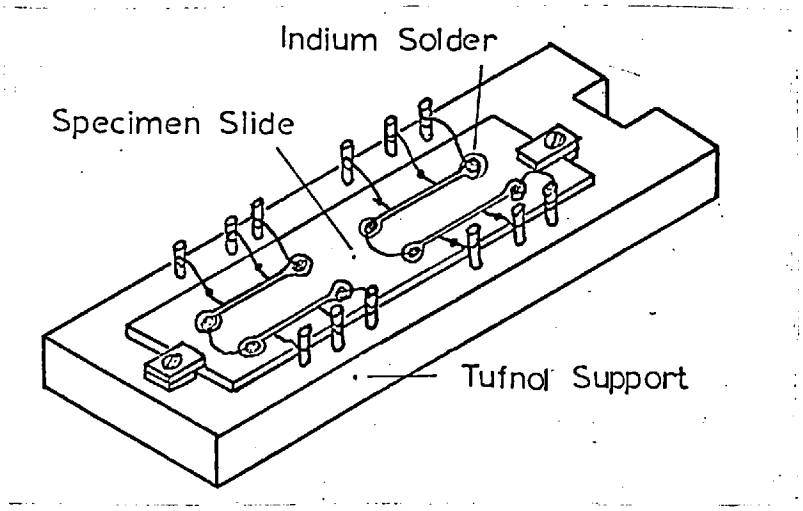

Fig. 19 Specimen Holder

3.12 Growth and Structure of Pb-Bi Films

No literature was available on the growth and structure of Pb-Bi films. It was decided, therefore, to examine two platinum-carbon replicas prepared from the surfaces of $Pb_{0.95}$ $Bi_{0.05}$ evaporated films. The replicas were viewed in transmission through an electron microscope. One replica was made from the surface of a 10.000 Å thick film evaporated according to the conditions outlined in sections 3.6 and 3.7. This specimen was assumed to be typical of those used for superconductivity measurements described in this thesis. The other replica corresponded to the surface of a thin film of the alloy of the order of 100 Å thick.

Plate 2 illustrates the surface of the thinner film which had a connected island structure similar to that of pure lead (54); the presence of grain boundaries and possibly twinning lines may also be seen in this micrograph.

Plate 3 for the thicker film shows grain boundaries which indicate a grain size of at least the thickness of the film. Other parts of this film surface were observed under the electron microscope and large areas found where no boundaries could be seen, inferring a continuous crystal lattice. An important

conclusion to be drawn from the micrograph is that the grain boundaries were separated by distances large compared with the superconducting coherence length and penetration depth. Since the relative orientation of the platinum-carbon rods and substrate were known it was possible to deduce the degree of flatness of the film surface from the lengths of shadows cast by prominences on the surface.

$$\text{Height of prominence} = \frac{\text{length of shadow}}{2.6}$$

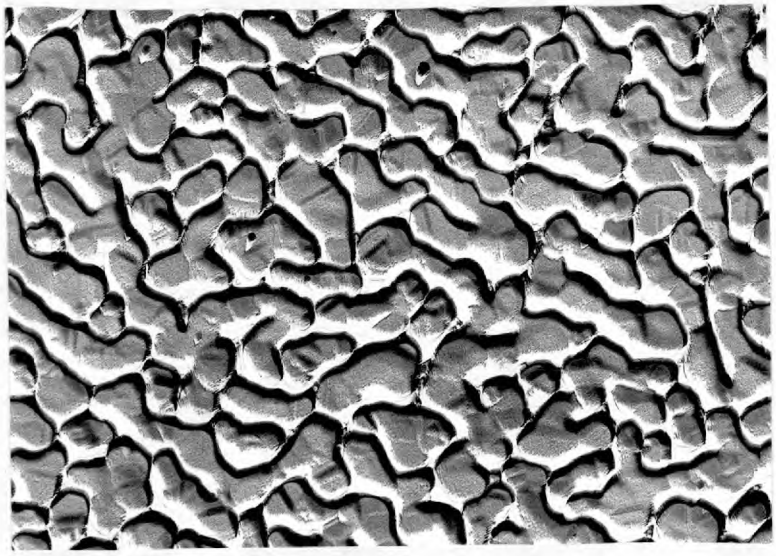

Plate 2. Surface of Thin Pb-Bi Film

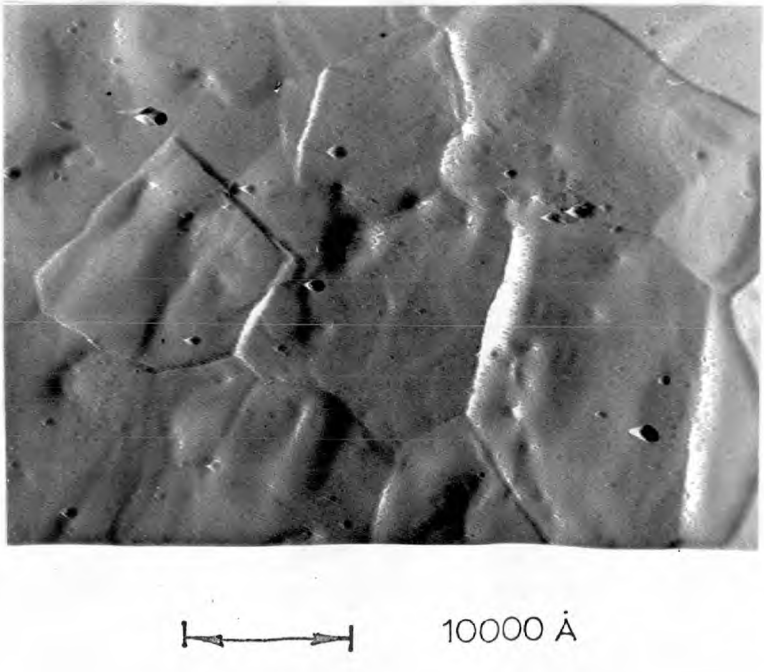

Plate 3. Surface of Thick Pb-Bi Film

CHAPTER IV

CRYOGENICS AND DESCRIPTION OF APPARATUS

4.1 Storage and Transfer of Liquid Helium

Low temperature measurements were made with specimens immersed in liquid helium obtained from Oxford Cryogenics Limited. The helium was delivered in double walled vessels of about 16 litres capacity. Losses during storage amounted to between 0.2 and 0.4 litres per day. For economical reasons gaseous helium was collected in polythene bags and later compressed into metal cylinders for return to the manufacturer. The procedure of transfer of liquid helium using a vacuum jacketed syphon was standard and described in detail by White (55).

4.2 Cryostat and Auxiliaries

The schematic diagram (Fig. 20) shows the layout of the cryostat and auxiliary equipment; plate 4 also illustrates this part of the experimental set up. The cryostat consisted of two dewars with the silvering incomplete along diametrically opposite vertical strips about a centimetre wide. Illumination of the helium through one strip enabled the level to be

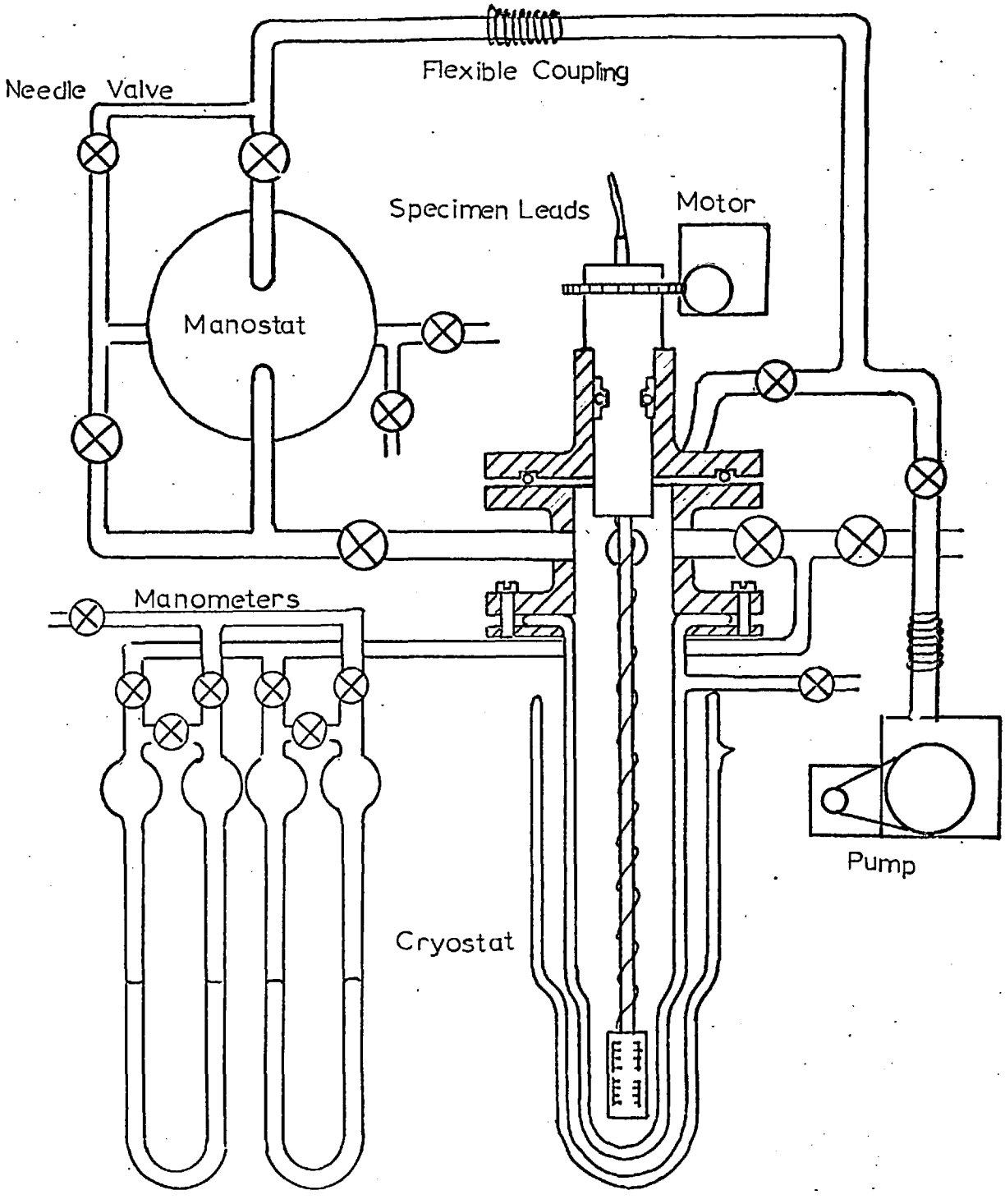

Fig. 20 Cryostat & Auxiliaries

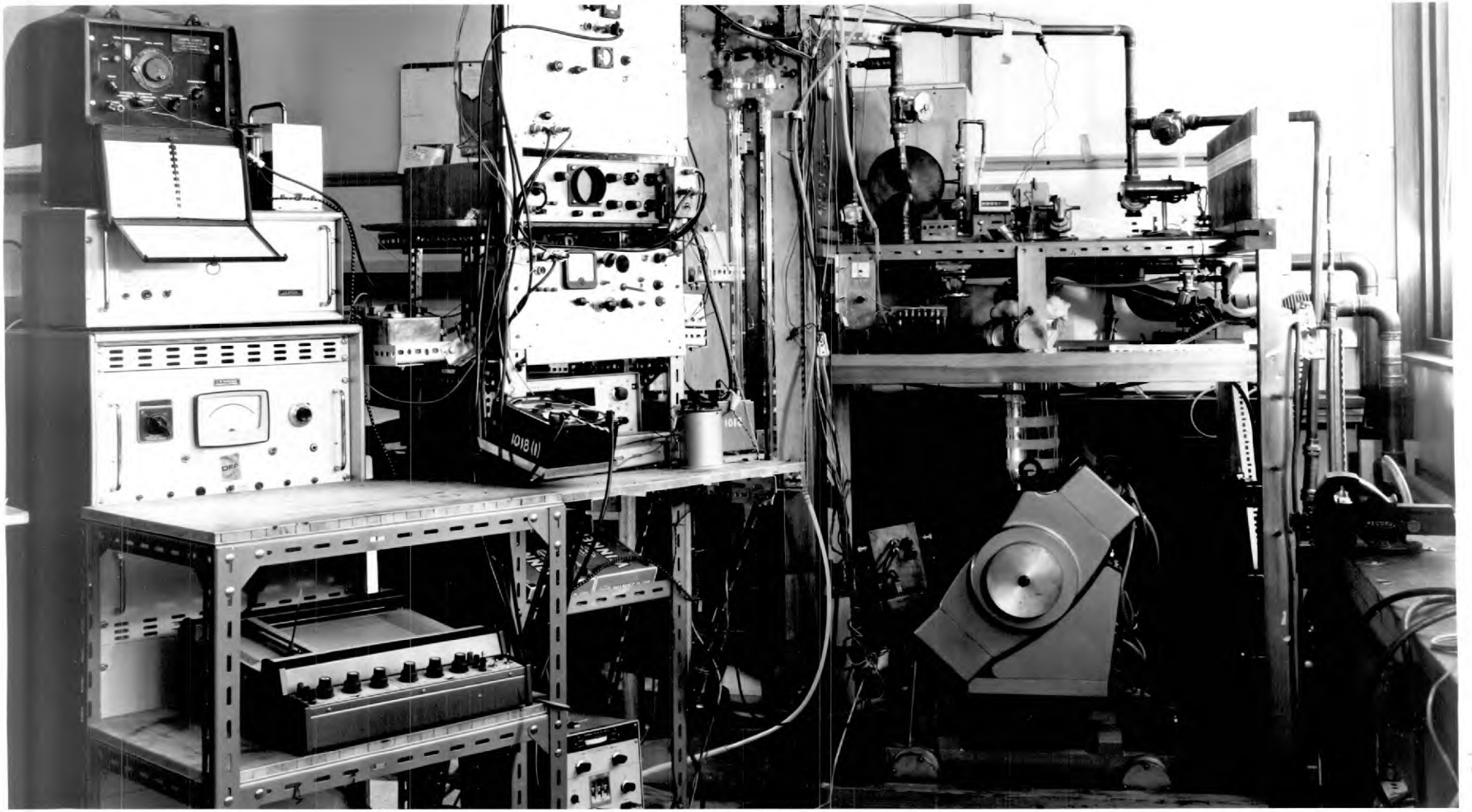

Plate 4. Apparatus

observed through the other. The internal diameter of the tail of the inner dewar was 5.7 cms and its length 18.0 cms.

The specimen holder was connected to a nickel tube mounted on a brass rod. Specimen wires were passed through an insulated "lead-through" housed in the internal bore of the brass rod: a little varnish was necessary to render a leak-free fit of the specimen leads. Joints in the brass metal-work at the top of the dewars were rendered vacuum tight by incorporating standard "O"-ring seals.

It was possible to rotate the specimens about a vertical axis with an electric motor whose speed and sense of rotation could be varied. The orientation was recorded directly from a scale attached to the motor. However, because of backlash in the gearing mechanism, accuracy was limited to $\pm$ 1 degree and a more precise method of angle measurement was employed. A mirror attached to the axis of the specimen support reflected light from a focussed galvanometer lamp that could be made to traverse a scale. In this way the angular orientation of the specimens was set with a precision of better than $\pm$ 0.1 degrees.

Precooling of the specimens was achieved by first filling the inner dewar with exchange helium gas and then flushing out the interspace with dry nitrogen. The interspace was evacuated

to a pressure of 0.05 Torr and the outer dewar filled with liquid nitrogen. The inner dewar reached liquid nitrogen temperatures after about one hour when liquid helium was transferred to the system. Temperatures in the inner dewar were roughly estimated by observing the change in resistance of a carbon resistor attached to the specimen holder.

4.3 Temperature Measurements

Although most measurements were made at atmospheric pressure, temperature control was possible using a manostat of a simple rubber diaphragm type. A 158 litres/min. single stage rotary pump was used to reduce the vapour pressure of the helium. The pressure was recorded by a mercury manometer and translated into temperature using the 1958 He^4 - scale (56). Above the λ point the hydrostatic pressure of the liquid helium at the location of the specimens was added to the manometer reading. This amounted to a maximum correction of 2.8 mms of Hg at the commencement of a run when the helium level was some 30 cms above the specimens. The density of liquid helium was taken as 0.13 gms/cc. Since the 1958 He^4 - scale of temperatures corresponded to mercury at $0^{\circ}C$ it was necessary to allow for the change in density of mercury due to thermal expansion.

The correction factor was negative with a magnitude 3.6×10^{-3} at $20^{\circ}C$. The coefficient of cubical expansion of mercury was taken as $1.82 \times 10^{-4}\ ^{\circ}C^{-1}$. At atmospheric pressure this correction was equivalent to 2.7 mms of Hg. Thus at the commencement of a helium run the total correction was small compared with the probable error in reading the manometer scale. The ability to read the scale to within $\pm$ 0.2 mms was assisted by illumination of the mercury menisci with miniature lamps attached to the scale cursor. Parallax errors were reduced with the aid of a mirror fixed behind the manometer columns. At the completion of a run when the hydrostatic pressure of the helium was small the correction for a nominal temperature of $4.2^{\circ}K$ was less than 4 millidegrees. Other sources of error in temperature measurement have been studied by Wipf (57) who considers the deviation of the acceleration due to gravity from the standard value; the thermal expansion of scales; differences in the shape of the two mercury menisci. He concludes that these errors are small compared with the accuracy of reading the manometer scale.

The dissipation of power in the specimens can also lead to an increase in temperature. The equilibrium temperature

T and power dissipation I^2R can be expressed in the form (58) $I^2R = FA(T - T_o)$ where A is the area of specimen exposed to the helium bath at a temperature T_o and F 200 mW/cm^2/degree K. From this formula an increase of 1 millidegree would be expected from a power dissipation of 10μW in a film of typical surface area 0.05 sq. cm. Critical currents were measured at a power level below this figure and so no allowance was made for the effect of Joule heating on temperature for such measurements.

4.4 Applied Magnetic Fields

Near to H_{c_3} the surface critical current was strongly dependent on the applied magnetic field, H_o. This necessitated an accuracy of field measurement to within 0.1% in order to compare critical currents of different specimens in the vicinity of H_{c_3}. The magnetic fields were typically of the order of a few kOe so that the Earth's contribution of about 0.2 Oe was negligible. The field source was a 7 inch electromagnet (Newport) fitted with shims to improve field homogeneity. The current for field coils was supplied from a Wareham Stabilised Power Unit and Hum Suppressor (type G198/C119).

Magnetic fields were measured with a Hall probe calibrated and tested for linearity with a proton resonance circuit. Preliminary measurements were made on the Hall probe to check its sensitivity to variations in temperature by passing warm water through a copper jacket surrounding the probe crystal. A copper-constantan thermocouple was used to measure temperature as a function of the probe output for constant applied field. The temperature stability was 1.5% of H_o per degree centigrade, sufficiently high to warrant a check on the expected variations in temperature of the probe during the course of an experiment. To determine this variation a thermocouple was again attached to the Hall probe and the thermoelectric voltage measured with a Keighly micromillivoltmeter, the amplified output of which was used to drive a Honeywell Recorder. Measurements over periods of several hours revealed that drifts in temperature could be as much as 0.3 degrees centigrade per hour. Provided the calibration of the applied field was checked every quarter of an hour during an experiment, errors in the field due to temperature variations did not amount to more than the required 0.1%. The Hall probe was used to check the homogeneity of the magnetic field in the volume occupied by the specimens. No variations in field were detected in this volume - homogeneity

was further verified from the shape of the proton resonance trace which exhibited "ringing", indicative of a uniform field.

4.5 Proton Resonance Probe

The Hall probe was calibrated with a circuit for magnetic resonance detection based on a design by Faulkner and Holman (59). A schematic representation of the circuit is illustrated in Fig. 21.

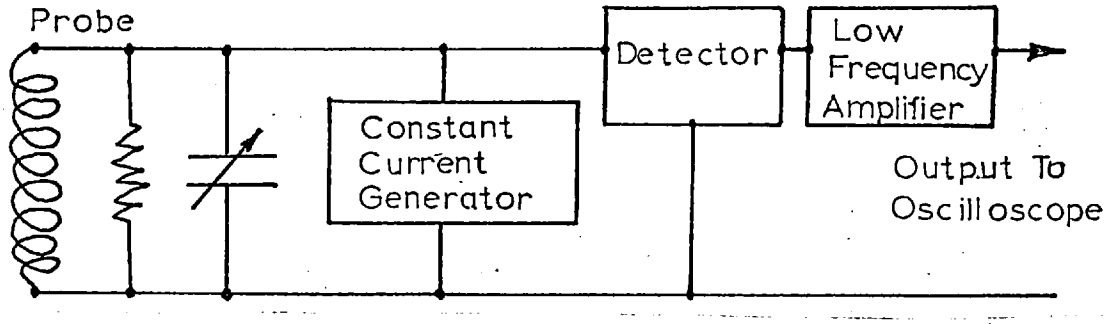

Fig. 21 Proton Resonance Circuit

The current generator was a two transistor limited oscillator. The oscillator frequency was measured by injecting a r.f. signal from a frequency meter and observing beats on the oscilloscope screen. The collector current in the second transistor corresponded to a square wave of constant amplitude and unity mark/space ratio. This r.f. current flowed through a coil surrounding

a capsule containing 1/20th normal ferric nitrate solution. The voltage developed across this coil depended on the quality factor, Q, and thus on the nuclear magnetic resonance. Changes in the voltage across the coil were registered by the detector, amplified and applied to the Y-plates of a cathode-ray oscilloscope.

An important part of the circuit was the design of the probe head. This was made from a Radiospares 7 mm diameter coil former filled with the ferric nitrate solution and sealed off to prevent loss of fluid due to evaporation. The 1 centimetre long coil was wound with 38 gauge enamelled copper wire - each turn separated by the wire diameter to optimize the Q factor. The coil was mounted rigidly to a piece of perspex to which field sweep coils were also mounted. These took the form of a Helmholtz pair, each 2.5 cm in diameter and wound with 30 turns of 28 guage enamelled copper wire. The probe and sweep coils are illustrated in Fig. 22 together with the associated electrical circuitry. The magnitude of the sweep field could be changed by altering the resistance in series with the coils. With the 50 ohm resistance in series the sweep field had a peak to peak magnitude of 5(0e). At each calibration point the applied field from the magnet was adjusted until a

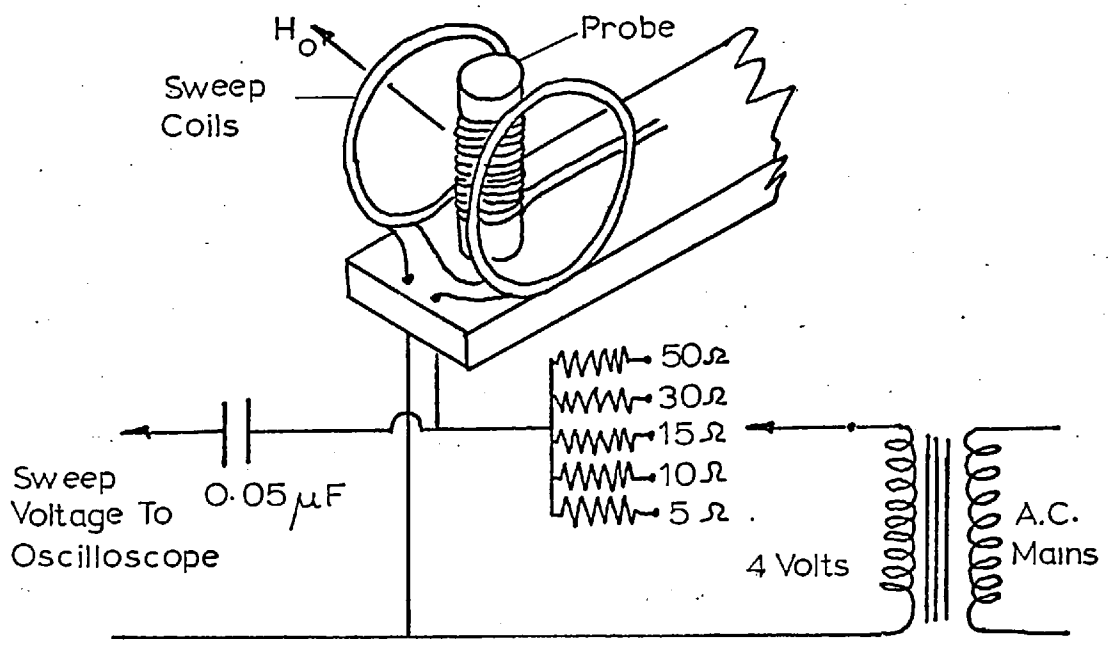

Fig. 22 Proton Resonance Probe

resonance signal was located at the centre of the oscilloscope trace. This could be achieved to within an estimated error of about 1 Oe. The proton resonance probe served to check the linearity of the Hall probe over a field range from 960 Oe to 3.7k Oe. Over this range the Hall probe output was linear with oscillator frequency to within the required limits of accuracy.

4.6 Measurement of Critical Currents

Critical currents corresponding to the appearance of $1\,\mu V$ at the specimen potential terminals were measured using

a self-balancing current regulator shown in Fig. 23. All leads and terminations to the input circuit were of copper to minimize thermal gradients. The potential leads were connected via a low thermal switch to the input terminals of a Tinsley Photocell-Galvanometer Amplifier type 5214 which satisfied the stringent requirements of high sensitivity (gain ~ 300) and low thermal drift necessitated by the low threshold voltages involved. The d.c. biasing arrangement had two functions; firstly to balance thermal e.m.f.'s in the circuit and secondly to set the reference voltage for the error controlled servo-loop. When the reference was set at 1 μV the equilibrium state of the system corresponded to the condition that the voltage across the specimen potential leads was 1 μV and the input to the operational amplifier was zero. When the specimen p.d. was different from 1 μV the resulting error voltage was integrated by the operational amplifier employing capacitive feedback. The output from this amplifier actuated the control unit supplying current to the specimens. The reference voltage was set by replacing the specimens with a 0.005 Ω standard resistance and adjusting the d.c. bias until the equilibrium state of the mechanism was achieved with a current of 200 μA. The d.c.:d.c. converter served

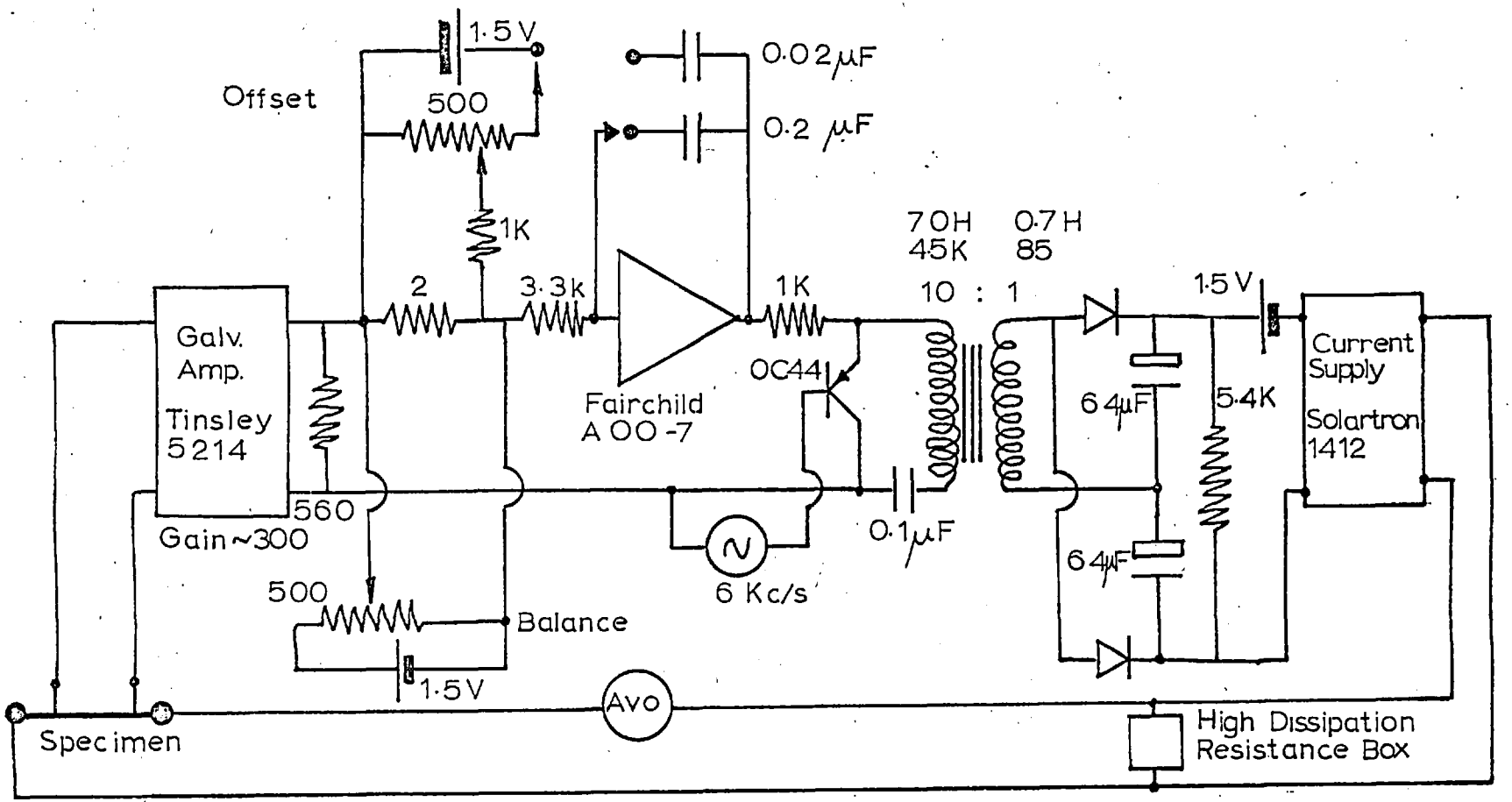

Fig. 23 Current Regulator

to introduce a break in the earth line, to obviate earthing both a current and a voltage lead from the specimen. The converter functioned by chopping the d.c. output from the integrator so that the transformer could convey the signal to the rectifier where the d.c. voltage was restored and fed to the control unit.

4.7 Measurement of Voltage-Current Characteristics

Experiments were conducted where a transport current was applied to the specimens and the voltage developed across the potential leads measured. The voltage-current (I-V) characteristics were plotted for different magnitudes and orientations of the applied field.

Current was supplied to the specimens using a Solartron Power Supply Unit Type AS 1412.2. It was possible to use the Unit to sweep the current using an external programme which took the form of an integrating linear sweep generator shown in Fig. 24. I-V characteristics were plotted directly using a Bryans Portable XY plotter Model 22000. The X terminals were used to record the current by measuring the p.d. across a 0.2 Ω standard resistance in series with the specimens.

The Y input terminals were connected to the specimen potential leads. The circuit arrangement is illustrated in Fig. 25.

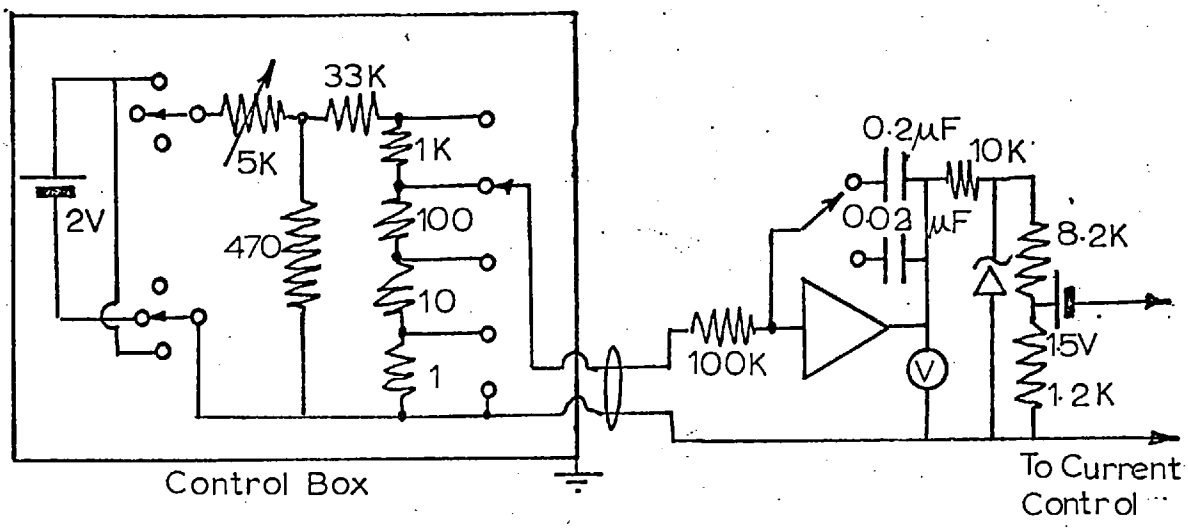

Fig. 24 Integrator Circuit

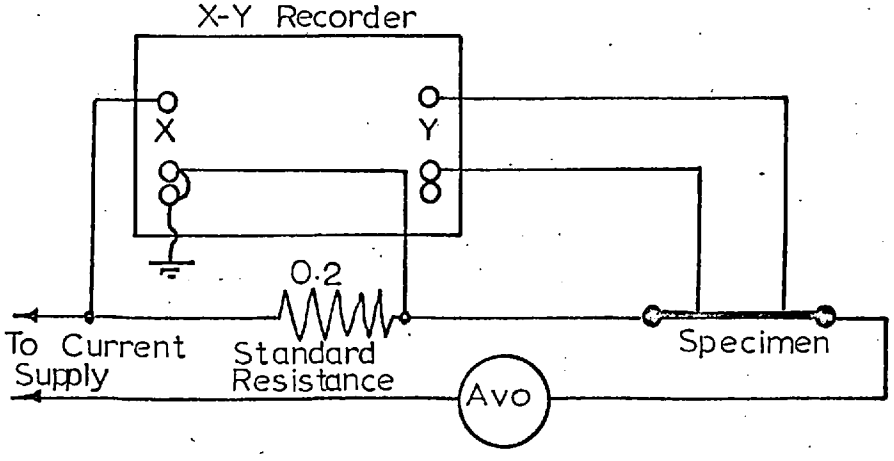

Fig. 25 Plotting of I - V Curves

CHAPTER V

EXPERIMENTAL RESULTS

5.1 Estimates of Residual Resistivity as a Function of Composition

Measurements were made of normal state resistances of Pb-Bi films at room temperature and at liquid helium temperatures. Resistances were measured, using four terminal techniques, with a Comark resistance meter (type: 220) and by plotting normal state I-V characteristics as described in section 4.7. The superconducting phase at liquid helium temperatures was quenched by applying a perpendicular magnetic field of 6.1 k.Oe. Resistance changes in the normal state for field variations between Hc_3 and 6.1 k.Oe and also for temperature variations between 1.8°K and 4.2°K amounted to less than 2%. Any systematic errors arising from the effects of magnetoresistance and lattice vibrations were thus neglected and considered smaller than scatter in experimental results. The resistivity of the specimens was determined from knowledge of specimen geometry or deduced from the resistance ratio, R_r, defined by:

$$R_r = \frac{\text{Resistance of films at room temp.}}{\text{Resistance at } 4.2^{\circ}K} \qquad 5.2.1$$

From Matthiessen's rule, the resistivity of the alloys at room temperature, ρ_{RT}, can be represented by the sum:

$$\rho_{RT} = \rho_{Pb} + \rho_{4.2} \qquad 5.2.2$$

where ρ_{Pb} is the phonon contribution at room temperature which was taken to be that of pure lead, $20.6 \mu\Omega$.cm (60). From equations 5.2.1 and 5.2.2:

$$\rho_{4.2} = \frac{20.6}{R_r - 1} \mu\Omega \text{.cm}$$

The residual resistivity has been plotted in Fig. 26 as a function of composition. Results are compared with earlier measurements of Livingston (61) and Gamari (62). The solid line in the graph corresponds to a fit of the present experimental data to Nordheim's rule:

$$\rho_{4.2} = 0.83\, x\left(1 - \frac{x}{100}\right) \mu\Omega\text{.cm}$$

where x is the composition of the alloy in atomic % bismuth. In applying Nordheim's formula no allowance was made for changes in lattice parameter or for the increase in the number of valency electrons per atom with increased bismuth composition.

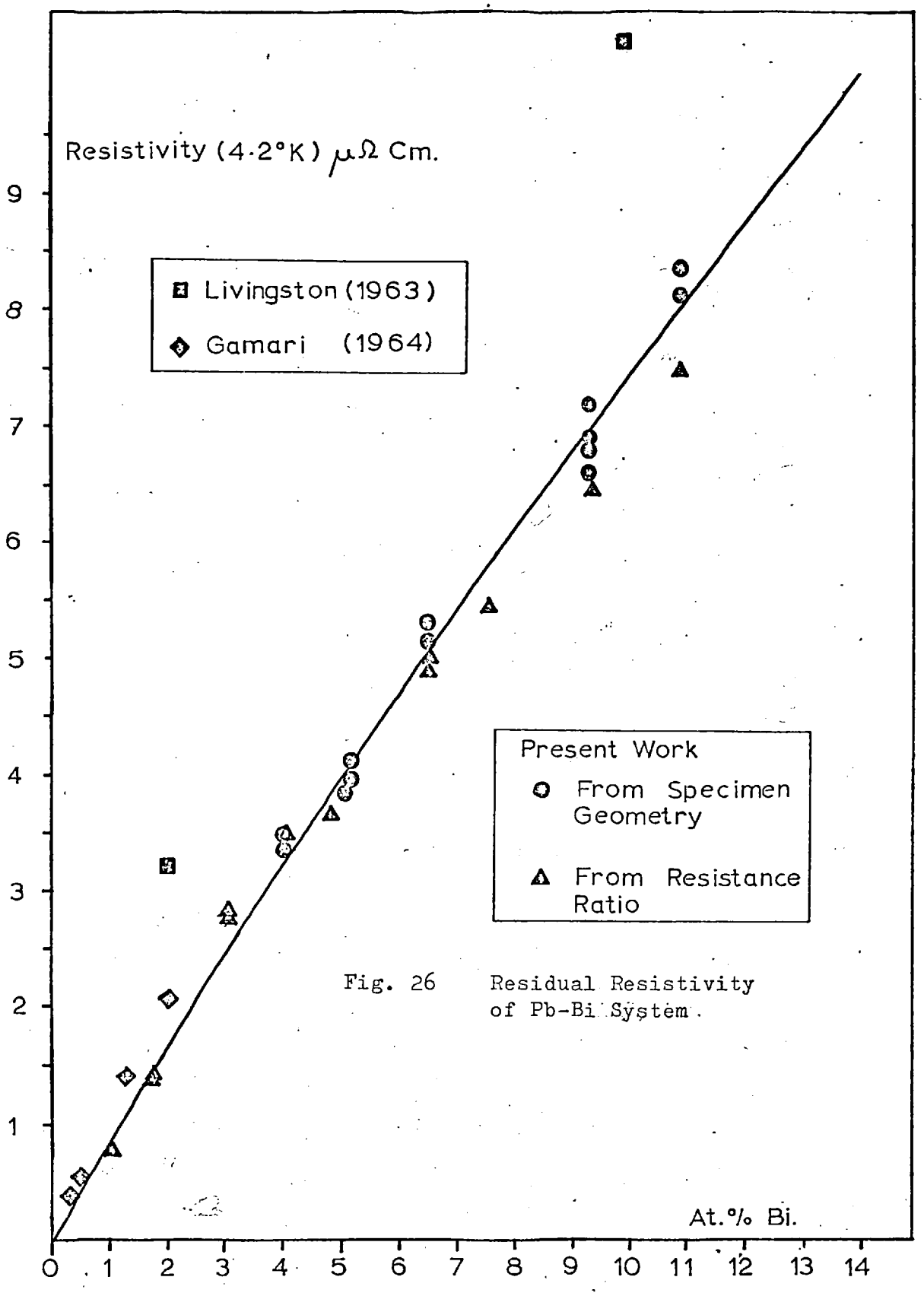

Fig. 26 Residual Resistivity of Pb-Bi System.

5.2 Estimates of Critical Fields and some Qualitative Features of Critical Current Measurements

Critical current characteristics were expressed by plotting log I_c as a function of the applied field Ho. Two orientations of the field with respect to the specimens were of particular interest:

(i) Ho perpendicular to both the transport current and film surface. From the nomenclature adopted in Fig. 9 this corresponds to the case of $\Theta = 90^o$ and $\phi = 90^o$

(ii) Ho parallel to the film surface and perpendicular to the transport current i.e. $\Theta = 90^o$, $\phi = 0^o$.

The fields corresponding to the transition to the normal state for configurations (i) and (ii), respectively $H_{\perp}$ and H_{11}, have been interpreted by Burger and St James (63) from solutions of generalised G-L equations. In the dirty limit and for films thick compared with their coherence lengths:

$$H_{\perp} = H_{c_2}$$

and $$H_{11} = H_{c_3}$$

Typical critical current characteristics are shown in Figs 27-28 for specimens 41(13/14) and 38(15/16). Specimen details are tabulated in the appendix. $H_{c_2}(T)$ was identified

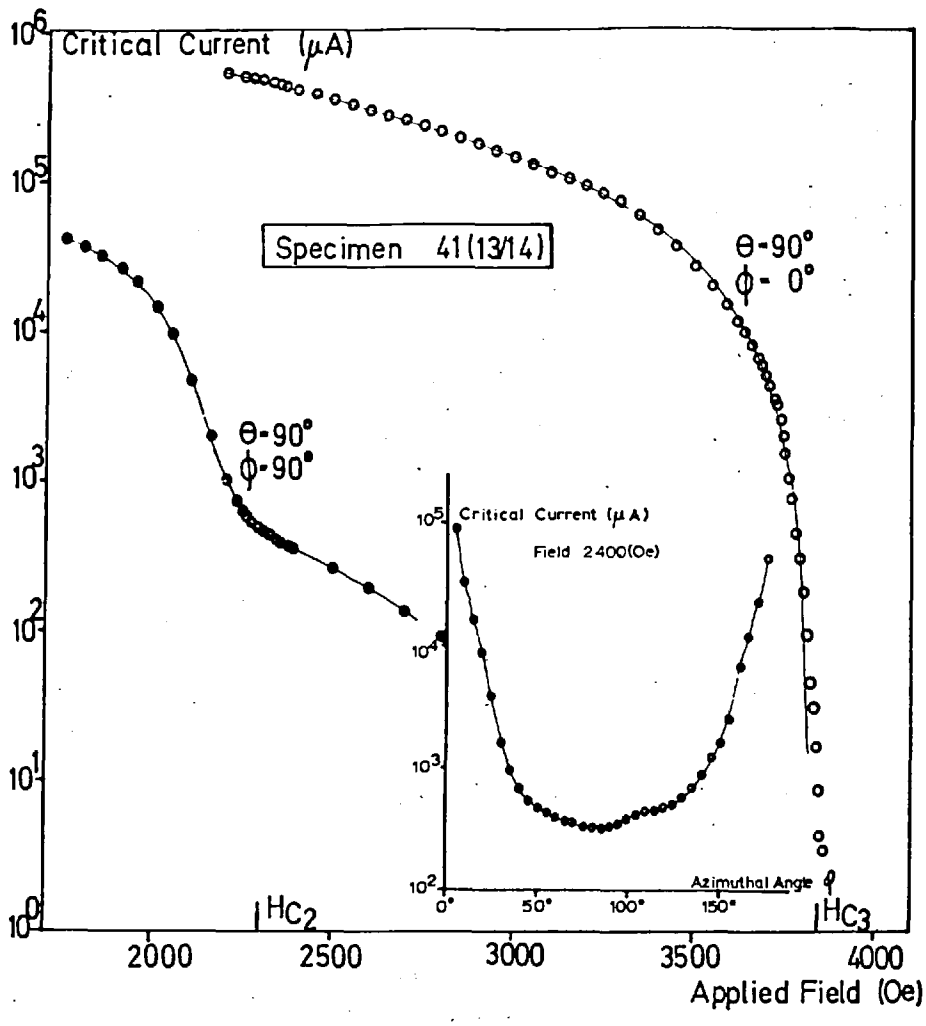

Fig. 27 Critical Current Curves for Specimen containing 6.5 At.% Bi

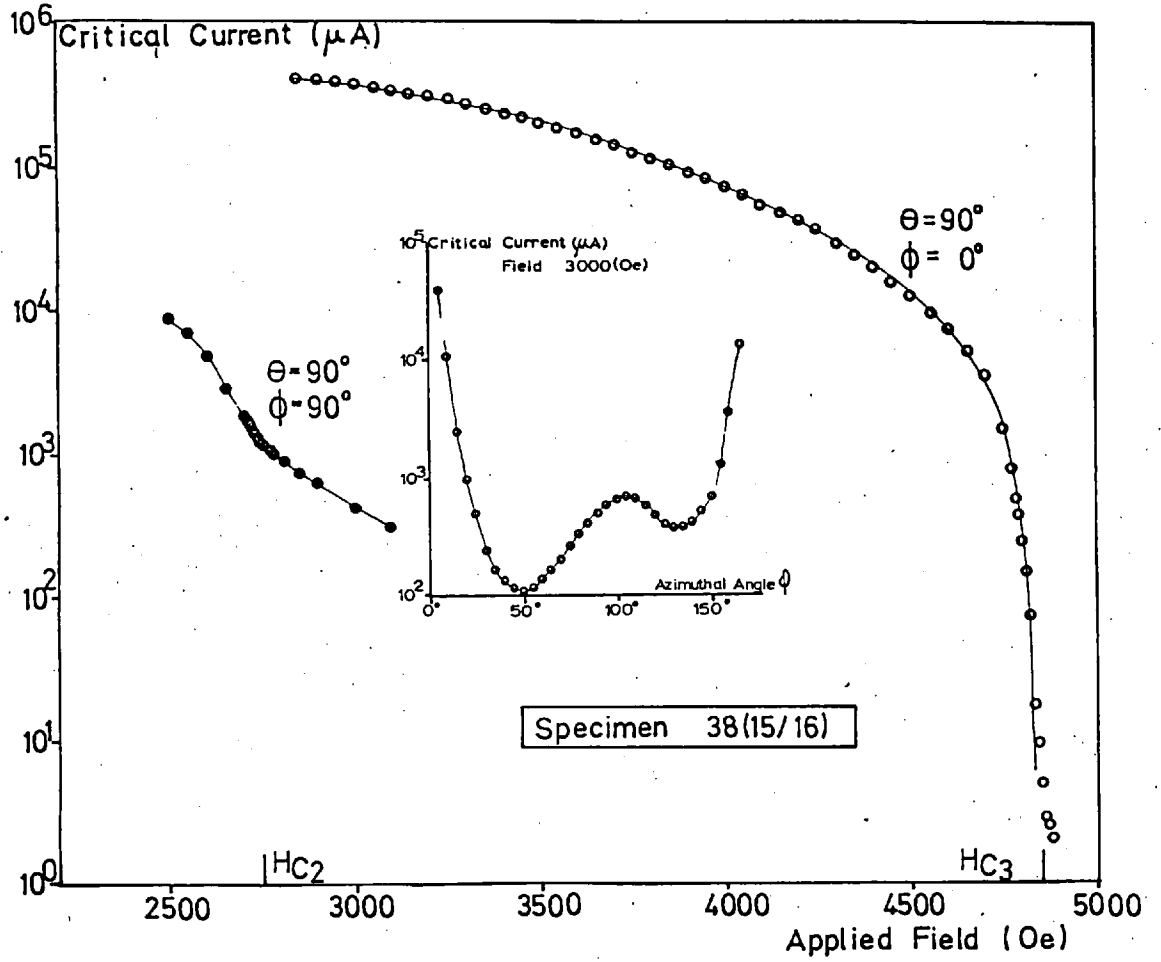

Fig. 28 Critical Current Curves for Specimen containing 9.3 at.% Bi

with the value of Ho which corresponded to a discontinuity in the gradient of the critical current curve for $\Theta = 90^{\circ}$, $\varphi = 90^{\circ}$. The observed values of $Hc_2(T)$ were masked by the presence of a tail in the critical current curve. The existence of superconductivity above H_{c_2} was believed to be due to the presence of surface superconductivity at the edges of the specimen. In order to check that this was the case two tests were made. Firstly the specimens were rotated so that an attempt could be made to align the edges parallel to the applied field and so enhance the effect of surface superconductivity. Secondly, surface superconductivity was reduced at the edges by enveloping the film in an evaporated layer of copper. The results of the first test indicated that in the majority of cases a plot of log I_c as a function of φ in constant field revealed no significant features apart from a lack of symmetry in the value of the critical current about $\varphi = 90^{\circ}$ (Fig. 27). An exception was specimen 38(15/16) illustrated in Fig. 28 where a secondary peak was distinctly seen. The second test showed that the tail above Hc_2 was considerably reduced when the specimen was coated with a 400 $\mathring{A}$ layer of copper (Fig. 29).

The copper was evaporated at a pressure of 5×10^{-6} Torr without breaking the vacuum between consecutive depositions of copper and alloy layers.

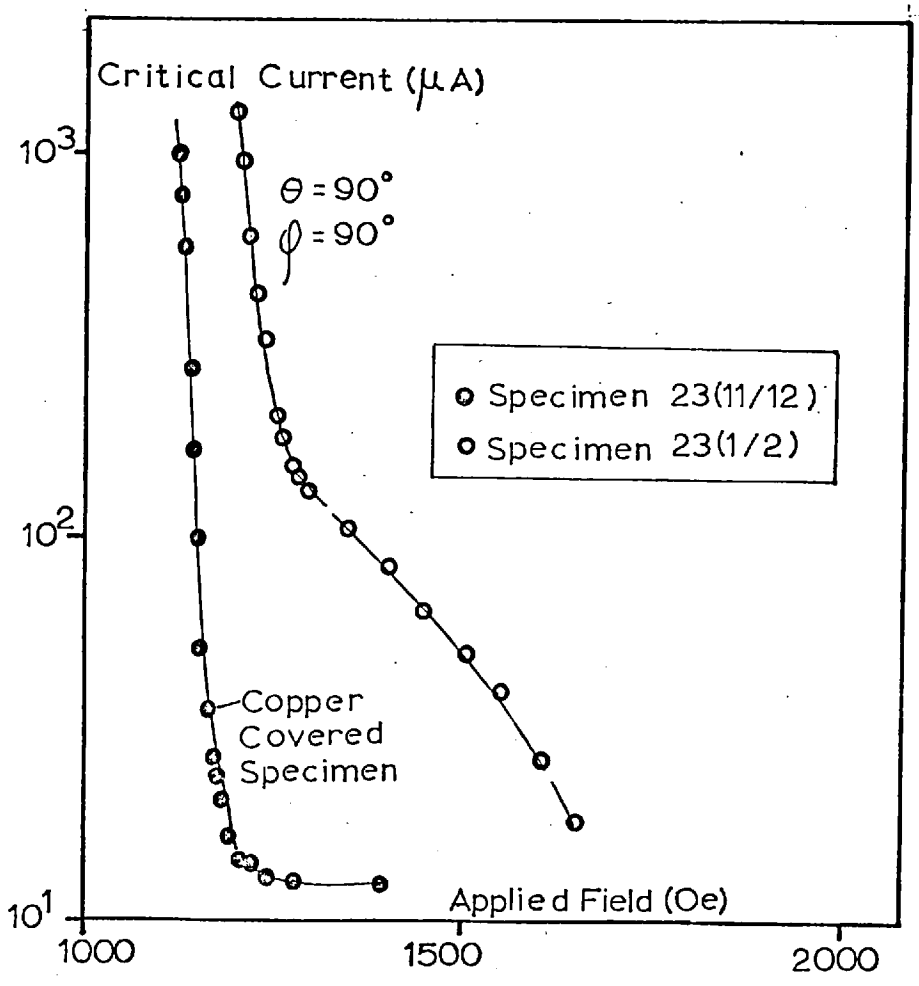

Fig. 29 Influence of Proximity Effects on Critical Current Characteristics

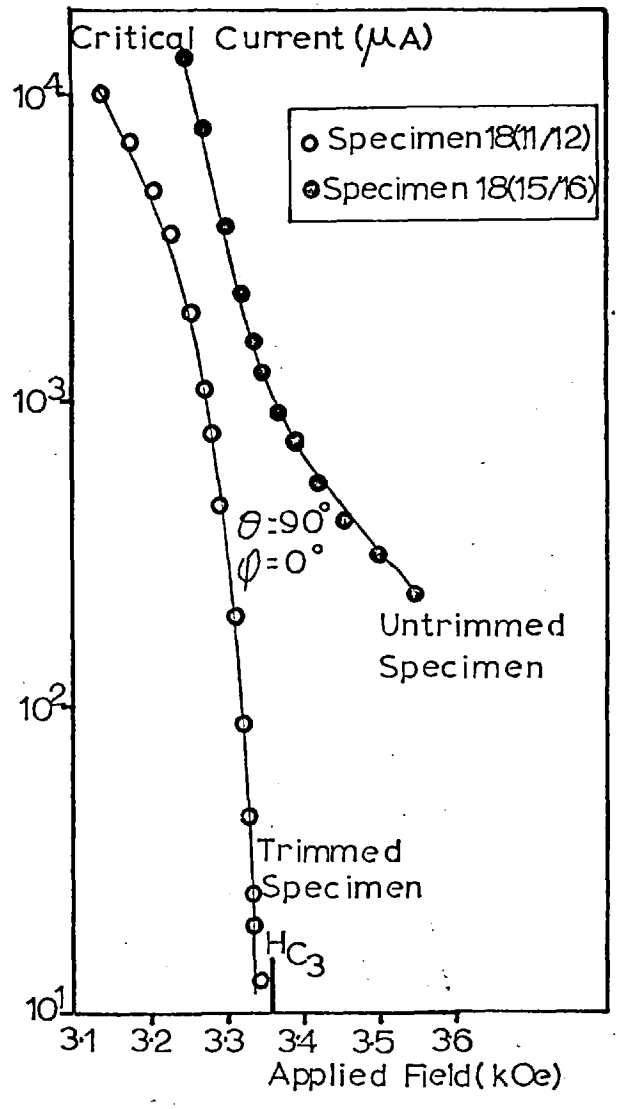

Fig. 30 Effect of Trimming

In order to determine the parallel transition field, H_{11}, it was found convenient to treat the measured critical current, I_c as the sum of contributions from the sheath I_s and the normal bulk I_n:

$$\text{i.e.} \quad I_c = I_s + I_n$$

I_n was taken to be the measured critical current in high fields where only the normal phase was present. The applied field, Ho, was then expressed as a series expansion in log I_s:

$$H_o = a_o + \sum_{n=1}^{10} a_n (\log I_s)^n \qquad 5.2.1$$

where the coefficients were determined by computer and H_{11} estimated by extrapolating the data to find the maximum value yielded by equation 5.2.1. For trimmed films H_{11} was taken to be equal to H_{c_3} but for untrimmed specimens H_{11} was considerably greater than $H_{c_3}(T)$ as Fig. 30 illustrates in page 91.

5.3 H_{c_3} and H_{c_2} as a Function of Composition at 4.2°K

H_{c_2} and H_{c_3} were determined from critical current characteristics over a range of compositions between 1 and 15 at.% Bi at 4.2°K Results are plotted in Figs 31-32 for

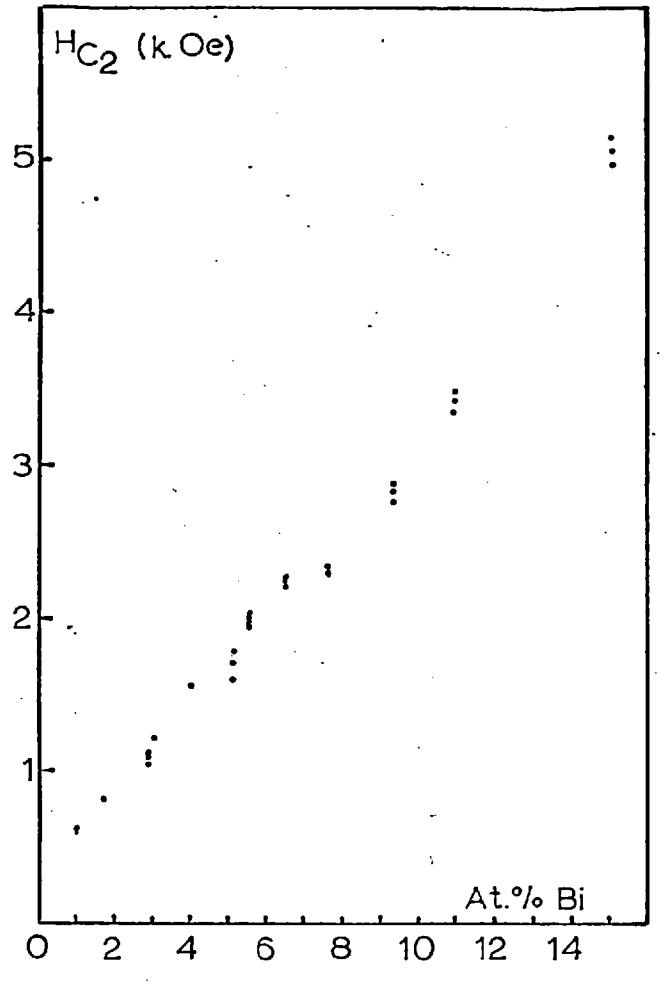

Fig. 31 Variation of H_{c_2} (4.2°K) with Composition

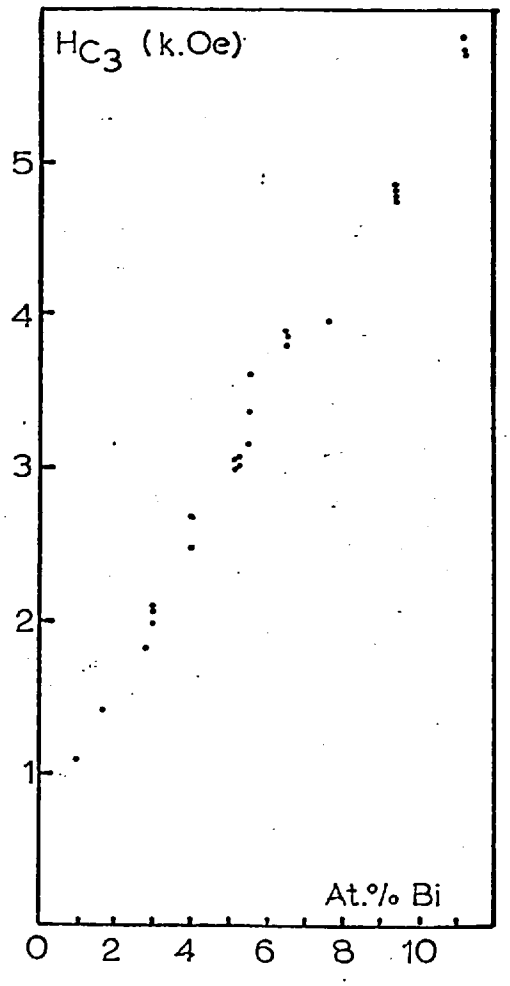

Fig. 32 Variation of H_{c_3} (4.2°K) with composition

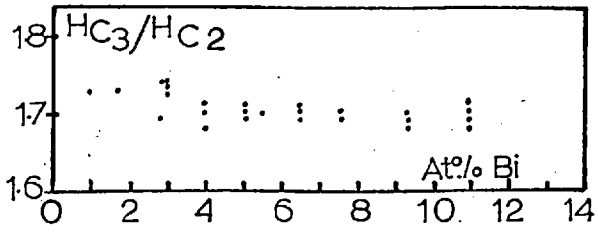

Fig. 33 Variation of H_{c_3} (4.2)/ H_{c_2} (4.2) with composition

specimens which had been trimmed and annealed for one hour at 150°C. The compositions ofthe films were taken to be equal to that of the alloy prior to evaporation. The ratio of the two critical fields are plotted in Fig. 33 for comparison with the theoretical value of 1.695.

5.4 Importance of Specimen Annealing

Early measurements of critical current characteristics were made on unannealed specimens which had been at ambient room temperature for periods between 16 hours and a week prior to the execution of experiments. Estimates of parallel transition fields for the specimens were in general larger than H_{c_3} obtained for specimens of similar average composition but first annealed at 150°C for one hour. With unannealed specimens there was considerable scatter in the observed data which resulted in variations of H_{c_3}/H_{c_2} ranging from 1.7 to 2.1. It was possible to check the existence of composition gradients across specimens by taking advantage of the surface sheath destroying properties of a layer of evaporated copper. When copper was applied between the substrate and an unannealed film containing 5.5 at.% bismuth the ratio H_{c_3}/H_{c_2} was 1.86. However, when copper was applied to the upper surface of a film this ratio was 1.46 after 16 hours at room temperature. After a further 80 hours at room temperature this ratio increased

to 1.56. A specimen evaporated from the same source but annealed for 1 hour at 150°C possessed a ratio $H_{c_3}/H_{c_2} = 1.69$. Subsequent annealing for another hour at this temperature failed to produce any further changes in the value of H_{c_3}/H_{c_2}. From these observations it appears that during the formation of a Pb-Bi film the lead component is deposited preferentially. The observations also emphasize the importance of annealing specimens to ensure homogeneity.

Attempts to raise the annealing temperature beyond 200°C resulted in distortion of the film and lifting from the substrate.

5.5 The Variation of H_{c_2} and H_{c_3} with Temperature

The critical fields H_{c_2} and H_{c_3} were measured over a limited range of temperatures from 1.87°K to 4.21°K for specimen 18(11/12) containing 5.5 at.% bismuth. H_{c_2} for this specimen is plotted as a function of reduced temperature in Fig. 34. $T_c = 7.41$°K was taken from the thesis of Gamari (62). No changes in the ratio of H_{c_3}/H_{c_2} were detected for variations in temperature:

$$H_{c_3}/H_{c_2} = 1.74 \pm 0.2$$

The estimated uncertainty in this result stems largely from the lack of precision in the estimate of H_{c_2} because of the persistence of superconductivity to higher fields.

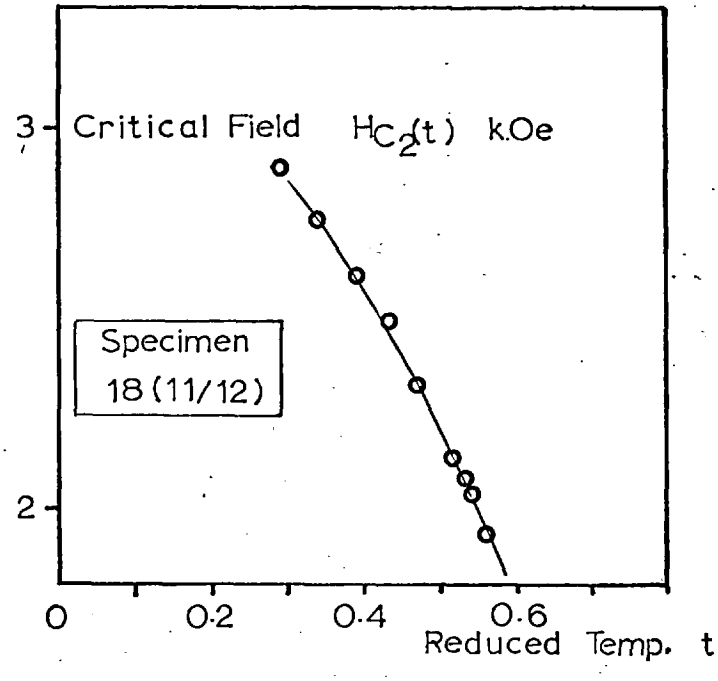

Fig. 34 Variation of H_{c_2} with Reduced Temperature

5.6 Sensitivity of the Shape of the Critical Current Curves to the Voltage Dectection Level

In determining critical current characteristics, the critical current was taken to be the current corresponding to the appearance of $1\mu V$ at the specimen potential leads. The influence of the defining voltage on the shape of parallel field ($\Theta = 90^{\circ}$, $\phi = 0^{\circ}$) critical current curves was investigated for voltage levels in the vicinity of $1\mu V$. Fig. 35 shows I-V and critical current characteristics for specimen 33(11/12).

Near to H_{c_2} the critical current was insensitive to variations in voltage but as Ho approached H_{c_3} the voltage level became increasingly important in deciding the shape of the critical current curve (Fig. 35).

5.7 Critical Current Characteristics for Specimens of Different Compositions

Critical current characteristics were plotted at a temperature of $4.2^{\circ}K$ for specimens of different compositions with surface superconductivity present on both surfaces. Some of these characteristics are represented in Figs 36-39. The effect of variations in bismuth concentration on the critical current density at fields of H_{c_2} and $1.60\ H_{c_2}$ are displayed in Fig. 40.

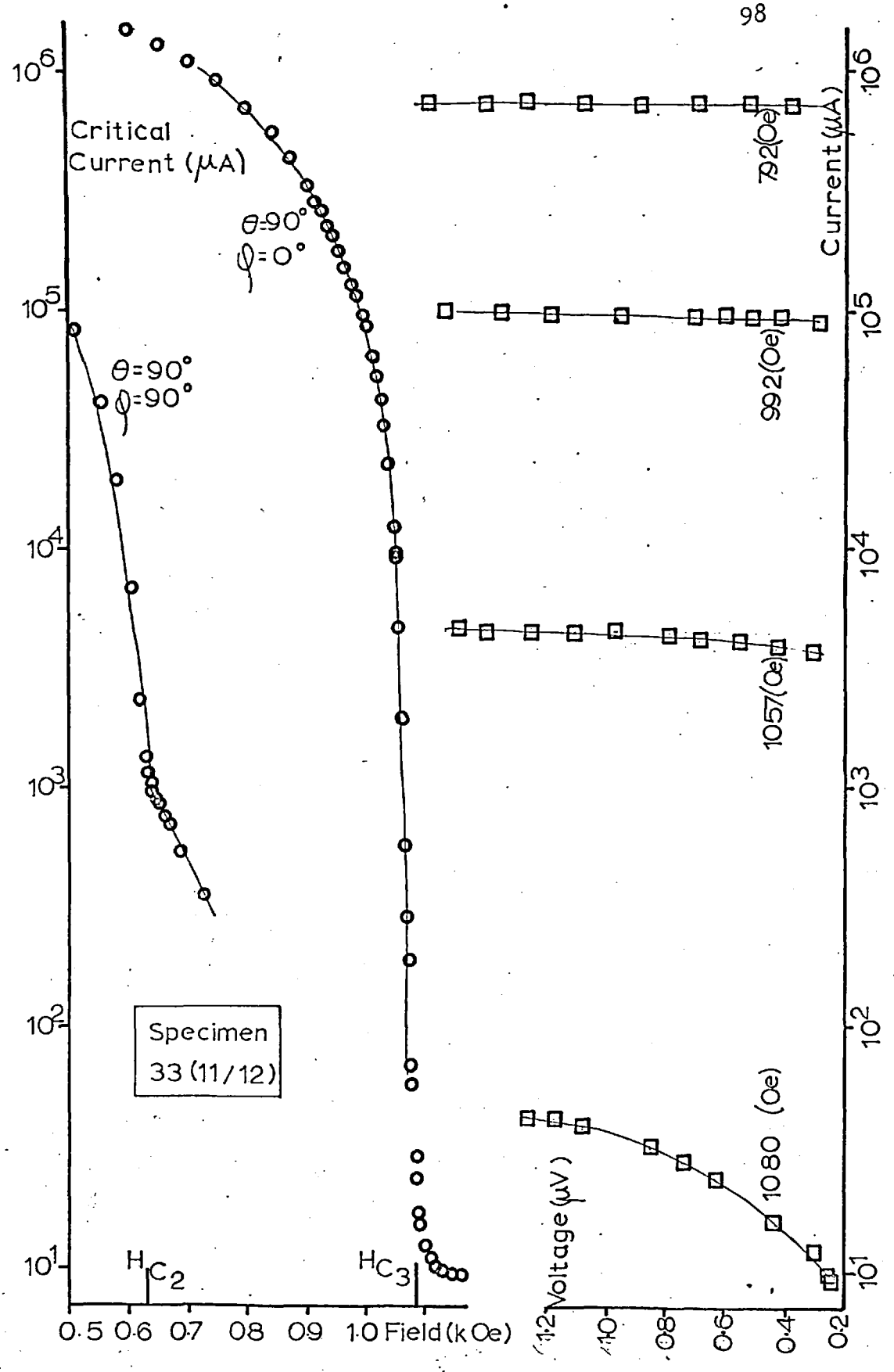

Fig. 35 I-V and Critical Current Characteristics

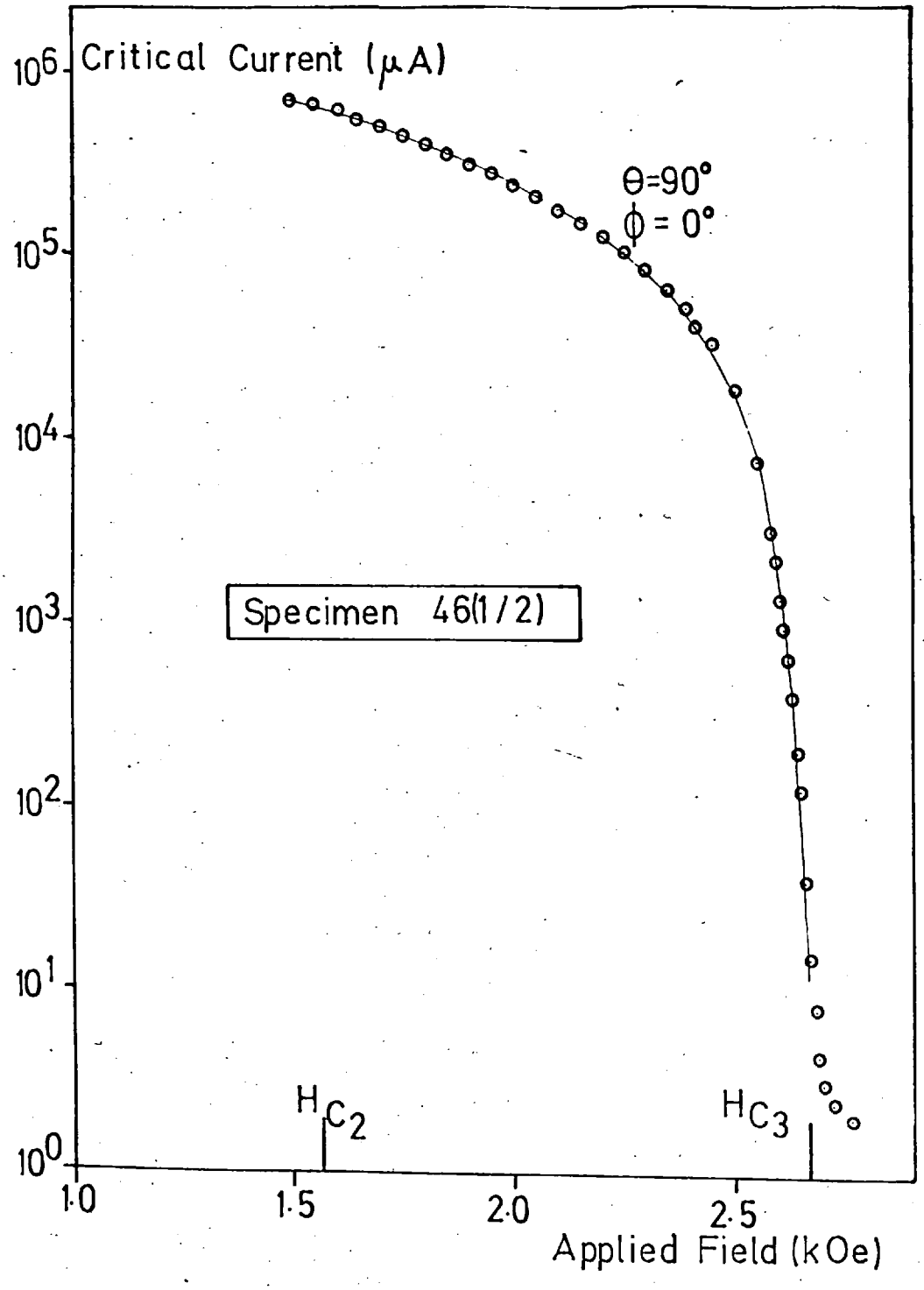

Fig. 36 Critical Currents for Specimen Containing 4.0 At.% Bi

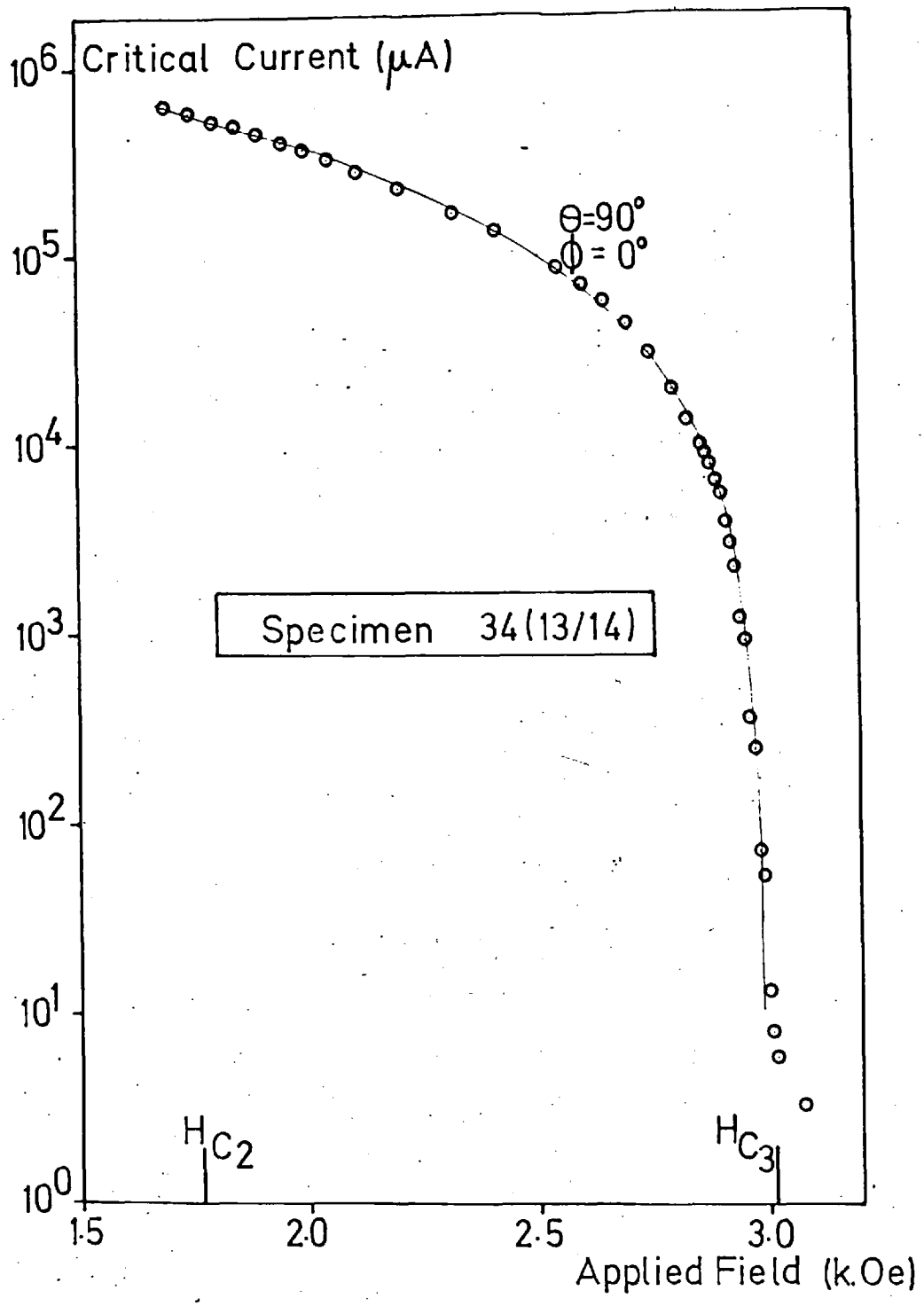

Fig. 37 Critical Currents for Specimen Containing 5.2 At.% Bi

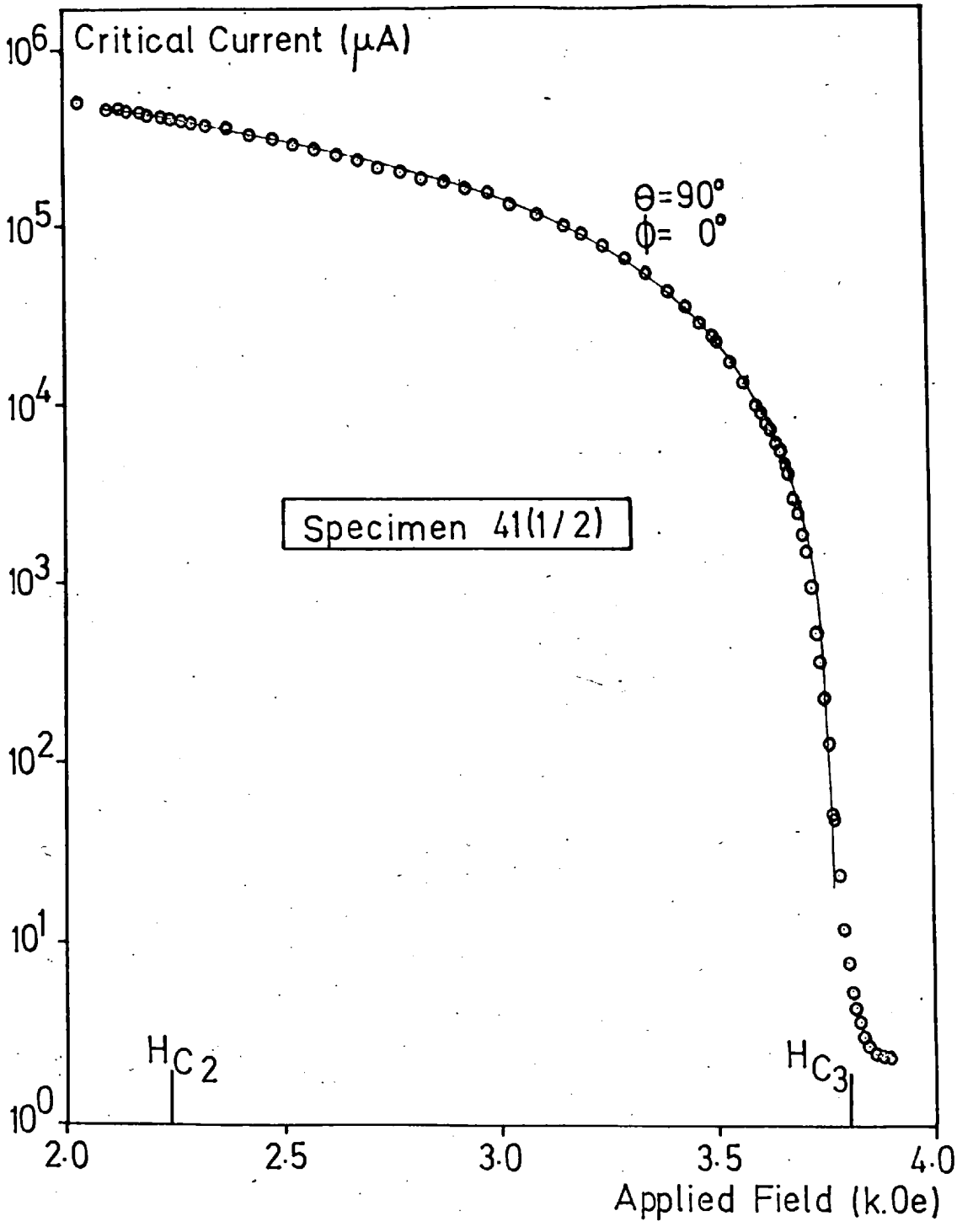

Fig. 38 Critical Currents for Specimen Containing 6.5 At.% Bi

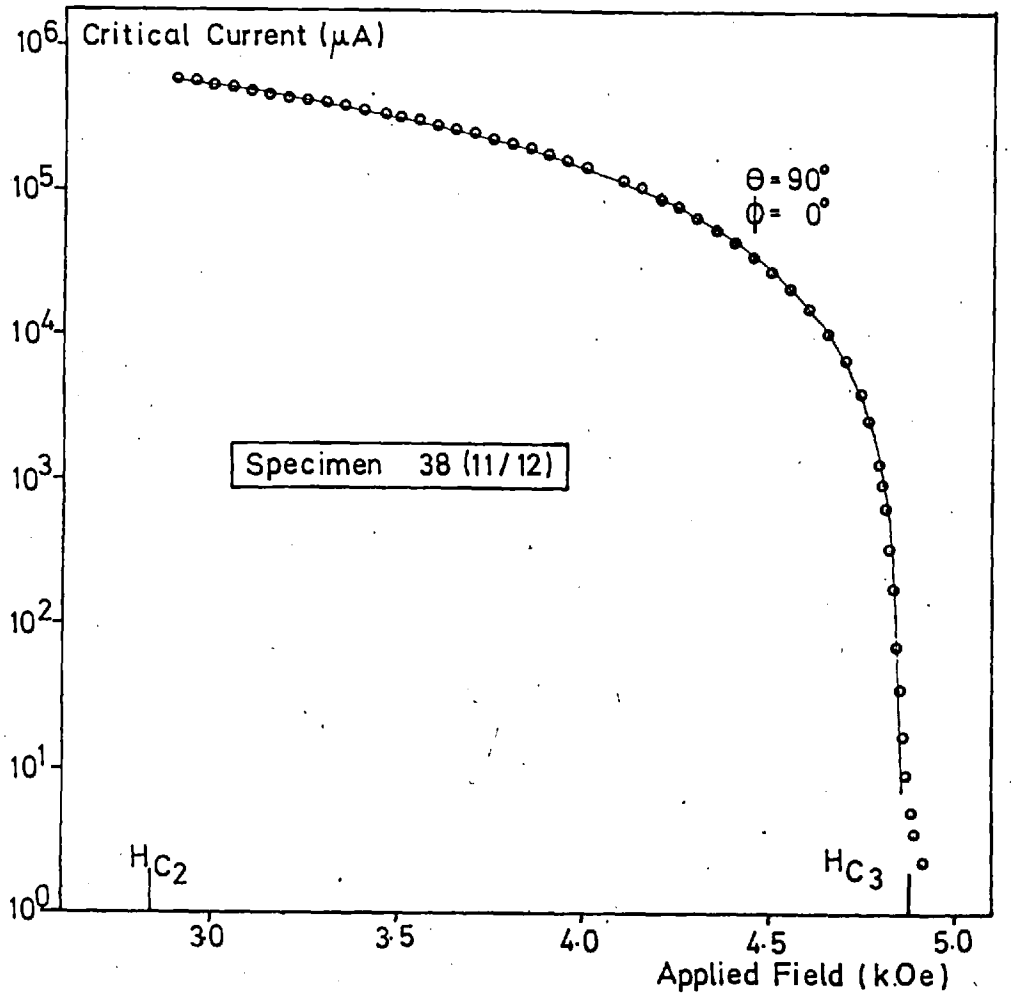

Fig. 39 Critical Current Curve for Specimen Containing 9.3 at.% Bi

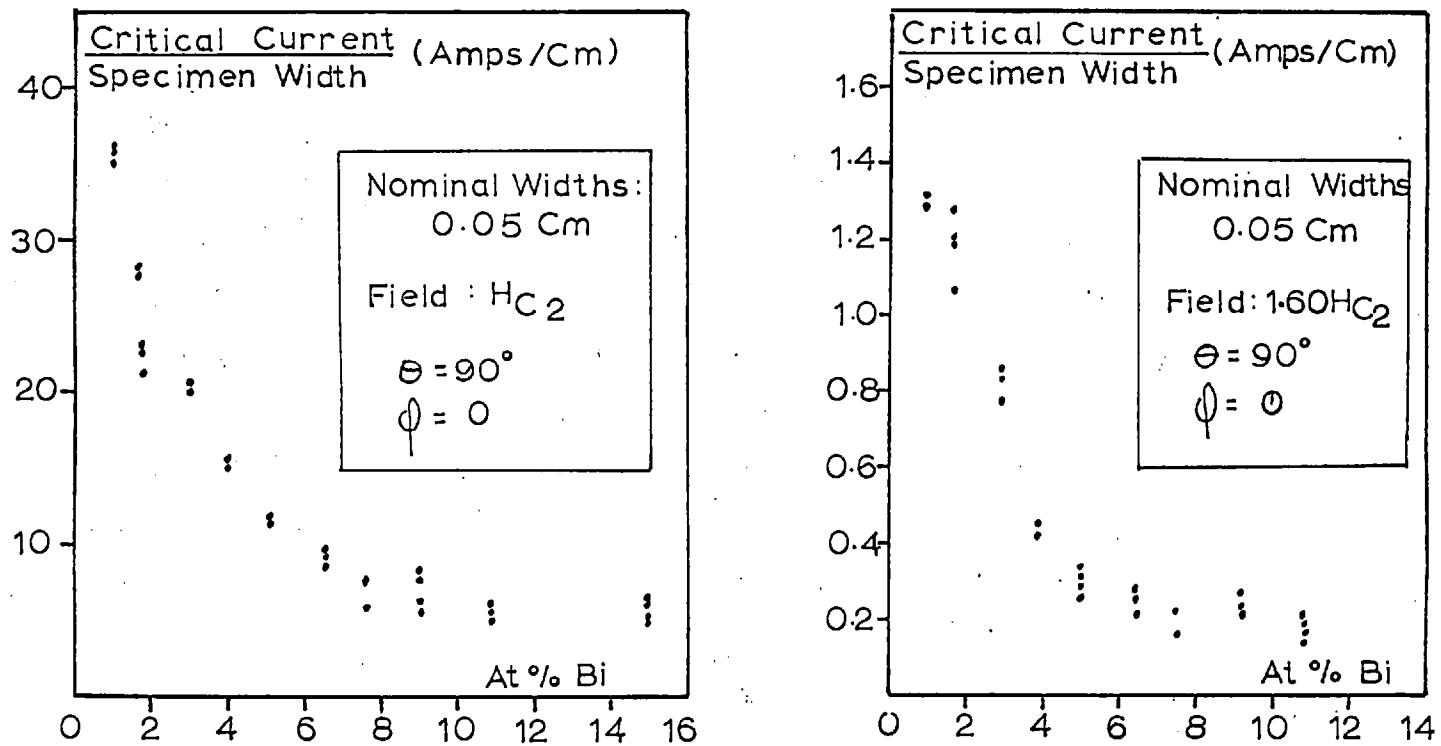

Fig. 40 Variation of Critical Current with Bi Concentration at H_{c_2} and 1.60 H_{c_2}

5.8 Rectification Phenomena

Critical currents were measured for specimens with surface superconductivity reduced on one surface by evaporation of a 400 Å layer of copper.

Results wereobtained for specimens containing 5.5 at.% bismuth and also for specimens with 2.9 at.% bismuth. From experiments on films with 400 Å layers of copper on both surfaces it was deduced that surface critical currents were reduced by three decades by the presence of copper in fields close to H_{c_2}. Above 1.5 H_{c_2} no superconductivity was detected.

For all specimens with copper on one surface the diamagnetic critical current was larger than the paramagnetic critical current for fields around H_{c_2} and up to H_{c_3}. In the case of the 5.5 at.% Bi alloy the rectification ratio at H_{c_2} (4.2°K) with $\theta = 90°$ and $\varphi = 0°$ was 1.36 ± 0.03 compared with 1.35 ± 0.03 obtained for the 2.9 at.% Bi specimens.

The dependence of the diamagnetic and paramagnetic critical currents on temperature was investigated for a temperature range from 1.83°K to 4.21°K. The rectification ratios for a given reduced field were not altered significantly by variations in temperature. The absolute magnitude of

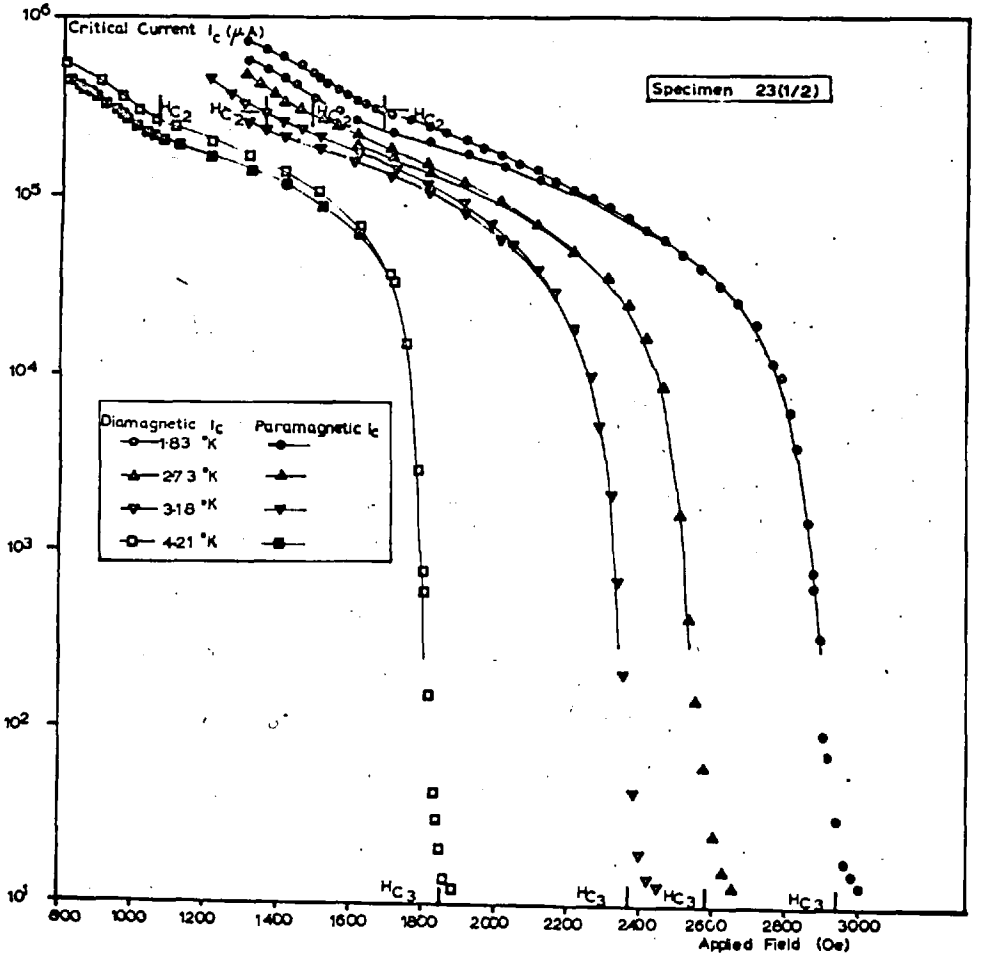

Fig. 41 Variation of Critical Currents with Temperature

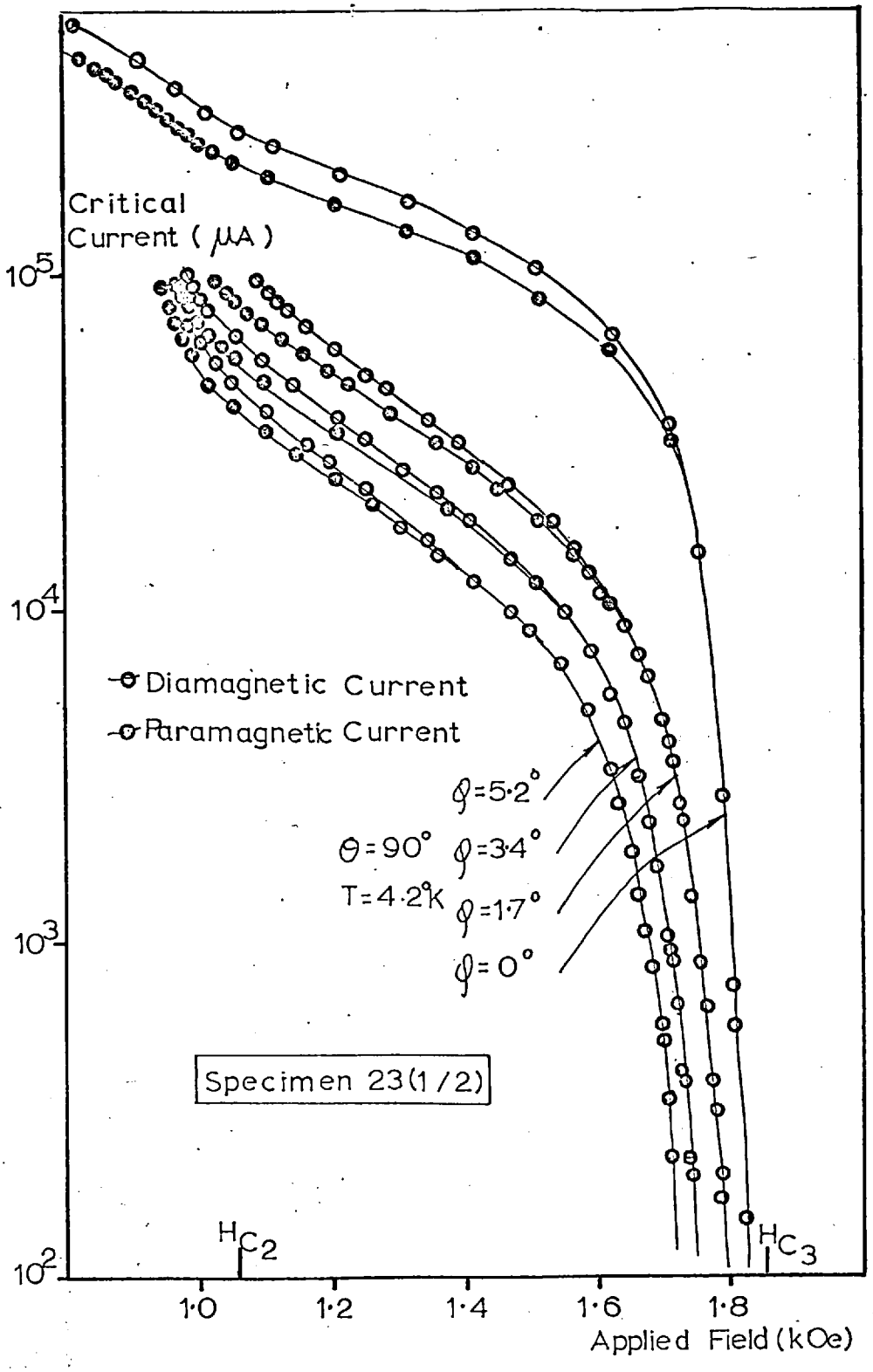

Fig. 42 Variation of Critical Current with Azimuthal Angle φ

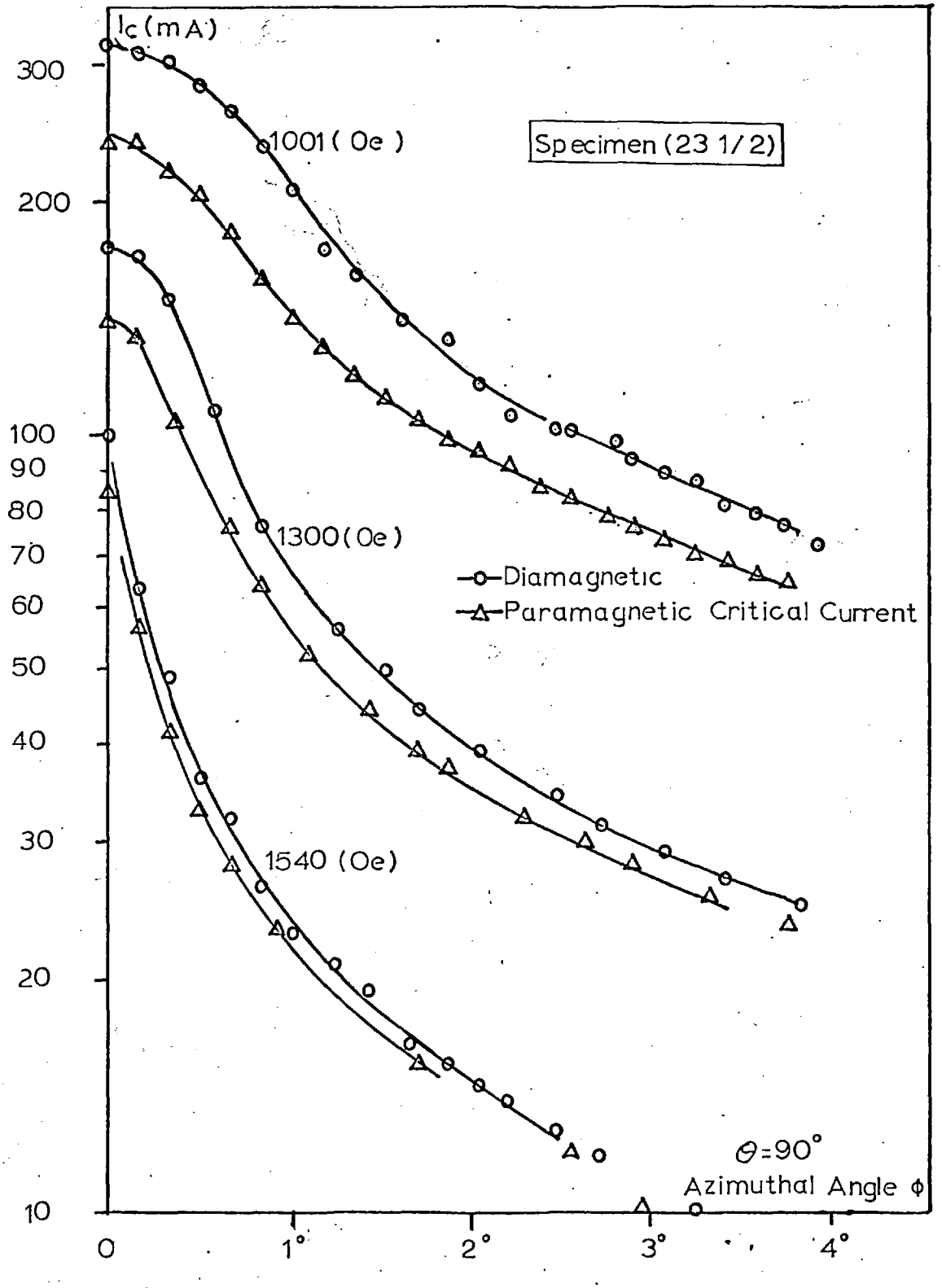

Fig. 43 Diamagnetic and Paramagnetic Critical Currents

the diamagnetic critical current for specimen 23(1/2) at H_{c_2} was reduced by a factor of 0.71 from 410 mA at 1.83°K to 290 mA at 4.21°K. Results for this specimen are illustrated in Fig. 41 on page 105.

The variation of critical current with azimuthal angle φ was measured in constant field with $\theta = 90°$. In the case of specimen 23(1/2) the rectification ratio reached a maximum of 1.42 at $\varphi \approx 0.2°$ for fields close to H_{c_2}. The ratio decreased for further increases in the azimuthal angle. Results are plotted in Figs 42-43 on pages 106-107.

5.9 The Variation of Critical Current with Specimen Width ($\theta = 90°$, $\varphi = 0°$)

The variation of critical current with specimen width was measured for fields between 0.85 H_{c_3} and 0.96 H_{c_3} at 4.2°K. The range of widths covered a decade from 5 mms to about 0.5 mms.

Early attempts at making these measurements were conducted on different specimens of various widths evaporated from the same source. Scatter in the data from these results prevented any strong conclusion to be drawn about the correlation between widths and critical currents. Better reproducibility was achievedby repeatedly trimming

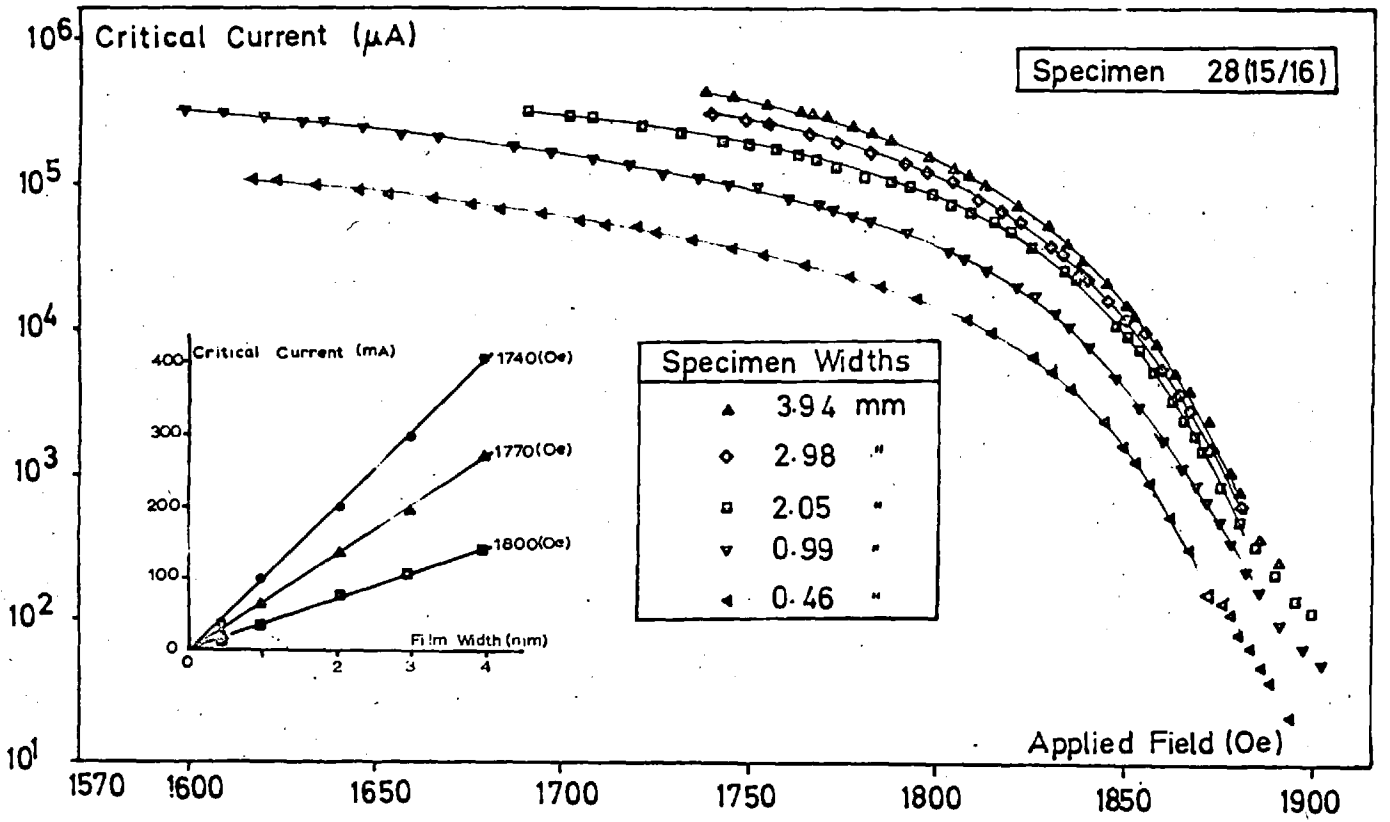

Fig. 44 Variation of Critical Current with Specimen Width

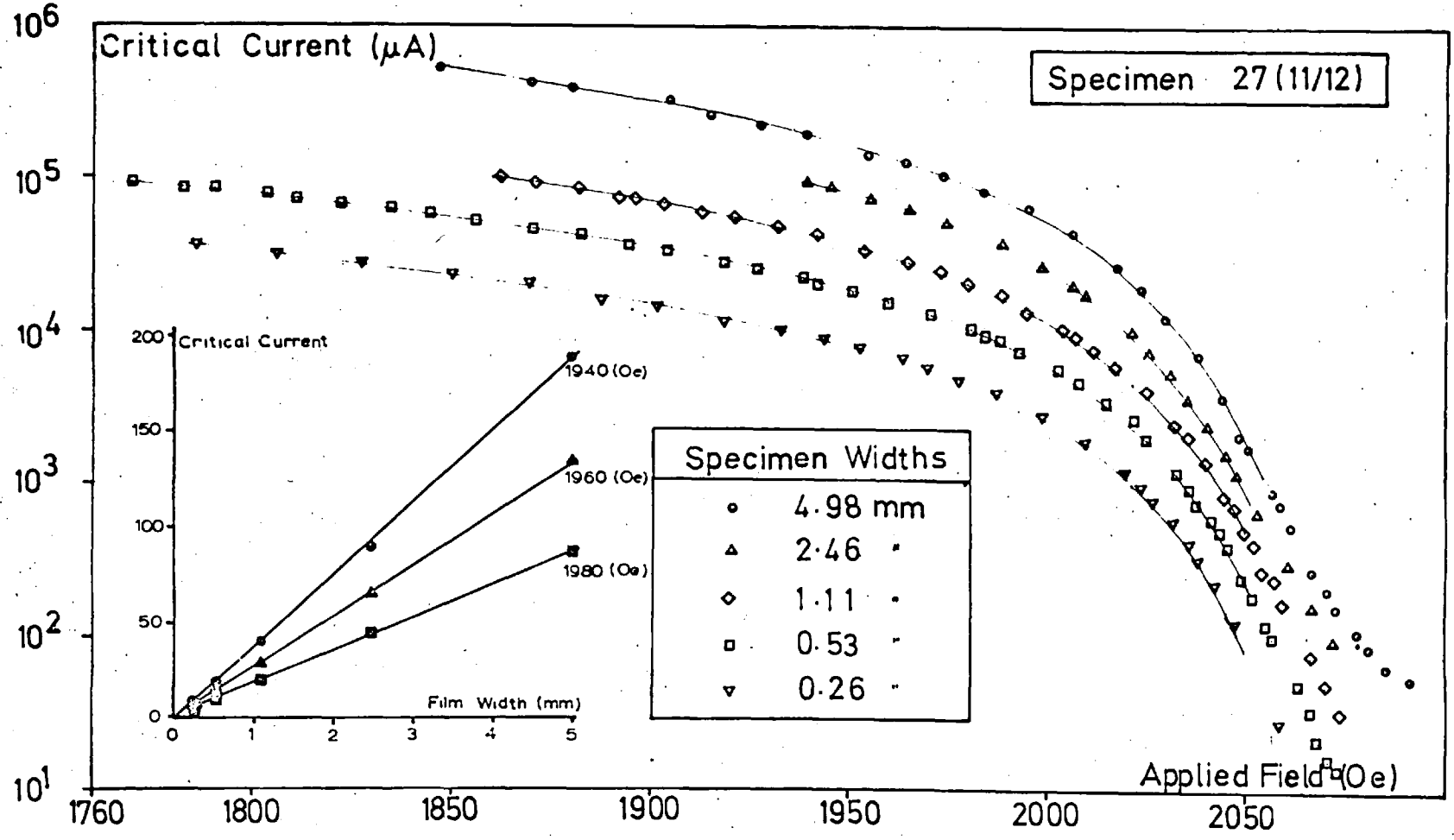

Fig. 45 Variation of Critical Current with Specimen Width

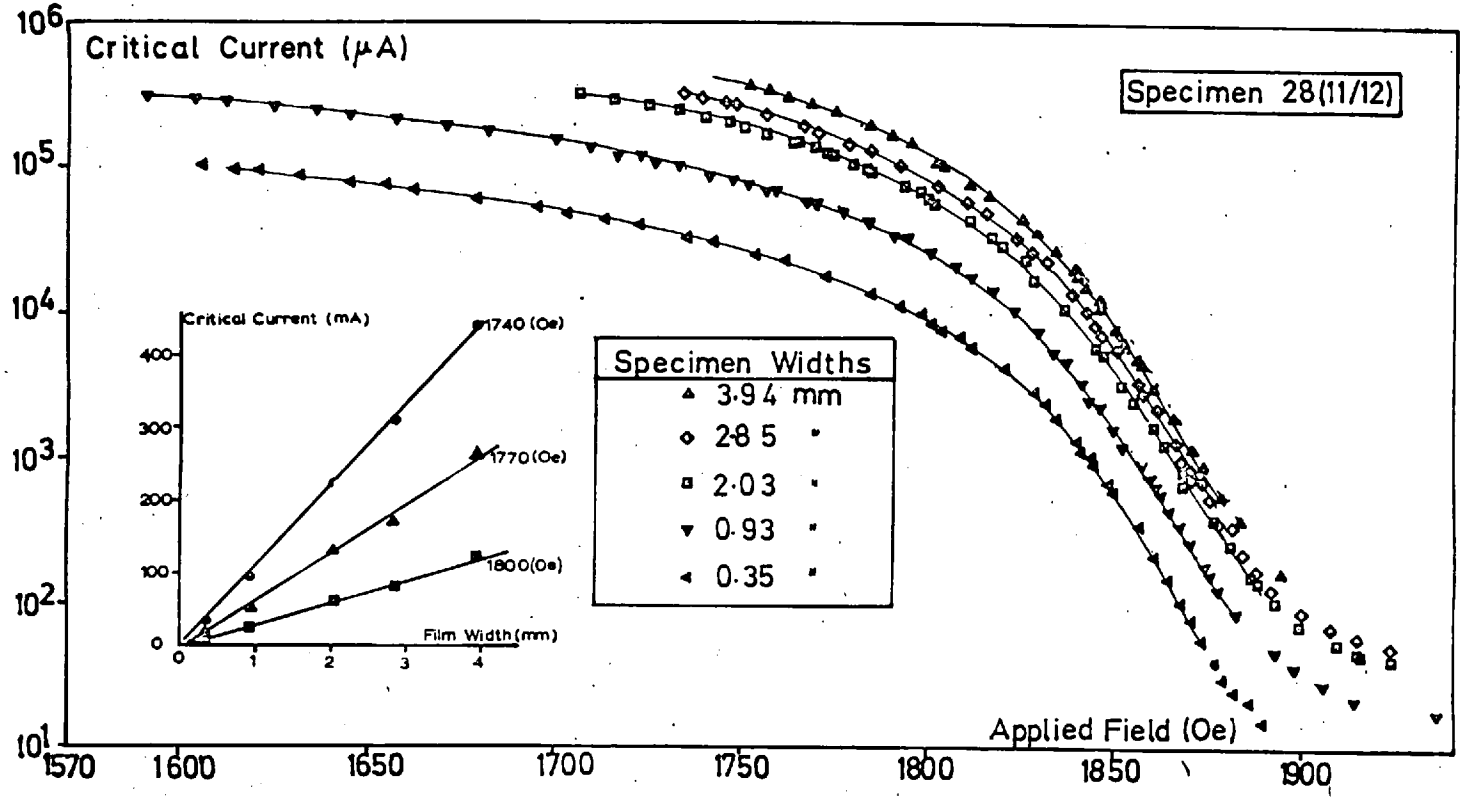

Fig. 46 Variation of Critical Current with Specimen Width

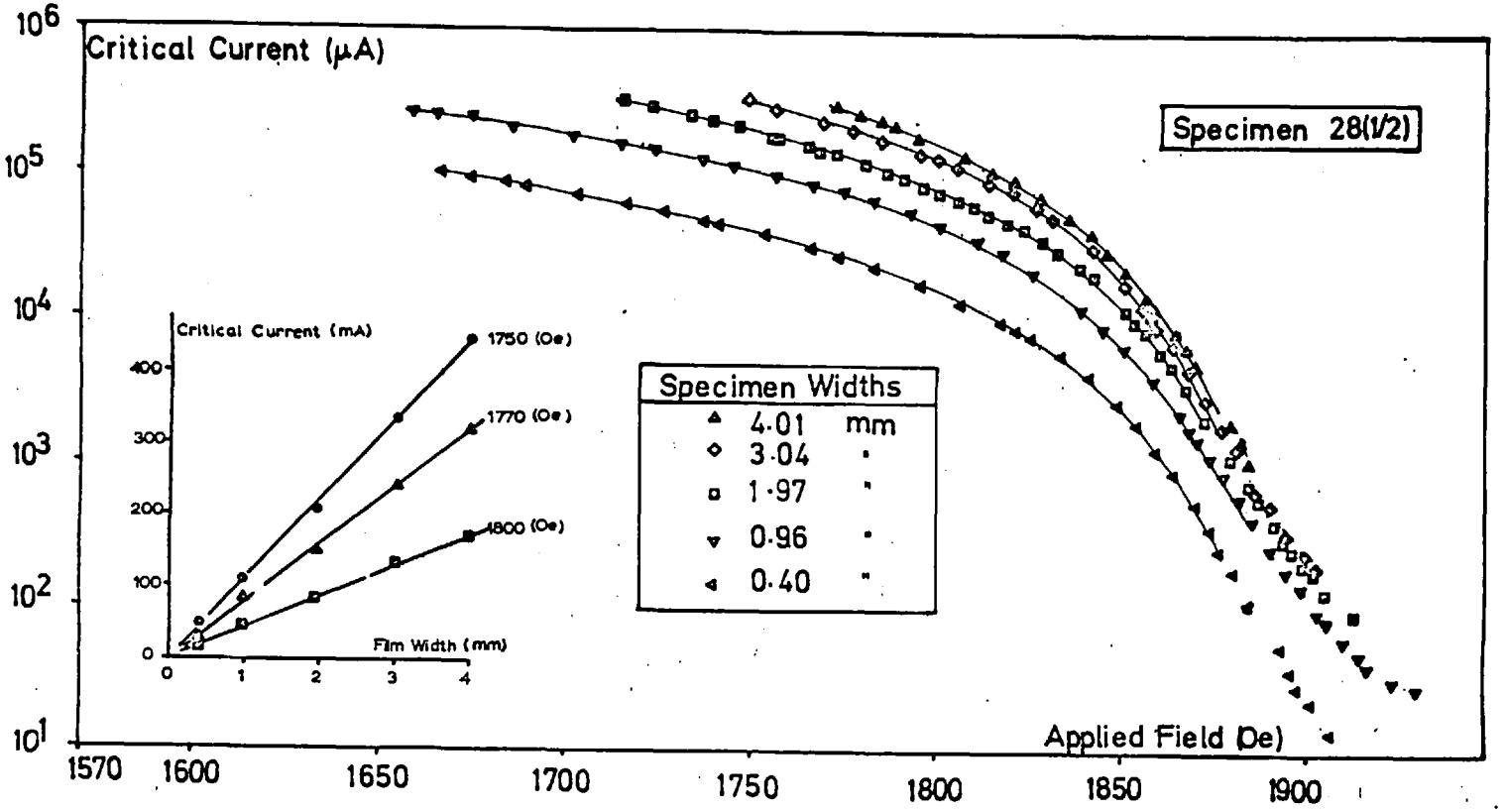

Fig. 47 Variation of Critical current with Specimen Width

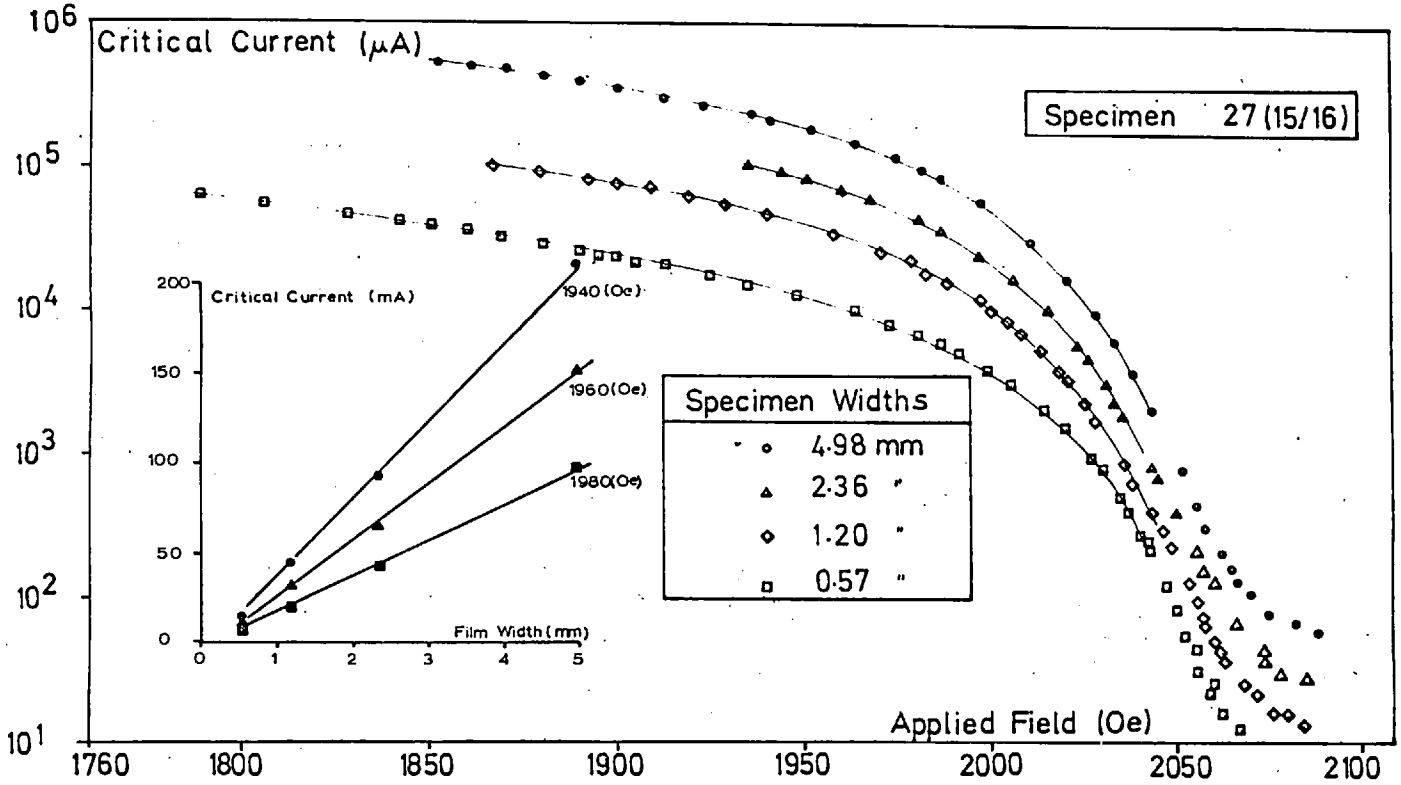

Fig. 48 Variation of Critical Current with Specimen Width

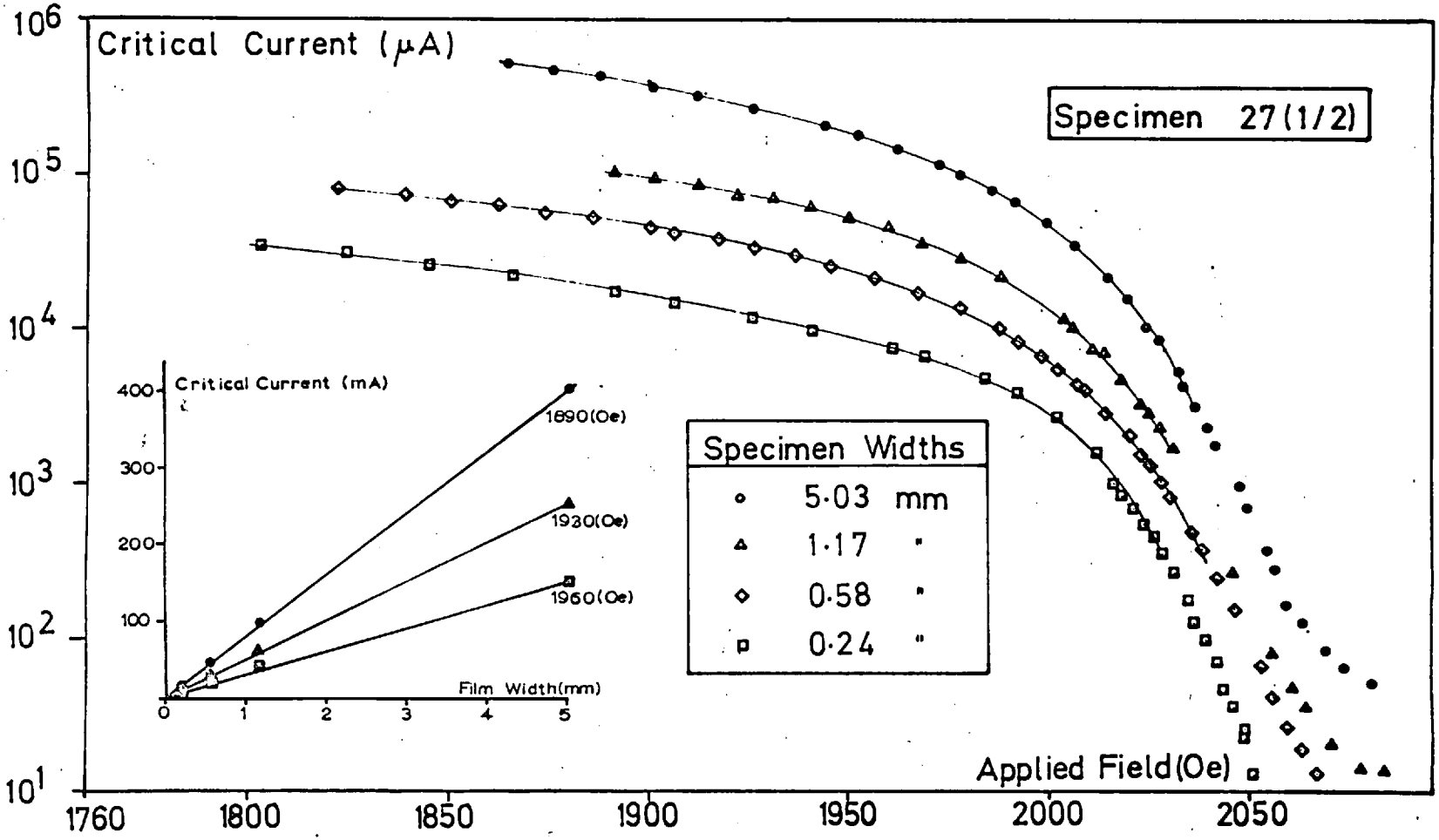

Fig. 49 Variation of Critical Current with Specimen Width

specimens and observing changes in their critical currents. In this way comparisons were made for specimens of almost identical surface structure and composition. This technique entailed making measurements on different days so that specimens could be removed from the cryostat for trimming. In order to correct for the effects due to changes in atmospheric pressure and the hydrostatic head of helium a control film of constant width was inserted into the cryostat. Changes in the observed value of H_{c_3} which were usually around a few Oe. could thus be accounted for and measurements standardized to the same temperature. The shape of the critical current curves for this control film were not significantly affected by small changes in temperature nor by exposure to air for several hours. Results are expressed in Figs 44-49 which demonstrate with good measure of reproducibility that there was a linear relationship between critical current and width.

5.10 Voltage - Current Characteristics

Typical I-V curves are plotted in Figs 50-53 for different fields and ranges of current and voltage. For fields close to H_{c_3} in the orientation $\Theta = 90^\circ$, $\varphi = 0^\circ$,

Fig. 50 Voltage Current Curves

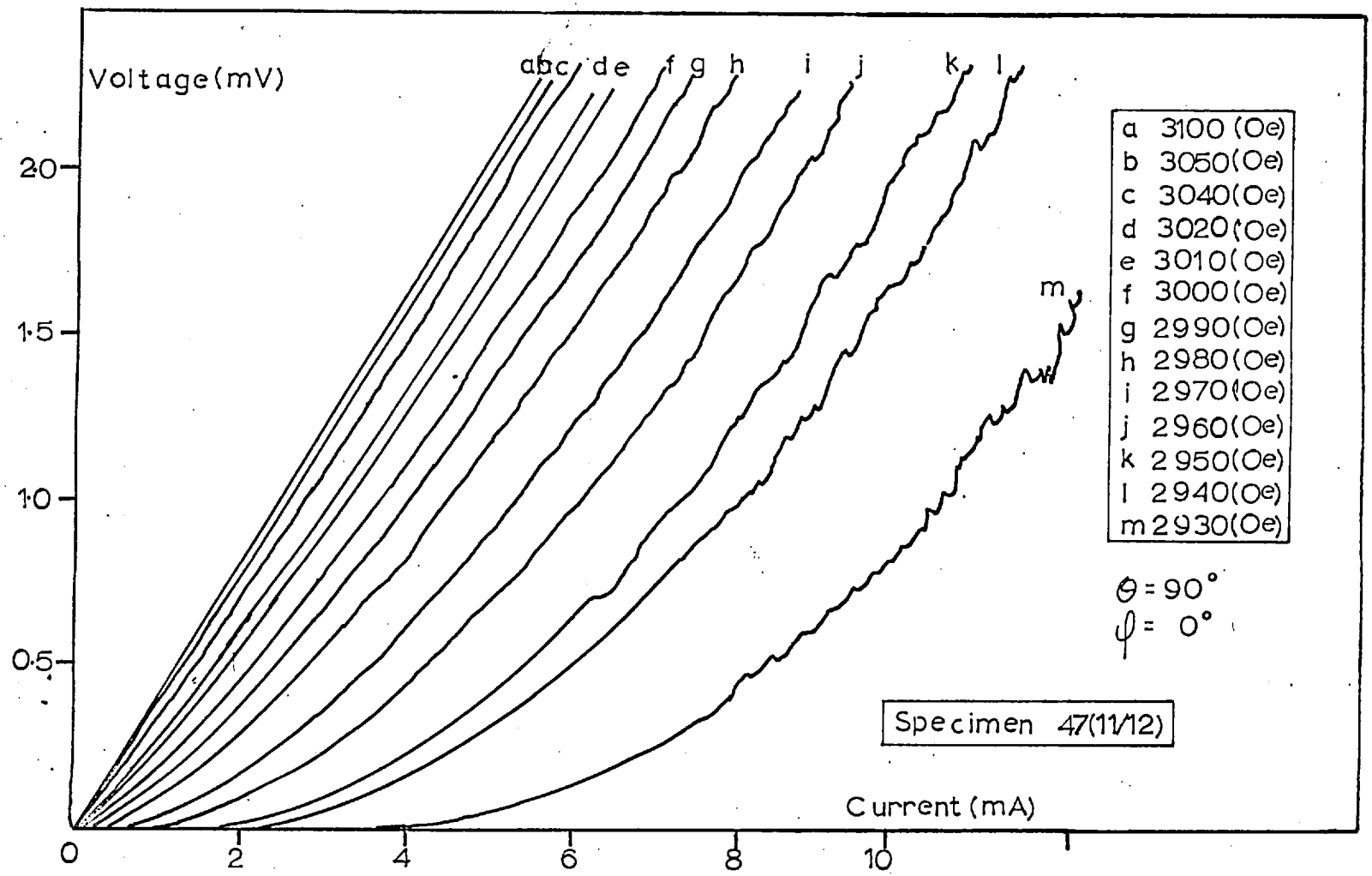

Fig. 51 Voltage Current Curves

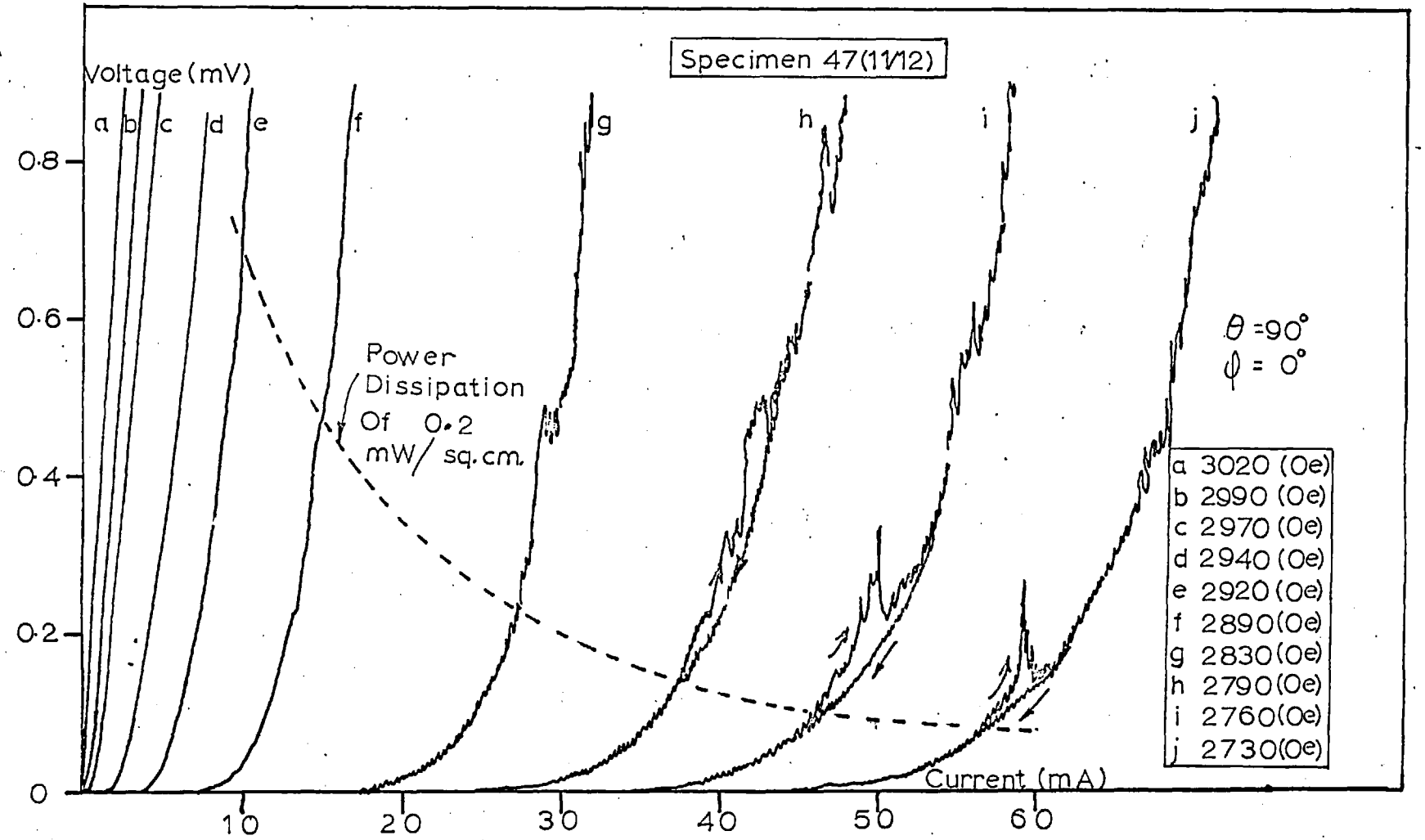

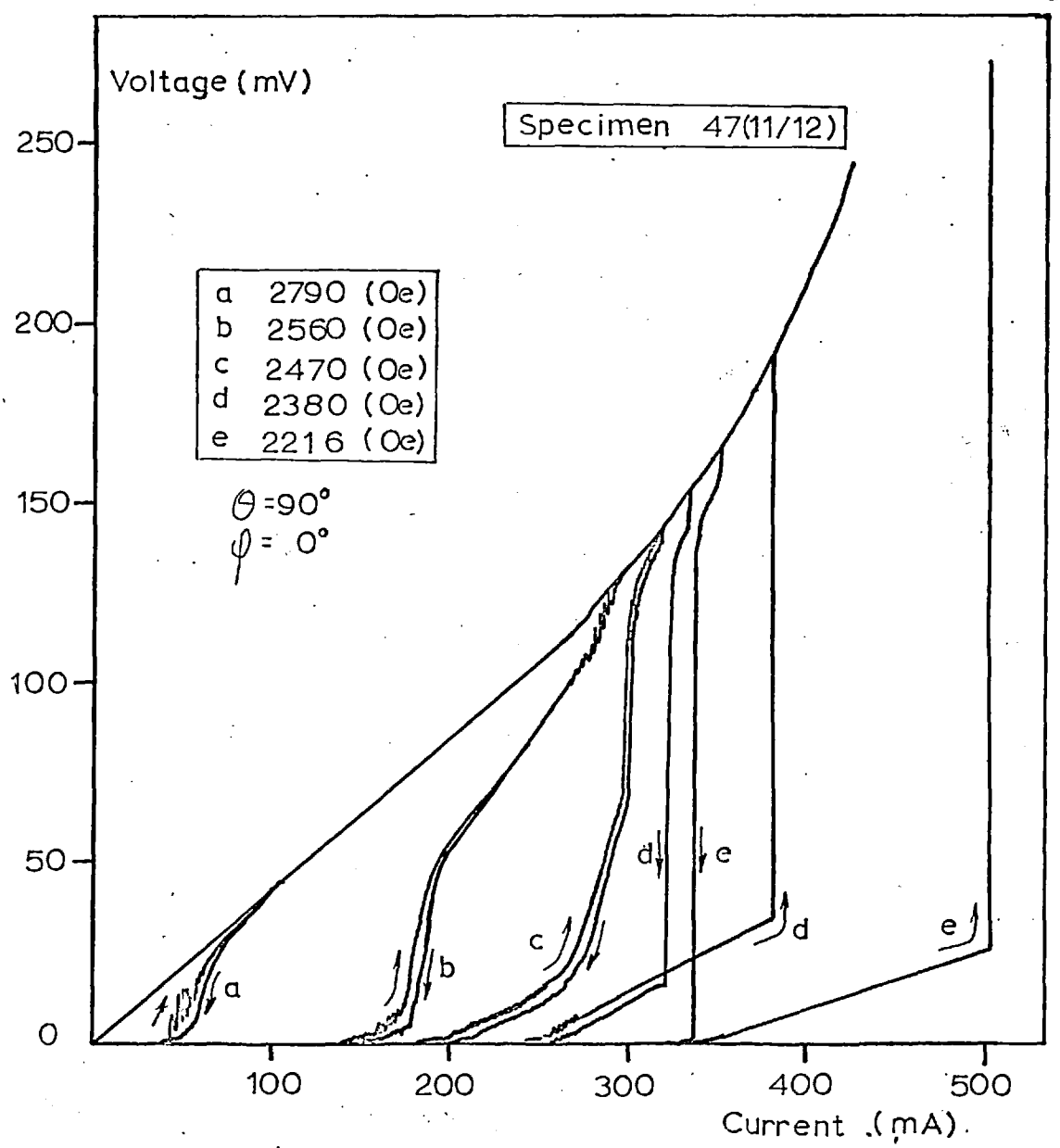

Fig. 52 Voltage Current Curves

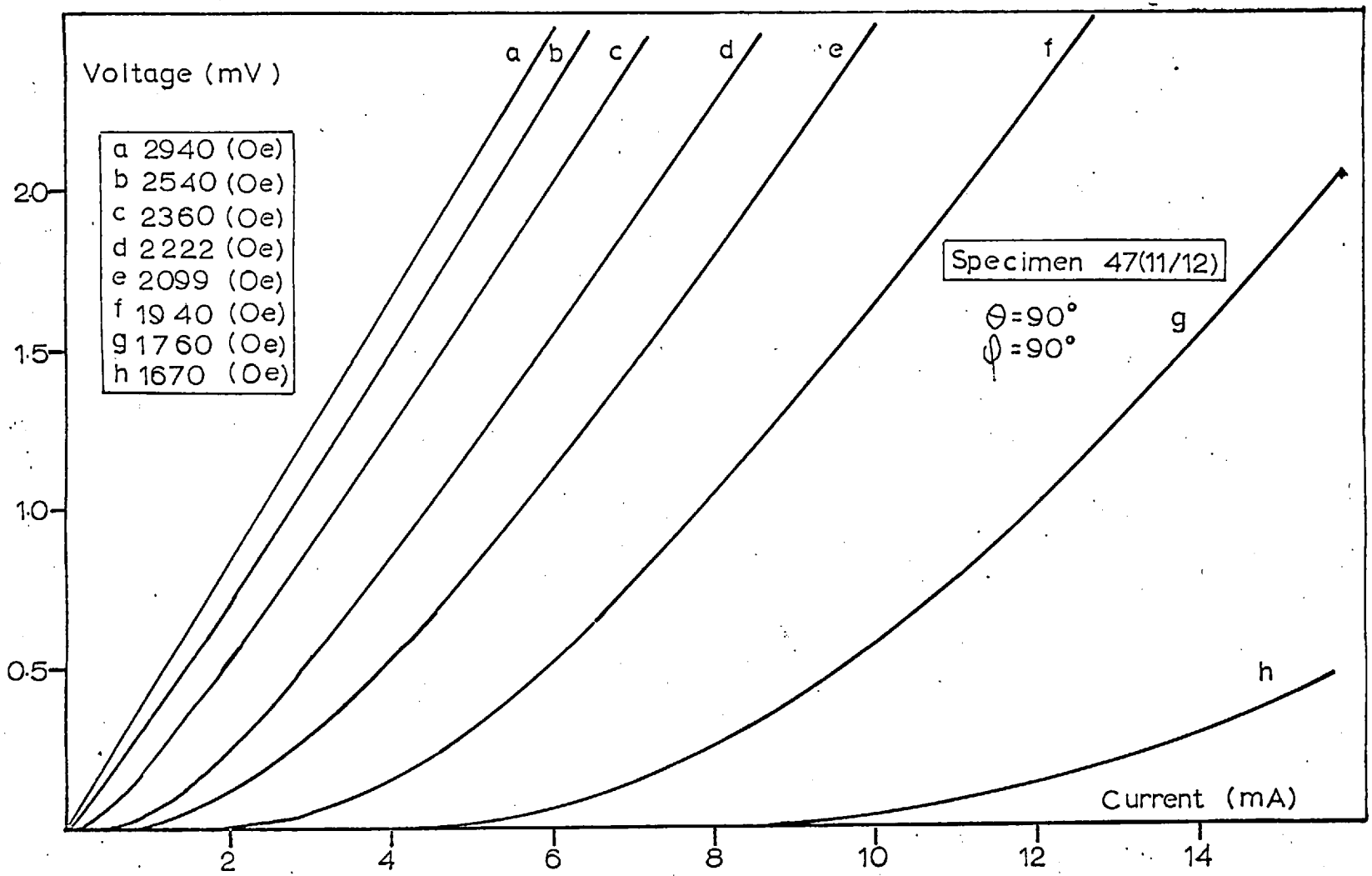

Fig. 53 Voltage Current Curves

I-V curves for power dissipations less than 0.1 mWatts/sq. cm were free of significant fluctuations and the observed voltage equal for increasing and decreasing currents. (Fig. 50). At lower fields, fluctuations in the observed voltage develop for power levels around 0.2 mWatts/sq.cm. (Fig. 51). When the current was increased from zero to a value greater than the current corresponding to the start of these fluctuations the average measured voltage was greater than that recorded as the current was returned to zero. The directions of increasing and decreasing currents are indicated by arrows in the diagrams. I-V curves at still lower fields and for comparatively large power levels of the order of 100 mWatts/sq.cm are illustrated in Fig. 52.

Fig. 53 shows I-V curves for the geometry, $\theta = 90^\circ$, $\varphi = 90^\circ$. Superconductivity persisted for fields greater than Hc_2 probably because of edge effects already discussed in Section 5.2.

CHAPTER VI

DISCUSSION OF RESULTS

6.1 Estimates of the Parameters $\kappa, \lambda, \xi, \xi_o$, and l

Theories concerned with the magnitude of critical surface currents depend on solutions of G-L equations. Most of the experiments described in Chapter V were at a reduced temperature of $T/T_c = 0.56$. Unless the electrodynamics are local, G-L theory is not necessarily valid in this temperature regime. In this section some of the characteristic parameters: κ, λ, ξ, ξ_o and l are calculated from Gorkov-Goodman and G-L theory and compared with experimental data. Consistencies between these comparisons were reasonable and did not invalidate the application of G-L theory on a qualitative basis.

Estimates of the G-L parameter κ were made from the resistivity measurements using the Gorkov-Goodman equation given in section 1.2:

$$\kappa = \kappa_o + 7.5 \times 10^3 \frac{\gamma^{\frac{1}{2}}}{\sigma} \qquad 6.1.1$$

γ for lead was taken as 1713 erg. cm^{-3} $deg.^{-2}$ (64) and assumed to be unchanged by alloying. κ_o was taken as 0.33

from the surface resistance measurements of Fischer (65) on pure lead. The relationship between K_{G-L} calculated from equation 6.1.1 and the composition of the films is shown in Fig. 55. $K_1(4.2^{\circ}K)$ has been measured by Evetts (66) for the Pb-Bi system from magnetization measurements and offers a useful source for comparison. From the calculations of Helfand and Werthamer (20):

$$\frac{K_1(4.2)}{K_{GL}} = 1.1$$

in the dirty limit. For an alloy containing 10 atomic % bismuth , considered to be dirty, this ratio is:

$$1.3 \pm 0.1 = \frac{K_1(4.2^{\circ}K) \text{ (from Evett's results)}}{K_{G-L} \quad \text{(from resistivity measurements)}}$$

It is perhaps of interest to draw attention to the measured residual resistivities of the evaporated films and the resistivities obtained by Livingston (61) for Pb-Bi alloys prepared by melting in an inert atmosphere and casting into moulds. His specimens, which were annealed for about a week within 20°C of their melting point, exhibited residual resistances some 30% higher than those plotted in Fig. 26.. Metallographic studies (66) have shown that in the Pb-Bi system there is a tendency for the cast binary alloy to

solidify with a cellular structure with a high solute concentration in the walls of the cells. Such a structure will lead to high residual resistivities which are only gradually improved by prolonged annealing. It would appear that such structure effects can be obviated by preparing specimens using evaporation techniques.

The coherence length ξ can be obtained from solutions of the linear G-L equations for fields close to $H_{c_2}(T)$:

$$\left[-i\nabla-\left(\frac{2\pi}{\Phi_o}\right)\underline{A}\right]^2\Psi = \left[\frac{1}{\xi^2(T)}\right]\Psi \qquad 6.1.2$$

The lowest eigenvalue of this equation gives:

$$\frac{1}{\xi^2(T)} = \frac{2\pi H_{c_2}(T)}{\Phi_o} \qquad 6.1.3$$

$\lambda(T)$ can be estimated from $\xi(T)$ and $H_c(T)$ (66) through the relationship:

$$H_c(T) = \left[\frac{1}{(8\pi^2)^{\frac{1}{2}}}\right]\left[\frac{\Phi_o}{\lambda(T)\,\xi(T)}\right] \qquad 6.1.4$$

$\lambda(4.2)$ and $\xi(4.2)$ deduced from equations 6.1.3 and 6.1.4 and measurements of H_{c_2} ($4.2^\circ K$) are shown in Fig. 54 as functions of composition. From the two interpolation formulae

obtained by Goodman (equations 1.2.14 and 1.2.15) it is possible to derive the B.C.S. coherence length ξ_o and the normal state electron mean free path, l. The variation of ξ_o and l with composition is illustrated in Fig. 56 where the London penetration depth for pure lead was taken as 390 Å (17).

From the theory of Helfand and Werthamer (20) it is possible to determine the ratio ξ_o/l from the variation of H_{c_2} with temperature near to T_c. This theory was applied to a specimen containing 5.5 atomic % bismuth where H_{c_2} was measured for reduced temperatures between 0.2 and 0.6. The value of $\frac{d}{dt}(H_{c_2})_{t=1}$ was estimated by extrapolating the data using a factor of $(1-t^2)/(1+t^2)$. The value of ξ_o/l so obtained was 6.5 with $H_c(0)$ taken as 900 Oe (18) and $\kappa_o=0.33$. ξ_o/l evaluated for the same specimen from G-L and Gor'kov- Goodman equations was 6·3.

6.2 Comparison of Experimental Critical Currents with Some Calculated Values

In Fig. 57 experimental critical currents for an alloy containing 10.9 at. % bismuth are compared with the parallel field calculations of Park (38) and Fink (41). The ratios of calculated critical currents to experimental values at different reduced fields are compared in Fig. 58.

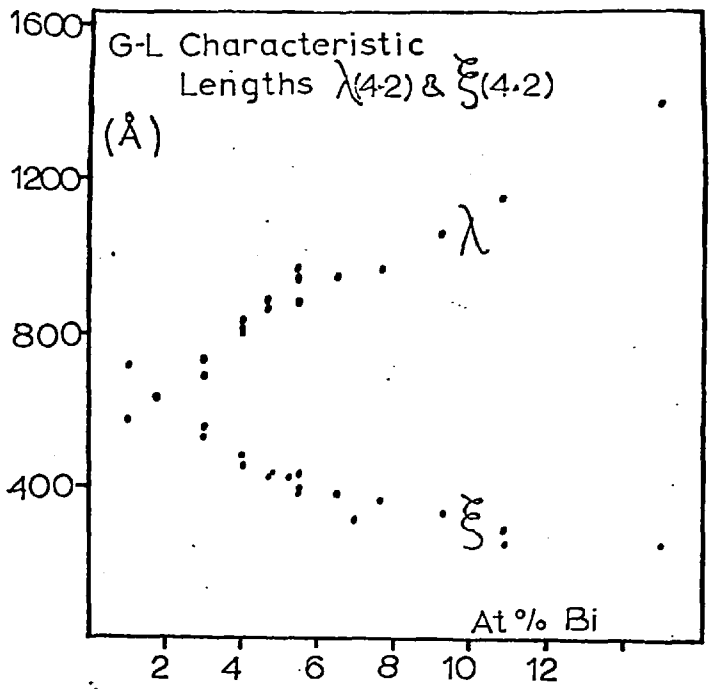

Fig. 54 Characteristic Lengths

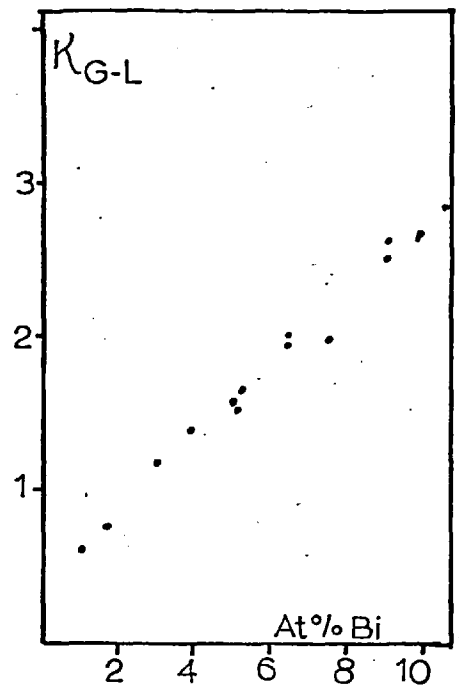

Fig. 55 G-L Parameter

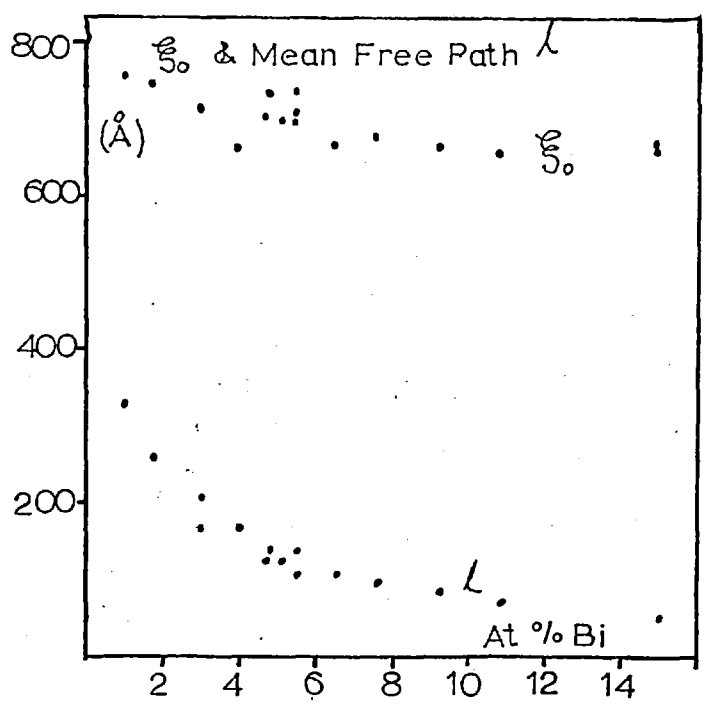

Fig. 56 B.C.S. Coherence Length ξ_0 and Mean Free Path l

If the appearance of a measurable voltage in the surface sheath is associated with the motion of fluxons derived from the transport current, it would be instructive to calculate the current corresponding to the initial penetration of flux at specimen edges. For a surface flux model with no pinning this current would correspond to the critical current. It is possible to make an upper estimate of this current by treating the surface sheath as a thin type-I superconductor (68). Glover and Coffey (45) have shown that for small transport currents the current density at the edge of such a superconductor of thickness t and width w is:

$$je = \frac{2}{\pi} \left(\frac{e}{2b} \frac{wt}{\lambda^2} \right)^{\frac{1}{2}} J \qquad 6.2.1$$

where e is the root of natural logarithms, b is of the order of unity, and J is the average current density. When equation 6.2.1 is applied to the surface sheath, t should be replaced by the sheath thickness Δ(Ho). When the current density at the edges reaches the maximum value which G-L equations allow, fluxons will penetrate the sheath and if there is no pinning mechanism a voltage will be detected. The total current in the specimen corresponding to the penetration of flux is:

$$Ip = \pi j_u K \left(\frac{w}{2e\Delta} \right)^{\frac{1}{2}} \qquad 6.2.2$$

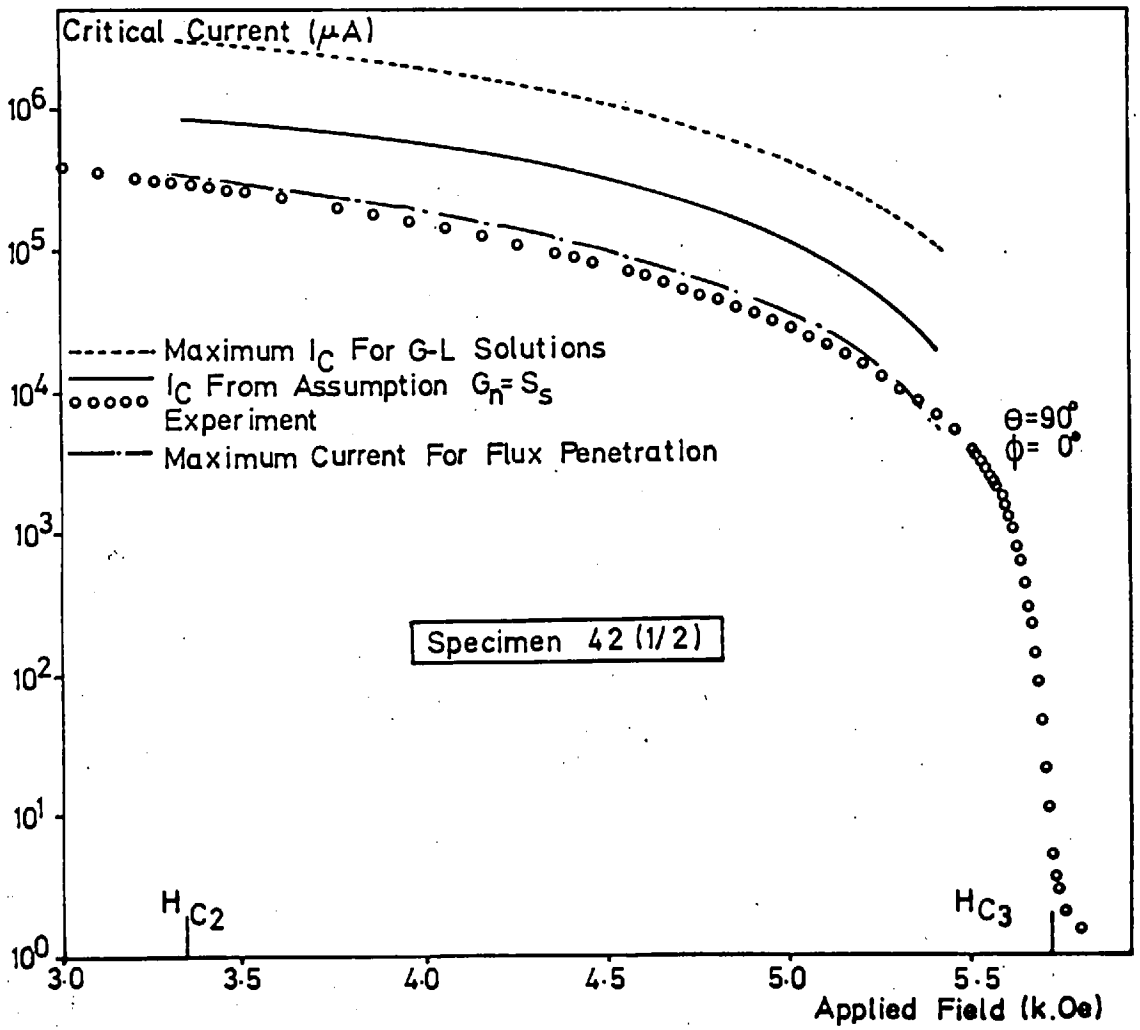

Fig. 57 Comparison of Experiment with Theories

where j_u corresponds to the ultimate critical current density calculated by Park (38). In Figs 57-58 Ip is compared with experimental values. Although the maximum current corresponding to flux penetration shows reasonable agreement with experiment, the dependence of Ip on film width is not in agreement with observations and the closeness of fit might well be fortuitious. For similar reasons the criterion $G_n = G_o$ for the appearance of resistance may be considered doubtful.

Fig. 58 Comparison of Calculated and experimental Critical Currents for Specimen 41(1/2)

Field Ho/H_{c_2}	$\frac{I_c(\text{G-L Theory})}{I_c(\text{Experiment})}$	$\frac{I_c(G_n=G_s)}{I_c}$	$\frac{I_p}{I_c}$
1.00	10.3	2.90	1.17
1.25	12.0	3.54	1.28
1.43	17.1	4.73	1.52
1.54	15.3	3.80	1.34
1.61	14.3	3.14	0.81

$\kappa = 2.9$ and I_c (G-L theory) $= \frac{I_c(\text{dia}) + I_c(\text{para})}{2}$

6.3 Variation of Critical Currents with κ

The ultimate critical surface current densities in type-II superconductors with low κ values have been calculated

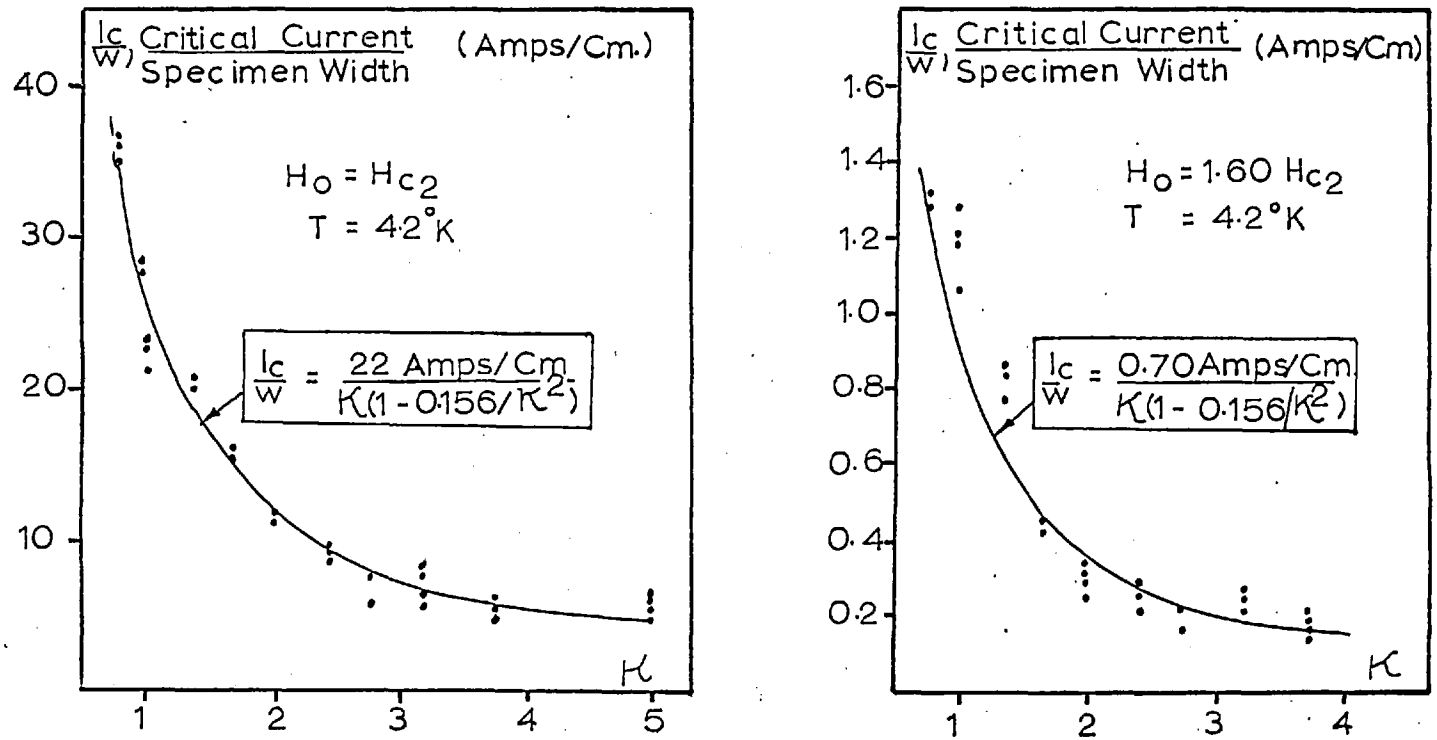

Fig. 59 Variation of Critical Current with K at H_{c_2} and 1.60 H_{c_2}

by Christiansen (69). The average value of the paramagnetic and diamagnetic critical currents for $1 < \kappa < 4$ is approximately proportional to $\frac{I}{\kappa(1 - 0.156/\kappa^2)}$. In order to test the relevance of this proportionality to experiments the critical current data shown in Fig. 40 were replotted with κ as abscissa and fitted to the equation:

$$\text{Ic/unit width} = \frac{A}{\kappa\left(1 - \frac{0.156}{\kappa^2}\right)}, \qquad 6.3.1$$

where κ was taken from the values of λ and ξ shown in Fig. 54. Results of this analysis are shown in Fig. 59 where the solid lines represent equation 6.3.1. Although scatter in the data is considerable there appears to be some justification in applying equation 6.3.1 to determine the κ dependence of surface critical currents.

6.4 Effects of Surface Roughness on Critical Currents

Attempts at expressing roughness on a quantitative basis have been made by Bellau (70) who shows that the sheath critical current can be approximately expressed by the empirical relation:

$$I_c \propto (H_{c_3} - Ho)^n \qquad 6.4.1$$

where n depends on the specimen preparation. Listed below in Fig. 60 are the values of n for evaporated Pb-Bi specimens of different compositions together with Bellau's results for a niobium tantalum alloy.

Fig. 60 Values of n given by Equation 6.4.1

Specimen Preparation		n
4 at.% Bi	evaporated	1.8
5.2 at.% Bi	"	1.9
6.5 at.% Bi	"	1.7
9.3 at.% Bi	"	1.8
10.9 at.% Bi	"	1.8
Bellau:	Electropolished	2
	mechanically polished	3
	Rolled	4.5
	Spark Eroded	6.0

For the Pb-Bi films the critical current could be expressed by equation 6.4.1 for fields from H_{c_2} up to about 1.65 H_{c_2} above which deviations are pronounced and the empirical formula no longer valid.

From studies of platinum-carbon replicas of film surfaces it was possible to produce a rough sketch of the surface of a typical film shown in Fig. 61 together with the relative

magnitudes of λ and ξ.

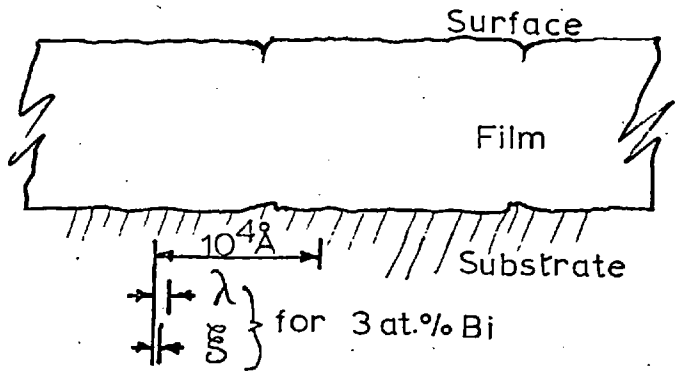

Fig. 61 Rough Sketch of Film Surface

Film surfaces can be treated as essentially flat on a scale greater than ξ and λ except at the location of regions considered to be grain boundaries. In these regions the radii of curvature of the surface is comparable with ξ Niessen et al (71) have found that magnetic flux tends to favour surface furrows and it may be possible that the grain boundaries are a source of pinning.

Several evaporated films were lightly scratched with a squirrel hair brush. After this treatment the critical current was substantially reduced. In these cases the surfaces may have been disturbed in such a manner that

large areas were produced where the applied field is inclined at an angle to the surface contours. In these regions the nucleation field and order parameter would be reduced (72) which would result in a small critical current.

The factors controlling surface flux pinning are not well understood and it would be useful if future studies could be conducted where critical currents are related to electron micrographs of specimen surfaces. The film surface structure might possibly be influenced by some of the following parameters:

(i) Evaporation pressure

(ii) Evaporation rates

(iii) Nature of substrate

(iv) Annealing procedure

6.5 Variation of Critical Current with Azimuthal Angle φ

For an azimuthal angle φ corresponding to a perpendicular component of the applied field greater than about 30 Oe a plot of $1/I_c$ against $\sin\varphi$ for specimen 23(1/2) could be represented by the equation:

$$\frac{1}{I_c} = \frac{1}{I_o} + A \sin\varphi \qquad 6.5.1$$

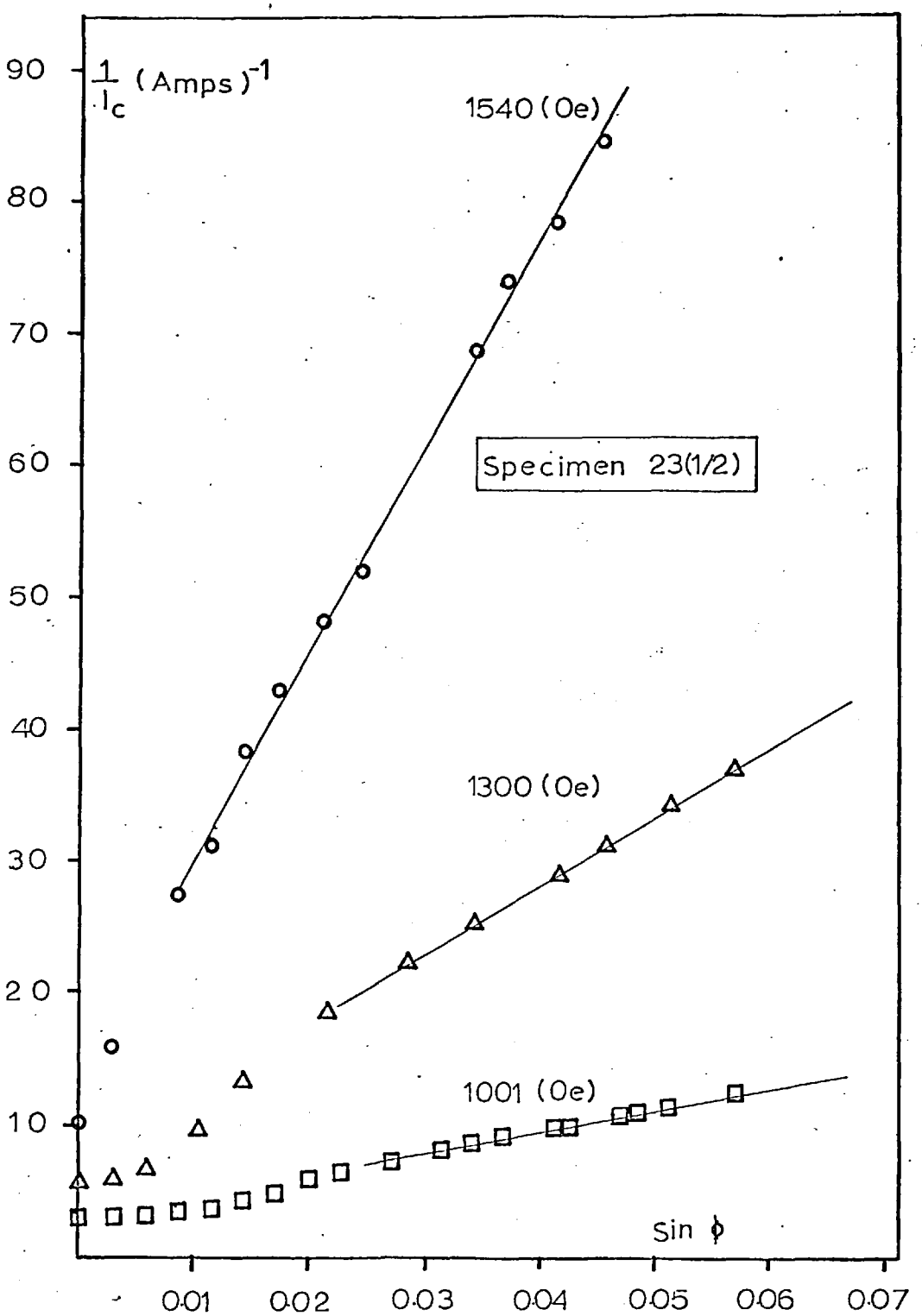

Fig. 62 Variation of Critical Current with ϕ

Results are plotted in Fig. 62. This functional form of the critical current is consistent with the model proposed by Hart and Swartz (44). They consider the number of flux spots per unit area, N, to be equal to $\left(\frac{H_p}{\Phi_o}\right) \sin\theta \sin\varphi$ and if m is the number of pinning centres per unit area, each of strength A, the pinning force per flux spot is:

$$F_p = H_p \frac{mA \Phi_o}{\sin\theta \sin\varphi}$$

provided $N \gg m$. In the critical state F_p can be equated to the Lorentz force, $J\Phi_o$, driving the flux spot across the surface. At very small angles the analysis breaks down since the condition $N \gg m$ may not be satisfied and perpendicular field components arising from the transport current may become comparable to the applied field.

6.6 Rectification Effects

Although the experimentally observed diamagnetic current was greater than the paramagnetic current in contradiction to parallel field calculations based on G-L equations it should be pointed that the theory was worked out only for the case of $\kappa \gg 1$. Rectification experiments on the Pb-Bi films were concerned with κ_{G-L} values of 1.1

and 1.7. The rectification experiment of Hart and Swartz on a $Pb_{0.9}$ $Tl_{0.1}$ evaporated film was also concerned with a low κ_{G-L} value of about 1.8. Christiansen (69) has calculated ultimate critical currents from G-L equations for low κ superconductors and concluded that when κ becomes small the asymmetry between the two currents becomes sensitive to the magnitude of κ. When κ becomes less than about 3 the difference between the two currents should fall to zero and then become larger but of opposite sign. No significant differences in the rectification ratio were detected for experiments on the two Pb-Bi alloys which indicates that rectification effects are insensitive to the asymmetry of the ultimate critical currents. For a surface pinning model the effects most likely to be important in deciding the asymmetry are the thickness of the sheath, already discussed in section 2.6, and the magnitude of the average value of the order parameter in the surface sheath which will depend on the local magnetic field. The magnetic field in the region of the sheath is enhanced by the presence of a paramagnetic current which would decrease the order parameter and the pinning strength. The applied field is reduced by a diamagnetic current which

would result in an increased pinning strength.

6.7 Voltage - Current Characteristics for $\varphi = 0$, $\Theta = 90^\circ$

In order to relate voltage-current characteristics to the surface sheath it was necessary to treat the measured current as the sum: $I = I_n + I_s$ where I_n is the current flowing in the normal bulk estimated by measuring the current in an applied field greater than H_{c_3}. I_s is the current through the surface sheath which was again treated as the sum of two components:

$$I_s = I_o + I_F$$

I_o is the current corresponding to the appearance of a voltage and I_F is the current which, for simple flux flow, should be related to the measured voltage through a viscosity coefficient. This analysis was executed on specimen 47 (15/16) for different applied fields between H_{c_2} and H_{c_3}. Results are expressed in the form of log V plotted against log I_F with I_o estimated from critical current measurements on the same specimen. From the graph plotted in Fig. 63 it can be shown that for power dissipations less than about 0.1 milliwatts/sq.cm, voltages and currents could be related by a power law:

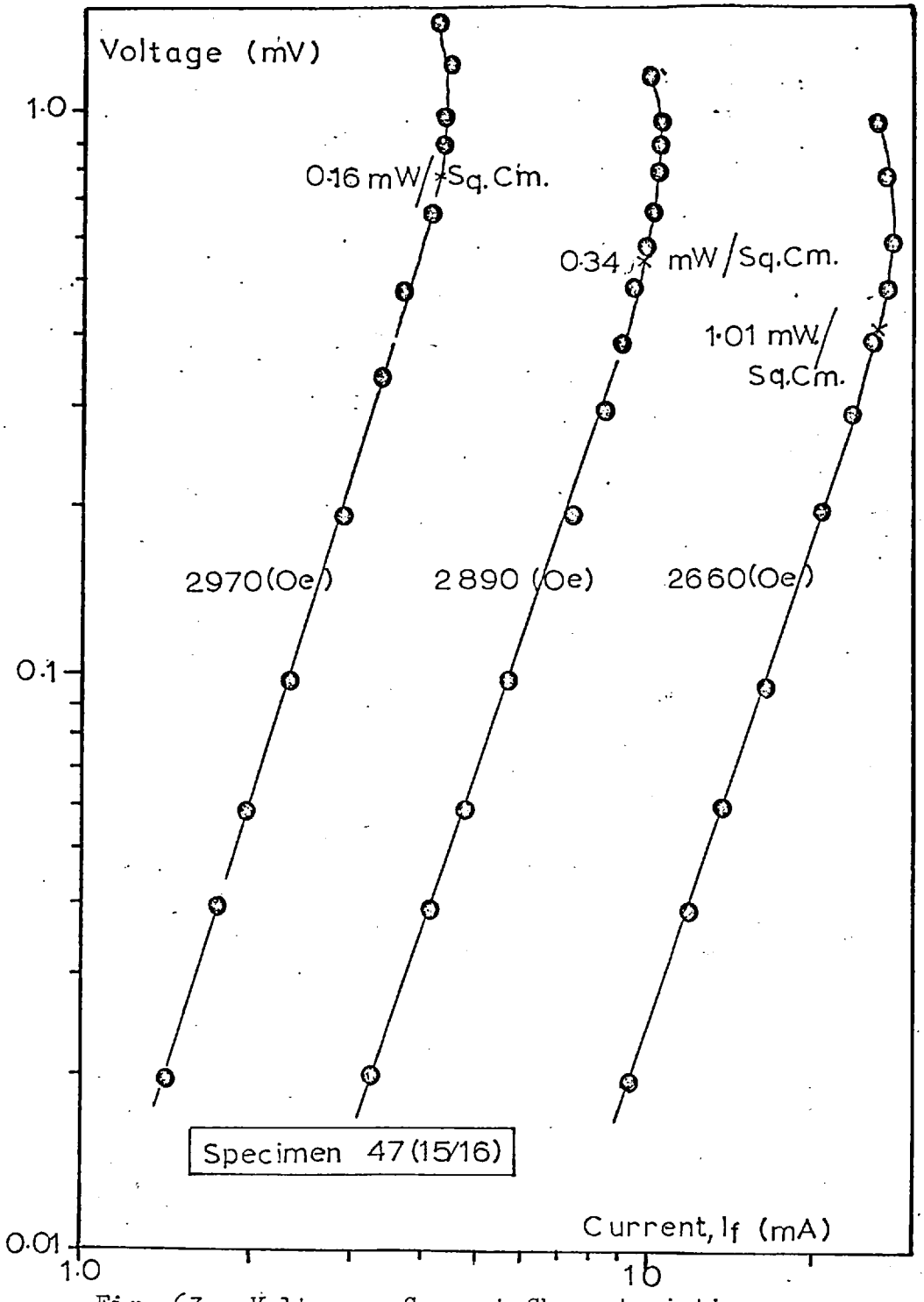

Fig. 63 Voltage - Current Characteristics

$$V \propto (I_F)^n \qquad 6.7.1$$

where n was 3.1 $\pm$ 0.1 and independent of the applied field. The power dissipation level corresponding to the initiation of voltage fluctuations depended on field strength - the lower the field the greater the power necessary to start instabilities. Power dissipations are indicated in Fig. 63. Flux flow experiments on the mixed state in perpendicular fields with surface currents reduced by proximity effects yield linear voltage current relationships (73). However, the results obtained for the surface sheath are not inconsistent with a flux flow model if vortices are derived from the transport current rather than the applied field, i.e. if the perpendicular field H_p is a function of the transport current density j .. From simple flux flow ideas outlined in section 2.2:

$$j\left[H_p(j)\right] \propto \eta v \qquad 6.7.2$$

and the observed voltage is::

$$V \propto H_p(j) \qquad 6.7.3$$

From equations 6.7.2 and 6.7.3 it follows::

$$V \propto j \left[H_p(j)\right]^2 \qquad 6.7.4$$

fluctuations for power
The voltage/dissipations above 0.1 milliwatts/sq.cm can hardly be created by overall changes in temperature since such dissipations, averaged over the film, can produce only a few millidegrees rise in temperature. Available published data on the relation between power dissipation in liquid helium I and temperature changes is somewhat variable and the formula quoted from reference 58 in section 4.3 is probably not appropriate over a large range of temperatures. More recent data is expressed in Fig. 64 taken from experiments by Karagouris (74) and Klipping and Kutzener (75)

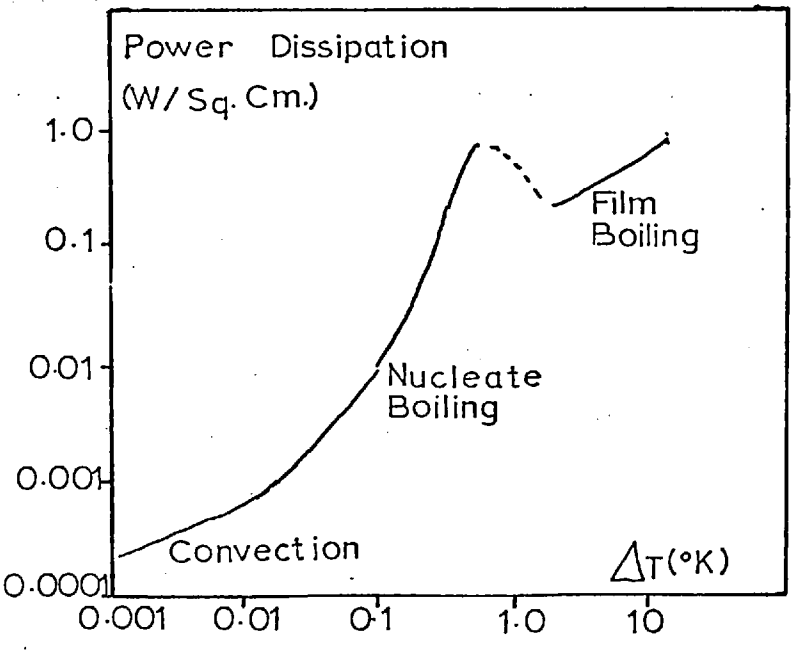

Fig. 64 Relation between Power Dissipation and Changes in Temperature for Liquid Helium

It may be possible that even though the average power dissipation in the Pb-Bi films was small, there were local regions in the film where this dissipation was high enough to initiate instabilities. In future investigations it might prove interesting if I-V characteristics were determined at reduced temperatures just above and below the λ point where the heat loss characteristics undergo abrupt changes. At high power dissipations above 100 mW /sq. cm in liquid helium I matters are further complicated by the effects of nucleate and film boiling of liquid helium.

APPENDIX 1

Dimensions of Specimens Named in Chapters V-VI

Specimen No.	At.%Bi	Width (mm)	Distance between Potential Leads (cm)
18(11/12)	5.5	1.4	0.83
18(15/16)	5.5	1.4	0.83
23(1/2)	2.9	0.7	0.68
23(11/12)	2.9	0.7	0.68
27(1/2)	3.0		0.66
27(11/12)	3.0	Dimensions	0.66
27(15/16)	3.0	given in	0.66
28(1/2)	3.0	text	0.66
28(11/12)	3.0		0.66
28(15/16)	3.0		0.66
33(11/12)	1.0	0.460	0.67
34(13/14	5.2	0.472	0.68
38(11/12)	9.3	0.561	0.680
38(15/16)	9.3	0.547	0.671
41(1/2)	6.5	0.440	0.660
41(13/14)	6.5	0.527	0.672
46(1/2)	4.0	0.419	0.690
47(11/12)	5.1	0.479	0.689
47(15/16)	5.1	0.470	0.670

APPENDIX 2

Analysis of Specimen Compositions

Electron probe analysis was executed on a specimen with a nominal average composition of 5.0 at.% Bi. Unfortunately this method was only sensitive enough to just resolve the presence of bismuth in lead; thus a quantitative determination of spatial variations in composition could not be made. The estimated lower and upper limits of the average film composition were 0.5 at.% Bi and 10 at.% Bi. Qualitatively this technique indicated that areas scanned by the electron probe contained no agglomerated regions of pure lead or pure bismuth. From the electron probe trace and from images produced by back-scattered and absorbed electrons it was possible to deduce the topography of the surface. "Circular" spots of about 5μm in diameter were observed scattered over the film surface. These spots, separated by distances of a few hundredμm, were attributed to either specks of dust or small holes in the film. In addition to the spots there was some indication of a pattern which could have been a crystal structure with a grain size of about 4μm.

A better estimate of the average composition was achieved by the chemical method of polarography. The specimen on which analysis was conducted was made from a mixture containing 5.0 at.% Bi prior to evaporation. The average composition of the film produced from the source was (4.8 0 $\pm$ 0.14) at.% Bi.

REFERENCES

(1) L. D. LANDAU and E. M. LIFSHITZ, Statistical Physics, Pergamon, London (1958)

(2) V. L. GINZBURG and L. D. LANDAU, Soviet Phys. J.E.T.P. 20, 1064 (1950)

(3) G. STEPHENSON, Mathematical Methods for Science Students, Longmans, London (1962)

(4) H. A. KRAMERS, Quantum Mechanics, North-Holland Publishing Co., Amsterdam (1957)

(5) J. BARDEEN, L. N. COOPER and J. R. SCHRIEFFER, Phys. Rev. 108, 1175 (1957)

(6) L. P. GORKOV, Soviet Phys. J.E.T.P. 9, 1364 (1959)

(7) L. P. GORKOV, Soviet Phys. J.E.T.P. 10, 998 (1960)

(8) E. A. LYNTON, Superconductivity, Methuen, London (1962)

(9) B. B. GOODMAN, Rep. Prog. Phys., 29, 445 (1966)

(10) A. A. ABRIKOSOV Soviet Phys., J.E.T.P. 5, 1174 (1957)

(11) W. H. KLEINER, L. M. ROTH and S. H. AUTLER, Phys. Rev., 133, A1226 (1964)

(12) J. MATRICON, Physics Lett., 9, 289 (1964)

(13) V. ESSMANN and H. TRAUBLE, Physics Lett., 24A, 526 (1967)

(14) D. St. JAMES and P. G. de GENNES, Physics Lett., 7, 306 (1963)

(15) D. P. JONES, Ph.D. Thesis, University of London (1969)

(16) J. McEVOY, Ph.D. Thesis, University of London (1968)

(17) H. J. FINK and R. D. KESSINGER, Phys. Rev., 140, A1937 (1965)

(18) G. FISCHER and K. MAKI, Phys. Rev., 176, 581 (1968)

(19) K. MAKI, Phys. Rev., 148, 362 (1966)

(20) E. HELFAND and N. R. WERTHAMER, Phys. Rev., 147, 228 (1966)

(21) L. TEWORDT, Zeit Physik, 184, 319 (1965)

(22) G. EBNETH and L. TEWORDT, Zeit Physik, 185, 421, (1965)

(23) K. D. USADEL and SCHMIDT, Zeit Physik, 221, 35, (1969)

(24) P. W. ANDERSON, Phys. Rev. Lett., 9, 309 (1962)

(25) R. DELTOUR and M. TINKHAM, Phys. Rev. Lett., 19, 125 (1967)

(26) J. FRIEDEL, P. G. de GENNES and J. MATRICON, Appl. Phys. Lett., 2, 119 (1963)

(27) C. CAROLI and K. MAKI, Phys. Rev., 164, 591 (1967)

(28) A. C. ROSE-INNES and E. H. RHODERICK, Introduction to Superconductivity, Pergamon Press, London (1969)

(29) J. VOLGER, F. A. STAAS and A. G. van VIJFEIJKEN, Physics Lett., 9, 303 (1964)

(30) M. TINKHAM, Phys. Rev. Lett., 13, 804 (1964)

(31) A. K. NIESSEN and F. A. STAAS, Phys. Lett., 15, 26 (1965)

(32) J. G. PARK, Phys. Lett., 20, 346 (1966)

(33) B. D. JOSEPHSON, Phys. Lett., 16, 242 (1965)

(34) Y. B. KIM, C. F. HEMPSTEAD and A. R. STRNAD, Phys. Rev., 139, A1163 (1965)

(35) P. G. de GENNES and J. MATRICON, Rev. Mod. Phys., 36, 45 (1964)

(36) P. W. ANDERSON and Y. B. KIM, Rev. Mod. Phys., 36, 39 (1964)

(37) A. A. ABRIKOSOV, Soviet Phys., J.E.T.P. 20, 480 (1965)

(38) J. G. PARK, Phys. Rev. Lett., 15, 352 (1965)

(39) H. J. FINK, Phys. Rev. Lett., 14, 309 (1965)

(40) L. J. BARNES and H. J. FINK, Phys. Rev., 149, 186 (1966)

(41) H. J. FINK and L. J. BARNES, Phys. Rev. Lett., 15, 792 (1965)

(42) J. G. PARK, Phys. Rev. Lett., 16, 1196 (1966)

(43) P. S. SWARTZ and H. R. HART Jnr., Phys. Rev., 137, A818 (1965)

(44) H. R. HART and P. S. SWARTZ, Phys. Rev., 156, 403 (1967)

(45) R. E. GLOVER and H. T. COFFEY, Rev. Mod. Phys., 36, 299 (1964)

(46) G. FISCHER and R. KLEIN, Phys. Lett., 23, 311 (1966)

(47) B. D. CULLITY, Elements of X-Ray Diffraction, Addison-Wesley, London (1959)

(48) C. MALSEED and W. A. RACHINGER, Scripta Metallurgica, 3, 139 (1969)

(49) L. HOLLAND, Vacuum Deposition of Thin Films, Chapman and Hall, London (1966)

(50) L. KOPF, The Review of Scientific Instruments, 38, 734 (1967)

(51) H. L. CASWELL, Physics of Thin Films, 1, 1 (1963), Academic Press, London

(52) W. SEITH and J. G. LAIRD, Smithells Metals Reference Book, 2, 597, Butterworths, London (1962).

(53) S. TOLANSKY, An Introduction to Interferometry, Longmans, (1955)

(54) J. H. FISHER and J. C. ANDERSON, Thin Solid Films, 2, 119 (1968)

(55) G. K. WHITE, Experimental Techniques in Low Temperature Physics, Clarendon Press, Oxford (1968)

(56) F. G. BRICKWEDDE, H. van DIJK, M. DURIEUX, J. R. CLEMENT and J. K. LOGAN, J. Research N.B.S. 64A, 1 (1960)

(57) S. WIPF, Ph.D. Thesis, University of London (1961)

(58) V. L. NEWHOUSE, Applied Superconductivity, John Wiley & Sons Inc., New York (1964)

(59) E. A. FAULKNER and A. HOLMAN, J. Sci. Instrum., 44, 391 (1962)

(60) W. H. J. CHILDS, Physical Constants, Methuen & Co. Ltd, London (1960)

(61) J. D. LIVINGSTON, Phys. Rev., 129, 1943 (1965)

(62) H. GAMARI, Ph.D. Thesis, University of London (1964)

(63) J. P. BURGER and D. St. JAMES, Superconductivity, edited by R. D. Parks, 2, 977 (Marcel Decker) New York (1969)

(64) D. L. DECKER, D. E. MAPOTHER and R. W. SHAW, Phys. Rev., 112, 1888 (1958)

(65) G. FISCHER, Phys. Rev. Lett., 20, 268 (1968)

(66) J. E. EVETTS, Ph.D. Thesis, University of Cambridge (1968)

(67) J. M. LOCK, Proc. Roy. Soc., A208, 391 (1951)

(68) J. G. PARK, Advances in Phys., 18, 103 (1969)

(69) P. V. CHRISTIANSEN, Solid State Comm., 4, 607 (1966)

(70) R. V. BELLAU, Phys. Lett., 21, 13 (1966)

(71) A. K. NIESSEN, J. van SUCHTELEN, F. A. STAAS and W. F. DRUYVESTEYN, Phillips Res. Rept., 20, 226 (1965)

(72) K. YAMAFUJI, E. KUSAYANAGI and F. IRIE, Phys. Lett. 21, 11 (1966)

(73) J. A. CAPE and I. F. SILVERA, Phys. Rev. Lett, 20, 326 (1968)

(74) A. KARAGOUNIS, Bull. Int. Inst. Refrig. Annex 2, 195 (1956)

(75) G. KLIPPING and K. KUTZNER, Cryogenics, 9, 11 (1969)